Studies of crystalline organic molecular materials under extreme conditions

Timothy James Biggs
St. Cross College, Oxford

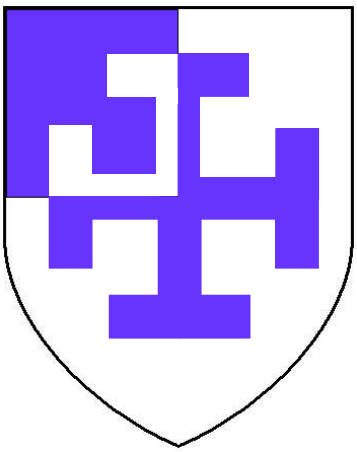

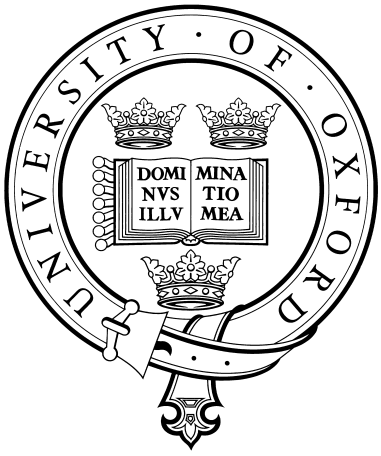

A thesis submitted for the degree of
Doctor of Philosophy
at the
University of Oxford
Hilary term 2006

Studies of crystalline organic molecular materials under extreme conditions

Timothy James Biggs,
St. Cross College,
Oxford University
Hilary Term 2006

Abstract of Thesis Submitted for the Degree of Doctor of Philosophy

This thesis describes investigations into the properties of κ-phase BEDT-TTF charge transfer salts. Charge transfer salts are mainly studied as they are very useful test beds for fundamental physics due to the tuneability of their properties and ground states. The effects of temperature and pressure on such systems have been studied, as these allow access to a wide range of different states and properties. Transport properties of these systems have been studied to obtain information about the Fermi surface and effective mass, and the effect of deuteration and also change of pressure media will be discussed. The interaction of infrared radiation with these systems has also been investigated and simultaneous pressure and temperature measurements will be presented, something not greatly studied due to the large technical challenges. The techniques and approaches for overcoming these are also discussed.

Chapter 1 provides an introduction to the organic materials themselves with particular emphasis on the actual compounds studied.

Chapter 2 provides the necessary theoretical background for studying organic charge transfer salts using magnetic quantum oscillations and their infrared reflectivity.

Chapter 3 covers the experimental techniques and also discusses some of the challenges encountered and their solutions to aid others working in this area.

Chapter 4 describes an investigation into the transport properties of κ-$(ET)_2Cu(SCN)_2$ by studying Shubnikov-de Haas oscillations using both deuterated and normal samples and using two different pressure media, and comparing it to work done using a third.

Chapter 5 presents an investigation into the pressure dependence of selected phonon modes in κ-$(ET)_2Cu(SCN)_2$ using infrared radiation on a deuterated sample.

Chapter 6 presents what is believed to be the first pressure and temperature dependent infrared study of an organic molecular material. In this case the organic molecular material is d_8-κ-$(ET)_2Cu[N(CN)_2]Br$, but the techniques should be readily transferable to other materials.

For Litsa, and my Mum and Dad

Acknowledgements

Many people have supported and helped me throughout the course of my DPhil. Thank you everyone, I could not have done it without you.

Formal thanks to Professor R. A. Cowley and Dr A. T. Boothroyd for extending the use of the facilities of the Clarendon Laboratory to me. I thank the EPSRC for funding my studentship and St. Cross college for the kind of support you hope for but don't expect.

I would like to thank my supervisors. John Singleton for getting me interested in organic materials, pointing me in the right direction and his boundless energy. Anne-Katrin Klehe for her invaluable insight into high pressure experimental physics, her belief that I could do anything with a little encouragement and always being willing to take time to discuss my work. Steve Blundell for taking up the reins in the final straight and giving me the guidance and support to complete the work you see before you.

At the Carnegie Institute of Washington Geophysical Laboratory and Brookhaven National Laboratory I would like to thank Russ Hemley, Alex Goncharov, Victor Struzhkin and Ho-Kwang Mao for allowing me to share their laboratory and expertise. I will always remember the road trip to get between the two labs.

Thanks to Mo Kurmoo, T. Sasaki, A. M. Kini and J. A. Schlueter for providing the many samples I would frequently destroy.

In the correlated electrons systems group I would particularly like to thank Ross McDonald for showing me the ropes with the Bruker spectrometer, superconducting magnets, programming matlab, data processing and helping me to get to know the little quirks of the group and how to deal with them; Paul Goddard for help with data analysis, latex for this thesis, his refreshing view on many subjects and showing me that it is really a small world; David Bakker for help with high pressure magnetoresistance experiments; Ishbel Marshall for being a friendly face when I first arrived; Moon-Sun Nam for reminding me that a thesis should not necessarily be mistaken for a telephone directory; Alessandro Narduzzo, Rachel Edwards and others for providing me with breaks from my own research, normally starting with "can you quickly align this sample...?" and Bill Hayes for valuable input in everything from feedback and proof reading my work to tea breaks. Thank you all of you for at least pretending to remember who I was when I did actually turn up for tea.

George and Rob in the Research Workshop for helping me build all the parts I needed for my research, and Reg, Simon and everyone else in the Main Workshop for those projects where my imagination and experimental requirements exceeded my machining skills. Peter Clack for tirelessly polishing and repolishing everything from sapphires to mirrors, no matter how many times I destroyed them or how exacting my standards. Thanks to Nigel Parker for always handling my last minute requests for helium with a smile.

Thanks to Bruker Spectroscopy for repeatedly repairing my spectrometer every time it broke. Without your help, I would not be finishing my research today. Anthony and Keith: I bet you are glad to finally see the back of me as you must have more free time now.

I would now like to thank all those people and things outside physics which have kept me sane.

Thanks to all the friends from my days as an undergraduate at Brasenose who generally first expressed incredulity that I was still going and then gave me encouragement whenever I saw them. Maybe some day soon I will be able to invite you round for dinner, I feel I have run up a giant "hospitality debt" over the last few years. To quickly name a few names: Jim, James, Sofia, Alex, Rob, Simon, Jonny, Phil, Dave, Natalie, Max, Mike, Joe, Emma, Alison, James, Martin and Ed (who I have known for a little bit longer).

Dancesport. My DPhil. would not have been the same without all the hard work, stress, triumphs and fun of competitive ballroom dancing. It provided a welcome change of scene when my experiments were not going as planned. Thanks to my coaches, Bruce and Vicky, for teaching me to dance and giving me the will to aim for the top and my partners over the years, Eleanor, Lindsay, Tiina, Litsa, Hazel and Kristen, for helping me get there. Thanks also to the whole team the year I was captain; the perfect victory record and the many nights I spent trying to sort out team politics are two things I won't forget! I miss the dancing, but not the 12 hours a week practice or the 5 am coach trips.

Lifesaving swimming. You guys are more than just a sports club with more socials than training and the legendary Christmas party (I fear there are still photos of me up on the website...)– I will have to make it back there one of these days. If you are an old fogey like me you probably got used to a pre-swimming warm up of three miles cycling uphill– university pool, who needs one?

Chris, my brother, I thank for continually reminding me that research working hours are really a walk in the park, for his invaluable help with job hunting enabling me to spend more time on this work and for being himself. I have made it through a DPhil. without beard and sandals so I am probably on the home straight now.

I thank my Mum and Dad for their continuing support throughout my whole education, for always encouraging my insatiable curiosity, even when I drove them mad in museums, and for always believing that I could do anything I wanted to.

Finally, thanks to my wonderful wife Litsa for always being there for me, supporting me in every way possible and showing me that true beauty is not to be found in a lab– I would not have made it this far without her.

Contents

Chapter 1

Introduction

1.1 Overview

In this thesis, I will describe my investigations into the properties of κ-phase BEDT-TTF charge transfer salts. Charge transfer salts are mainly studied as they are very useful test beds for fundamental physics due to the tuneability of their properties and ground states. I have primarily studied the effects of temperature and pressure on such systems as they allow access to a wide range of different states and properties. However isotopic substitution has also been used for some of the work. Transport properties of these systems have been studied to obtain information about the Fermi surface and effective mass, and the effect of deuteration and also change of pressure media will be discussed. The interaction of infrared radiation with these systems has also been investigated and here I will be presenting simultaneous pressure and temperature measurements, something not greatly studied due to the large technical challenges which I will also discuss. Infrared reflectivity is particularly useful as it allows the probing of low energy exitations and "fills the gap" left due to the different selection rules for Raman and neutron techniques. Chapter 1 provides an introduction to the organic materials themselves with particular emphasis on the actual compounds I have studied. Chapter 2 provides the necessary theoretical background for studying

them using magnetic quantum oscillations and their interaction with infrared radiation. Chapter 3 covers the experimental techniques and also discusses some of the challenges encountered and their solutions to aid others working in this area. Chapter 4 describes an investigation into the transport properties by studying Shubnikov-de Haas oscillations using two different pressure media, and comparing it to work done using a third. Chapter 5 presents an investigation into the pressure dependence of the phonon modes using infrared radiation in a deuterated sample. Chapter 6 presents what is believed to be the first pressure and temperature dependent infrared study of an organic molecular material.

1.2 Organic Molecular Metals

Until relatively recently, solid-state physics primarily studied inorganic compounds, alloys and elements- in other words, chemically simple materials. It was thought that fundamental physics should be concentrated on these "fundamental" materials. However, this meant missing out on some very exciting physics opened up by organic molecular materials. These are extremely complicated chemically, but their highly correlated natures, i.e. properties are dominated by many body effects, give rise to a range of instabilities which can result in a variety of ground states, everything from spin- or charge-density waves through ferromagnetic and antiferromagnetic to semiconducting and even superconducting states ([1][2][3]).

The field of organic superconductivity originated more than 40 years ago when Little [4] first suggested that it should be possible to make an organic polymer that would superconduct at room temperature. Unfortunately this has never been realized, but it has not stopped the field from continuing to grow. It is not the goal of room temperature superconductivity that makes these materials so widely studied, more the ability to tailor the bandstructure and the rich variety of fundamental physics easily available in these systems.

The first organic superconductor was discovered 15 years after Little's sug-

gestion. $(TMTSF)_2PF_6$ is electronically 1-dimensional with a $T_c \simeq 1K$ only at a pressure of 8 kbar. The first ambient pressure organic superconductor quickly followed, $(TMTSF_2)ClO_4$. The next generation of materials were designed to have a larger molecular overlap by giving each molecule a larger number of voluminous orbitals, enabling the formation of 2-D structures and superconducting transition temperatures ∼10 K, such as compounds based on bis(ethylenedithio)-tetrathiafulvalene (BEDT-TTF or ET for short) (Figure 1.1).

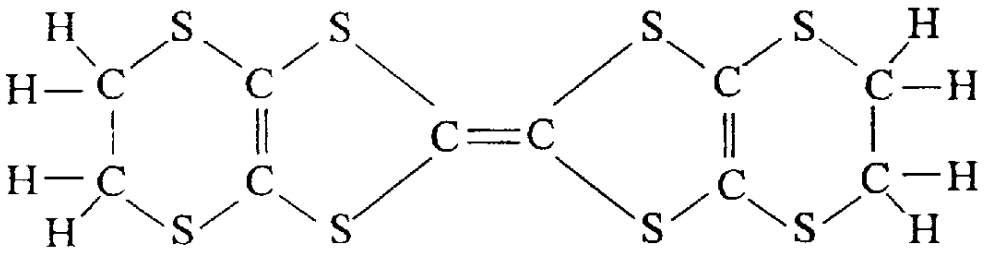

Figure 1.1: The BEDT-TTF molecule [5]

The properties of such molecules can be altered by either changing the organic building block (there are more than 60 currently) or by changing the ionic end groups and hence altering the packing of the structure. This allows a high degree of control over the band structure. For example κ-$(ET)_2Cu(SCN)_2$ is a 10.4K ambient pressure superconductor while $(ET)_2ClO_4(TCE)_{0.5}$ exhibits metallic behaviour down to 1.4 K. Pressure can be another way of altering these properties as it can be thought of as a method of continuously varying the molecular packing. It also helps that these materials are many times more compressible than a metal, allowing greater changes at relatively low pressures.

Much of the current work [1] in this field is devoted to charge-transfer salts, systems in which a number of molecules (the cation, or donor molecules) jointly donate an electron to the anion, resulting in a stable crystalline lattice and a free hole shared between the cations. This means that any resulting bands will only be

partially filled and hence the material will be metallic. Most charge-transfer salts have a highly layered anion-cation-anion structure and anisotropic bands from the overlap of the cation molecular orbitals.

1.2.1 BEDT-TTF charge transfer salts

The neutral ET molecule (Figure 1.1) is nonplanar, twisted at the central C=C bond [3]. When it forms part of a charge transfer salt it untwists and increases the packing density and become approximately planar (with only slight deviation in the outer two rings). The sulphur π orbitals are responsible for the wavefunction overlap [3] and the end hydrogens' interaction with the anion layer determine the exact structure. ET salts are found in three distinct packing arrangements, or phases, denoted by the symbols α, β and κ (see Figure 1.2)

Most compounds are of the form (BEDT-TTF)$_2$X, where X is an anion unit e.g. Cu(SCN)$_2$, each ET molecule donates half an electron leaving half a hole per molecule.

1.2.2 κ-phase BEDT-TTF charge transfer salts

A large amount of the work in this thesis is devoted to κ-phase salts, so they will be discussed here in some more detail. The BEDT-TTF molecules are arranged in dimers, which the direction of each dimer alternating (Figure 1.2). This gives an approximately isotropic inplane conductivity.

κ-phase salts are also interesting because of the large range of ground states accessible through temperature and pressure changes (Figure 1.3) The similarity between this and the phase diagram of high T_c superconductors (hole concentration replaces pressure on the horizontal axis) has been much commented upon with the suggestion of a non-BCS mechanism for the pairing. It is even possible that the mechanism will turn out to be identical to that in the high T_c materials and this is where another advantage of organic superconductors comes into play: they are much more ordered (as there is no doping to create disorder) with longer

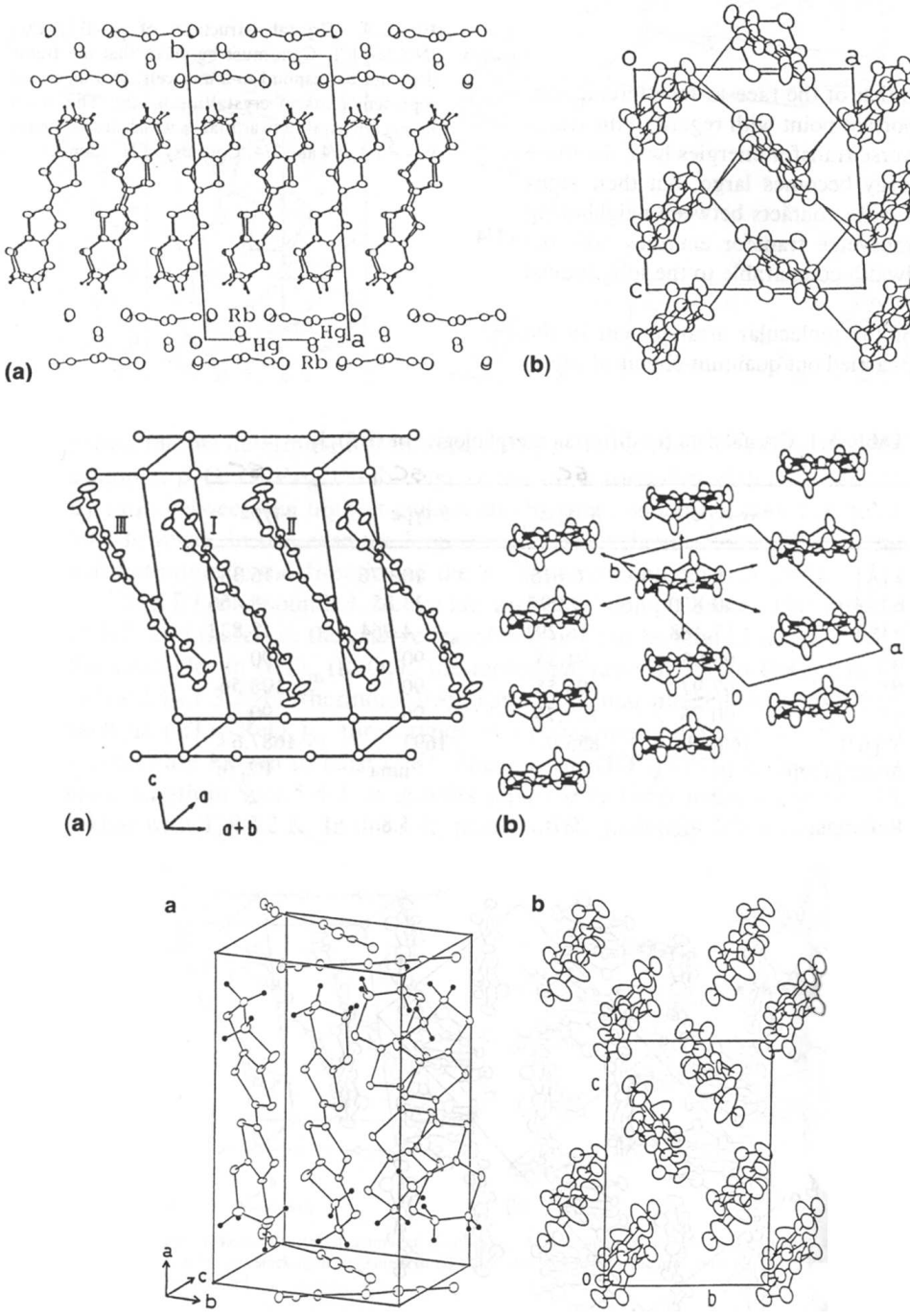

Figure 1.2: α (top), β (middle) and κ (bottom) phase packing arrangements for compounds of the BEDT-TTF molecule showing a 'side on' view (a) and an 'end on' view, indicating their in-plane packing arrangement (b) [3]

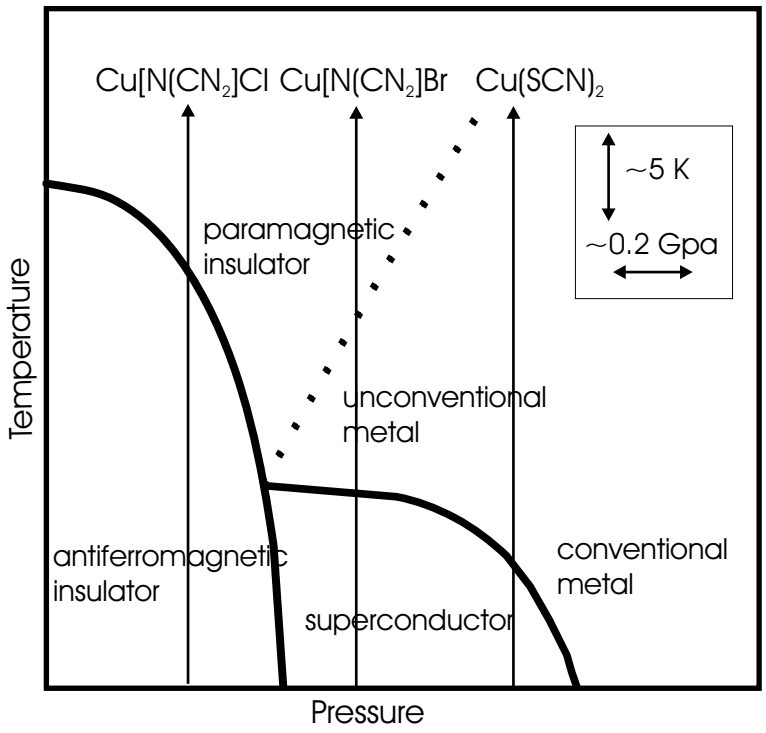

Figure 1.3: Schematic phase diagram of the $\kappa-(\mathrm{BEDT-TTF})_2\mathrm{X}$ family of organic superconductors, after [7]

mean free paths and have much lower critical fields than high T_c materials, allowing their Fermi surfaces to be probed with relative ease. In addition, their much higher compressibility allows tuning of properties for a given sample. As there are a wide range of techniques available to study these materials, it is hoped that the mechanism for superconductivity can be more easily pinned down, and when it is, that it will shed light on high T_c materials.

κ-$(\mathbf{ET})_2\mathbf{Cu(SCN)}_2$

κ-$(\mathrm{ET})_2\mathrm{Cu(SCN)}_2$ is one of the main materials covered in this thesis and so will be discussed here in some more detail. κ-$(\mathrm{ET})_2\mathrm{Cu(SCN)}_2$ is a superconductor with a T_c of 10.4 K [1]. The structure of this material is monoclinic and can be seen in Figure 1.4. Despite its complicated chemical formulation, κ-$(\mathrm{ET})_2\mathrm{Cu(SCN)}_2$, like all κ-phase charge transfer salts, has a relatively simple Fermi surface (Figure 1.5)

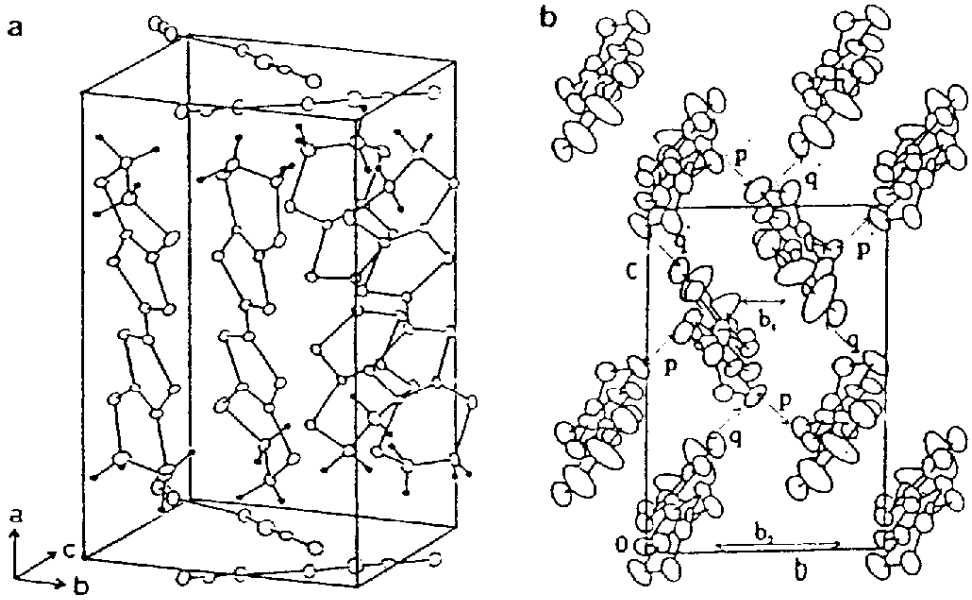

Figure 1.4: The structure of κ-$(ET)_2Cu(SCN)_2$, (a) unit cell, (b) κ-phase molecular packing from above [5]

and band structure.

Band structure calculations usually use the dimer as the base unit for a tight binding model [6]. Ionic bonding in the molecule leaves 1 hole per dimer and this results in a half full anti-bonding band. The bonding band is fully occupied and is shifted down in energy by approximately twice the energy of the intra-dimer transfer integral, t_1. t_1 is typically $\sim$ 250 meV and the band gap is about 0.5 eV [7]. t_2 and t_3, the inter-dimer transfer integrals, are of the order of 45 meV and 60 meV [8]. These can be used to calculate the dispersion of these bands, or bandwidth. As t_2 and t_3 are not the same, this leads to a slightly elliptical Fermi surface (Figure 1.5). The transfer integrals between differently oriented adjacent dimers are also different, i.e. $t_3 \neq t_3'$ (see Figure 1.6).

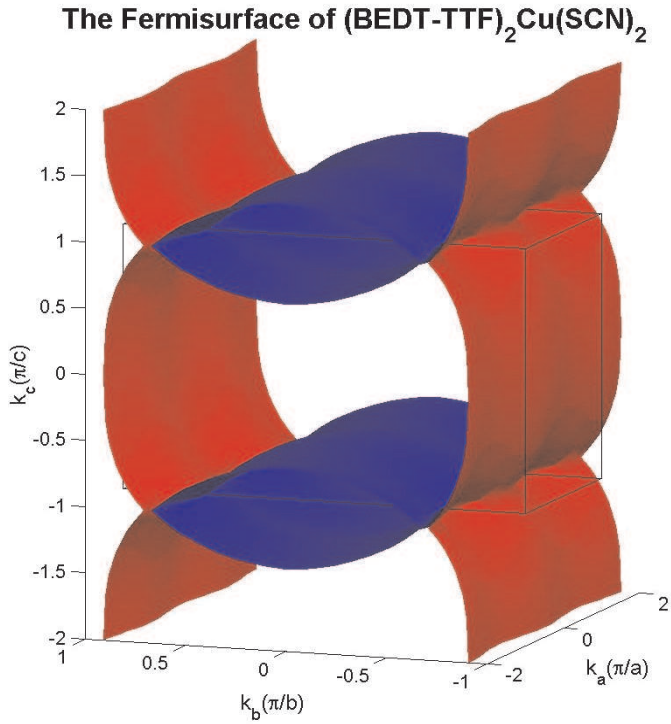

Figure 1.5: The 3D Fermi surface of κ-$(ET)_2Cu(SCN)_2$, Note the predominately 2-D structure, with small corrugations in the third direction due to a small but finite interlayer transfer integral (figure: R D McDonald)

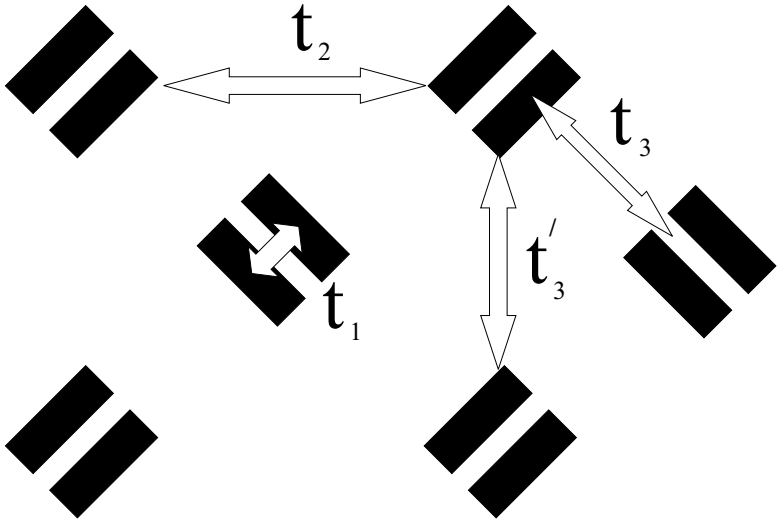

Figure 1.6: κ-phase molecular packing, showing the various transfer integrals

κ-BEDT-TTF$_2$Cu[N(CN)$_2$]Br

κ-BEDT-TTF$_2$Cu[N(CN)$_2$]Br displays very similar properties to κ-(ET)$_2$Cu(SCN)$_2$ and it is a superconductor with a T_c of 11.8 K [1]. However a difference is seen in the crystal structure– it is orthorhombic and the box enclosing the repeating structure with vertices parallel and perpendicular to the conducting planes does not correspond to a unit cell [3] (see Figure 1.7). The conducting plane is the ac-plane rather than the bc-plane seen with κ-(ET)$_2$Cu(SCN)$_2$

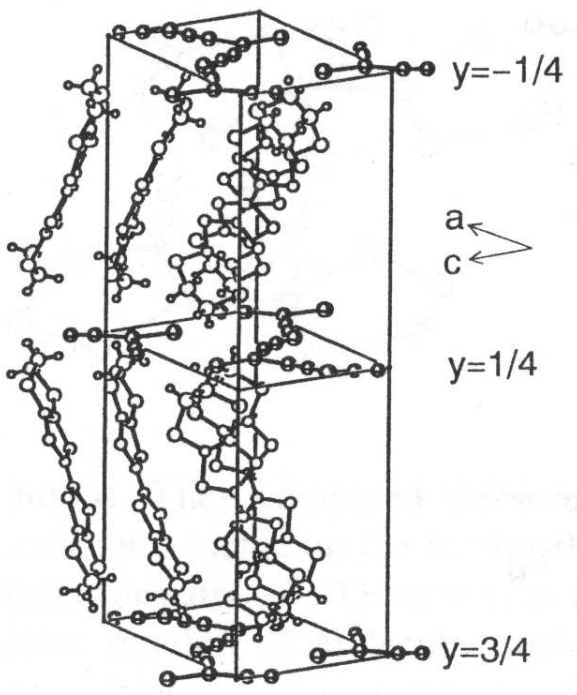

Figure 1.7: Crystal structure for κ-BEDT-TTF$_2$Cu[N(CN)$_2$]Br. Note, the box enclosing the repeating structure with vertices parallel and perpendicular to the conducting planes does not correspond to the unit cell. Anion layers are parallel to ac planes which are located at y=$-1/4$, $1/4$ and $3/4$ [3]

Chapter 2

Theoretical Background

2.1 Overview

In this chapter I review the theoretical work underlying the experiments performed in the rest of this thesis. Section 2.2 covers the mathematics which govern the response of a medium to infrared radiation, including the Kramers-Kronig relations, the Drude-Lorentz model and the extended Drude model. Section 2.3 deals with magnetic quantum oscillations and how they can be used to investigate the Fermi surface and calculate the effective mass. Finally, Section 2.4 shows how the effective masses acquired from different techniques relate to each other.

2.2 Infrared Response of media

2.2.1 Reflectance and Transmittance

Reflection and transmission of electro-magnetic waves are governed by their interaction with the electrons and nuclei of the sample being studied. From Maxwell's equations [9] in the presence of matter, we have that

$$\nabla \cdot \mathbf{D} = \rho_e, \tag{2.1}$$

where ρ_e is the charge density and the electric displacement $\mathbf{D}$ is given by

$$\mathbf{D} = \varepsilon_0 \mathbf{E} + \mathbf{P}, \tag{2.2}$$

where ε_0 is the permittivity of free space, $\mathbf{E}$ is the electric field strength and $\mathbf{P}$ is the polarization of the media (the vector sum off all the microscopic dipole moments in unit volume). It is possible to simplify this in the case of a simple isotropic dielectric by writing $\mathbf{P}$ as

$$\mathbf{P} = \chi \varepsilon_0 \mathbf{E}, \tag{2.3}$$

because $\mathbf{P}$ is parallel to $\mathbf{E}$. χ is known as the electric susceptibility. This allows us to write

$$\mathbf{D} = \varepsilon \mathbf{E}, \tag{2.4}$$

where

$$\varepsilon(\omega) = 1 + \chi(\omega), \tag{2.5}$$

$\varepsilon(\omega)$ is a second rank tensor and generally a function of frequency [16]. For an arbitrary polarization and propagation direction the response can be very complicated. Fortunately, the symmetry of crystalline systems greatly simplifies $\varepsilon(\omega)$ as, for measurements with the E-field along one crystal axis, the response is governed by a single component of ε. This is important as it allows the use of causality-derived relationships such as the sum rules and Kramers-Kronig integrals.

Solutions to equation (2.1) are of the form [10]

$$\mathbf{E}(\mathbf{r}, t) = \mathbf{E}_0 e^{i(\mathbf{k}.\mathbf{r} - \omega t)}, \tag{2.6}$$

where $\mathbf{E}_0$ is the electric field amplitude, $\mathbf{k}$ is the wave vector, and ω is the frequency. This leads to the dispersion relation for light polarization along a crystal

axis,

$$c^2\mathbf{k}^2 = \omega^2\varepsilon(\omega), \tag{2.7}$$

where c is the wave velocity. The dielectric response function, $\varepsilon(\omega)$, is used in the above dispersion relation to describe a dielectric medium. $\varepsilon(\omega)$ is complex,

$$\varepsilon(\omega) = \varepsilon'(\omega) + i\varepsilon''(\omega) = N^2(\omega), \tag{2.8}$$

where $\varepsilon'(\omega)$ and $\varepsilon''(\omega)$ are the real and imaginary coefficients of the dielectric response function respectively and $N(\omega)$ is the refractive index. Therefore $N(\omega)$ is

$$N(\omega) = n(\omega) + ik(\omega), \tag{2.9}$$

where $n(\omega)$ is the real refractive index and $k(\omega)$ is the extinction coefficient [27]. Equating real and imaginary parts in equation (2.8)leads to

$$\varepsilon'(\omega) = n^2 - k^2, \tag{2.10}$$

and

$$\varepsilon''(\omega) = 2nk. \tag{2.11}$$

The complex frequency dependent conductivity,

$$\sigma(\omega) = \sigma'(\omega) + i\sigma''(\omega), \tag{2.12}$$

is related to the dielectric response function by:

$$\varepsilon(\omega) = \frac{i\sigma(\omega)}{\varepsilon_0\omega}, \tag{2.13}$$

giving the real part of the conductivity to be

$$\sigma'(\omega) = -i\omega\varepsilon_0\varepsilon''(\omega), \tag{2.14}$$

and often the real components, σ' and ε', are used to describe metallic systems [16].

The above quantities can be linked to reflection and transmission using the Fresnel relations [27]. These are derived from the continuity of **E** and **H** fields parallel to an interface between two media. The subscript '1' denotes the first medium and '2' denotes the second. A more general angle dependent form can be derived, but this is not needed here as all experiments are performed at nearly normal incidence. From the Fresnel equations [27] the reflection r_{12}, and transmission, t_{12}, coefficients can be derived to be

$$r_{12} = \frac{N_1 - N_2}{N_1 + N_2} \tag{2.15}$$

and

$$t_{12} = \frac{2N_1}{N_1 + N_2}, \tag{2.16}$$

giving phase and amplitude information. By defining the reflectance, R, and transmittance, T, as the ratio of intensities the following relations are obtained

$$R_{12} = r_{12}^* r_{12} = \frac{(n_1 - n_2)^2 + (k_1 - k_2)^2}{(n_1 + n_2)^2 + (k_1 + k_2)^2} \tag{2.17}$$

and

$$T_{12} = \frac{N_2}{N_1} t_{12}^* t_{12} = \frac{4N_1 N_2}{(N_1 + N_2)^2} \quad . \tag{2.18}$$

Hence we need both R and T to determine N. Measuring both quantities on the same sample is not always possible, as a sample that has a large reflectance is almost certainly a poor transmitter and vice versa. One could obtain the relevant information by comparing two different angles of incidence. However this was not experimentally feasible, leaving only non-experimental methods for the extraction of the missing component. Each of these have their own advantages and disadvantages.

2.2.2 Kramers-Kronig dispersion relations

The dispersion relations are integral relations that link the real and imaginary parts of a function $f(\omega)$, which is analytic in the upper half of the complex plane [11]. For a frequency, ω_0, the Kramers-Kronig relations are

$$\mathrm{Re}[f(\omega_0)] = \frac{2}{\pi}\mathcal{P}\int_0^\infty \frac{\omega\ \mathrm{Im}[f(\omega)]}{\omega^2-\omega_0^2}\,d\omega \tag{2.19}$$

and

$$\mathrm{Im}[f(\omega_0)] = \frac{-2\omega_0}{\pi}\mathcal{P}\int_0^\infty \frac{\mathrm{Re}[f(\omega)]}{\omega^2-\omega_0^2}\,d\omega, \tag{2.20}$$

where $\mathcal{P}$ signifies the principal value of the integral and it is assumed that $f(\omega) \to 0$ as $\omega \to \infty$. Applying Kramers-Kronig relations to reflectance or transmittance measurements gives phase and amplitude information. This allows $n(\omega)$, $k(\omega)$, $\varepsilon'(\omega)$ and $\varepsilon''(\omega)$ to be calculated. From the integrals it is seen that it is necessary to integrate over all frequencies. When applying the Kramers-Kronig relations to determine, for example, the phase, the integrals will only be performed over a finite range of frequencies. Errors will be introduced in calculating quantities through the Kramers-Kronig relations and the results obtained can depend to a large extent on any extrapolation functions used.

2.2.3 Modelling the Dielectric Response Function

The Drude-Lorentz model

Instead of using Kramers-Kronig relations, it is possible to model the response of the medium using, in the first case, the Drude-Lorentz model. In this model, the permittivity $\varepsilon(\omega)$ is given by

$$\varepsilon(\omega) = \varepsilon(\infty) + \sum_j \frac{\Delta\varepsilon_j\omega_{Tj}^2}{\omega_{Tj}^2-\omega^2+i\omega\gamma_j} + \frac{\omega_p^2}{\omega(\omega+i\gamma)}. \tag{2.21}$$

Here, the second term on the right hand side is the contribution due to phonons and the third term is the Drude response. The phonon contribution is assumed to be a Lorentz oscillator and has the following components: γ_j is the damping of the jth mode, $\Delta\varepsilon_j$ is the oscillator strength of the jth mode and ω_{T_j} is the jth transverse optical eigenfrequency. This model (Equation 2.21) neglects interaction between modes. $\varepsilon(\infty)$ is a constant that allows for resonant effects at frequencies far above those measured. The behaviour of ε' and ε'' for a simple phonon response are shown in Figure (2.1).

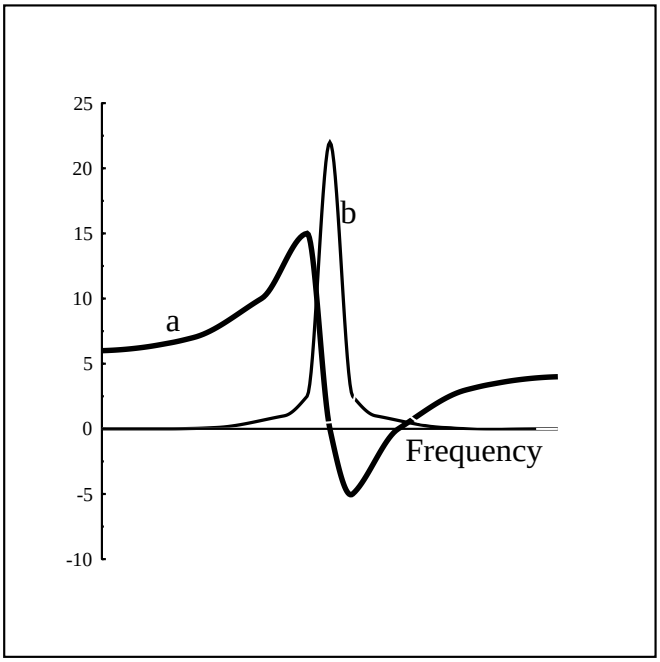

Figure 2.1: Dielectric response and loss function for a simple harmonic oscillator showing a) $\varepsilon'(\omega)$, b) $\varepsilon''(\omega)$

The Drude free electron model can be considered to be in the limit of zero phonon contribution in which the restoring force of a Lorentz oscillator is set to zero [12]; hence the permittivity $\varepsilon(\omega)$ is given by

$$\varepsilon(\omega) = \frac{\omega_p^2}{\omega(\omega + i\gamma)}. \tag{2.22}$$

When an external electric field is applied to a metal, the entire Fermi surface

is displaced by an amount proportional to the induced current density i.e. the free charge carriers accelerate until scattered. One of the main assumptions of this model is that we can use an average scattering rate, γ, and this governs the relaxation of the system to equilibrium, i.e. the state with average momentum $\langle \mathbf{p} \rangle = 0$ in the absence of external fields. γ is linked to the mean free path, l, by the Fermi velocity, $\mathrm{v_F}$ [16]:

$$\gamma \equiv \frac{1}{\tau} = \frac{\mathrm{v_F}}{l}, \tag{2.23}$$

where τ is known as the relaxation time. Scattering rates for independent processes add linearly,

$$\frac{1}{\tau} = \frac{1}{\tau_{impurity}} + \frac{1}{\tau_{phonon}} + \frac{1}{\tau_{electron}} + ... \tag{2.24}$$

The plasma frequency, ω_p, is the frequency at which $\varepsilon(\omega) \to 0$ in the absence of damping and this leads to a metal's high reflectance below the plasma edge. For a conventional Fermi liquid [12]

$$\omega_p^2 = \frac{n_e e^2}{\varepsilon_0 m^*}, \tag{2.25}$$

where n_e is the number of carriers of charge e and effective mass m^*.

The rate equation for this relaxation time is [10]

$$\frac{\mathrm{d}\langle \mathbf{p} \rangle}{\mathrm{d}t} = -\gamma \langle \mathbf{p} \rangle. \tag{2.26}$$

With an external $\mathbf{E}$ field this becomes

$$\frac{\mathrm{d}\langle \mathbf{p} \rangle}{\mathrm{d}t} = -\gamma \langle \mathbf{p} \rangle - e\mathbf{E} \tag{2.27}$$

Current density is given by $\mathbf{J} = -n_e e \langle \mathbf{p} \rangle / m^*$. In a DC field, $\mathrm{d}\langle \mathbf{p} \rangle / \mathrm{d}t = 0$ leading to

$$\sigma_{DC} = \frac{\mathbf{J}}{\mathbf{E}} = \frac{n_e e^2}{\gamma m^*}. \tag{2.28}$$

On the other hand, applying an AC field of the form $\mathbf{E}(t) = \mathbf{E}_0 e^{-i\omega t}$ and solving equation (2.27) leads to a complex, frequency dependent conductivity

$$\sigma(\omega) = \frac{n_e e^2}{m^*} \frac{1}{\gamma - i\omega}. \tag{2.29}$$

Fitting the parameters γ and ω_p can be ambiguous[1], so sometimes it can be advantageous to use the f-sum rule [15]

$$\frac{n_e}{m^*} = \frac{1}{2e^2} \int_0^\infty \omega \varepsilon''(\omega)\, d\omega. \tag{2.30}$$

or

$$\omega_p^2 = \int_0^\infty \sigma'(\omega)\, d\omega. \tag{2.31}$$

There is also a sum rule for the DC conductivity [15], this time related to the real part of the dielectric constant,

$$\sigma_{DC} = \int_0^\infty [\varepsilon'(\omega) - 1]\, d\omega. \tag{2.32}$$

The extended Drude model

Unfortunately, not every system in the metallic phase can have its conductivity accurately modelled by a simple Drude description. In organic molecular metals, such as studied in this work, electron-phonon and electron-electron interactions play a large part in their properties. Electron-phonon interactions may well effect the effective mass, but these interactions are only important at or below the frequencies of the phonons (these are typically in the infrared). Similar frequency dependent effects are seen for electron-electron interactions. Interband transitions can also contribute to the conductivity at low frequencies (again in the infrared). This means that the approximation that γ is independent of frequency does not

[1] With two unknowns, evaluating equation 2.22 in terms of real and imaginary parts can have more than one solution. This will be made worse by errors in experimental results, giving a range of values for each parameter.

hold true.

To try and allow for these effects, we can use a complex scattering rate Γ:

$$\Gamma(\omega) = \gamma'(\omega) + i\gamma''(\omega), \tag{2.33}$$

The real part can be interpreted as a modified electron-state life time and the imaginary part as a modified mass [17]. As the scattering rate and the mass are linked by a Kramers-Kronig transformation [10], this leads to a frequency dependent effective mass. When (2.33) is used in (2.29), the resulting model is known as the extended Drude model [10].

$$\sigma(\omega) = \sigma'(\omega) + i\sigma''(\omega) = \frac{\varepsilon_0\omega_p^2}{1+\lambda(\omega)} \frac{1}{\frac{\gamma'(\omega)}{1+\lambda(\omega)} - i\omega}, \tag{2.34}$$

where we define the dimensionless quantity $\lambda(\omega) = -\gamma''(\omega)/\omega$. This is of the same form as the Drude expression for conductivity (equation 2.29), but with a renormalized and frequency dependent scattering rate

$$\Gamma^*(\omega) = \frac{\gamma'(\omega)}{1+\lambda(\omega)}, \tag{2.35}$$

and a mass enhancement ratio of

$$\frac{m_{\text{eff}}}{m_b} = 1 + \lambda(\omega), \tag{2.36}$$

where m_{eff} is the enhanced effective mass in this model and m_{b} is the bare mass. These allow the conductivity to be written as

$$\sigma(\omega) = \frac{\varepsilon_0\omega_p^2}{\gamma'(\omega) - i\omega[m_{\text{eff}}(\omega)/m_b]}. \tag{2.37}$$

Rearranging equation 2.37 gives expressions for $\gamma'(\omega)$ and m_{eff}:

$$\gamma'(\omega) = \varepsilon_0\omega_p^2 \text{Re}\left(\frac{1}{\sigma(\omega)}\right) = \varepsilon_0\omega_p^2 \frac{\sigma'(\omega)}{\sigma'(\omega)^2 + \sigma''(\omega)^2} \tag{2.38}$$

and

$$\frac{m_{\text{eff}}(\omega)}{m_b} = \frac{\varepsilon_0 \omega_p^2}{\omega} \text{Im}\left(\frac{1}{\sigma(\omega)}\right) = \frac{\varepsilon_0 \omega_p^2}{\omega} \frac{\sigma''(\omega)}{\sigma'(\omega)^2 + \sigma''(\omega)^2}. \tag{2.39}$$

Now $\lambda(\omega)$ and $\gamma'(\omega)$ can be obtained from the Kramers-Kronig derived dielectric functions, or from a multiple oscillator fit to the spectra. A multiple oscillator fit may be preferable due to the difficulty of exactly fitting to the phonon modes of the system and the problems with finite frequency range. Some of the modes are very strong and hence any slight mismatch in the subtracted function can result in very sharp and narrow spikes being left over and incorrect extrapolation can result in a change in the underlying shape.

Note: This model only applies to itinerant carriers in the system so any phonon or interband contributions must be subtracted before calculating the frequency dependant mass enhancement ratio and scattering rate [18]. The value of ω_p^2 is determined using equation 2.31.

This renormalization is only effective at low frequencies, typically below the phonon frequency for electron-phonon interactions and below an effective reduced bandwidth for electron-electron interactions [10]. Equation 2.35 shows that, at high frequencies, the frequency dependent scattering rate will approach the frequency-independent value.

2.2.4 Infrared (IR) and Raman

The energies of IR correspond to those of low energy excitations of materials. For the materials studied in this work, this includes single particle excitations, collective modes and multi-particle excitations. IR radiation only interacts with small wave vector phonon modes due to conservation of energy and momentum [14].

For IR absorption to occur, the photon field, E, needs to excite a dipole moment, $\mathbf{P}$. This occurs if,

$$\langle \psi_1 | \mathbf{P} | \psi_2 \rangle \quad \neq 0. \tag{2.40}$$

If the ground state, ψ_1, is symmetric then only asymmetric modes are IR active as $\mathbf{P} = e.\mathbf{r}$ is a vector quantity, where $\mathbf{r}$ is the separation between the charges. Raman scattering can be used to examine the symmetric modes as scattering depends on the polarisability, α, a second rank tensor which can give rise to non-zero cross terms in the overlap integral. Only IR measurements have been studied in this thesis. However this does not mean that only asymmetric phonon modes have been studied. Some symmetric modes are visible in the IR due to electron-phonon coupling.

2.3 Magnetic Oscillations

Understanding of the Fermi surface of a metallic substance is important for explaining and calculating its basic properties, so experimental techniques that probe the Fermi surface are widely used. It is possible to probe the Fermi surface by investigating both oscillations in the magnetisation (de Haas-van Alphen oscillations) and in the magnetoresistance (Shubnikov-de Haas oscillations). This work will be confined to the latter, with the magnetic field at normal incidence to the crystal plane.

The organic molecular materials studied in this work have Fermi surfaces with *quasi*-2D and *quasi*-1D sections.

2.3.1 Quasiparticle motion in a magnetic field

The motion of a quasiparticle in a magnetic field B can be deduced using the Lorentz force equation [19]

$$\hbar \frac{d\mathbf{k}}{dt} = -ev \times \mathbf{B}, \tag{2.41}$$

where $\mathbf{k}(t)$ is the quasiparticle wavevector, $\hbar\mathbf{k}$ is the crystal momentum and v is the group velocity. This can be related to the energy by

$$\hbar v = \nabla_k E(\mathbf{k}), \tag{2.42}$$

where $E(k)$ is the energy of the quasiparticle and ∇_k is the gradient operator in wavevector space [19]. As the Fermi surface is a surface of constant energy, (2.42) shows that all quasiparticle velocities will be perpendicular to this surface. In the case where quasiparticles orbit on a closed loop of Fermi surface, they can possess velocity vectors which can point in any direction in a plane. They have freedom to move in two dimensions and hence are said to be *quasi*-2D. If they move on an open section, they have velocities parallel to a single direction and are *quasi*-1D [1].

Equations 2.41 and 2.42 imply that $\mathbf{k}_\parallel$, the component of $\mathbf{k}$ parallel to B, remains constant and that the energy remains constant i.e. the k-space of the quasiparticle is defined by the intersection of surfaces of constant energy with planes perpendicular to B. This means that for nearly all directions of magnetic field, B, quasiparticles on the closed sections of Fermi surface will be able to complete closed k-space orbits in the plane perpendicular to B. However, unsurprisingly, those on open sections will not. For the closed orbits it is possible to define a *cyclotron frequency* ω_c at which the quasiparticle will execute the orbit [1]. By comparing this to classical cyclotron motion it can be shown that [19]:

$$\omega_c = \frac{eB}{m^*_{cr}}, \tag{2.43}$$

where m^*_{cr}, the cyclotron mass, is defined as

$$m^*_{cr} = \frac{\hbar^2}{2\pi}\frac{\partial A}{\partial E}, \tag{2.44}$$

and A is the k-space cross-sectional area of the closed orbit.

The existence of a well defined frequency leads us (via the correspondence principle) to expect an associated system of quantum mechanical energy levels, known as Landau levels [19], separated by ω_c:

$$E(l+1, B, k_\parallel) - E(l, B, k_\parallel) = \frac{\hbar e B}{m^*_{cr}} = \hbar\omega_c, \tag{2.45}$$

where l is an integer quantum number which indentifies the Landau level. Combining 2.44 and 2.45 we get:

$$(E(l+1, B, k_\parallel) - E(l, B, k_\parallel))\frac{\partial A(E)}{\partial E} = \frac{2\pi e B}{\hbar}, \tag{2.46}$$

We can make the following approximation:

$$\frac{\partial A(E))}{\partial E} = \frac{A(E(l+1, B, k_\parallel)) - A(E(l, B, k_\parallel))}{E(l+1, B, k_\parallel) - E(l, B, k_\parallel)} \tag{2.47}$$

because we are interested in quasiparticles close to the Fermi surface, i.e. those with energies $\sim \mu \approx E_F$, where μ is the chemical potential and E_F is the Fermi energy ($E_F \equiv \mu(T = 0)$). For the fields used in this work ($< 20T$) the difference between adjacent levels ($\hbar\omega_c$) is much less than the energies of the levels themselves ($\sim \mu$) [1]. This allows us to rewrite equation (2.45) as

$$A(E(l+1, B, k_\parallel)) - A(E(l, B, k_\parallel)) = \frac{2\pi e B}{\hbar}. \tag{2.48}$$

From this is it clear than adjacent orbits of allowed energies and the same $k_\parallel$ enclose areas of k-space which differ by a fixed amount,

$$\delta A = \frac{2\pi e B}{\hbar}. \tag{2.49}$$

From this we get that the area enclosed by an orbit of allowed energy and $k_\parallel$ is given by:

$$A(E(l+1, B, k_\parallel)) = (1+\zeta)\delta A = (1+\zeta)\frac{2\pi e B}{\hbar}, \tag{2.50}$$

for $l >> 1$, where ζ is a constant ~ 1 [20] (for a parabolic band, it can be shown that $\zeta = \frac{1}{2}$ [5]).

This gives us the concept of "Landau tubes" which define the allowed k-space orbits (Figure 2.2).

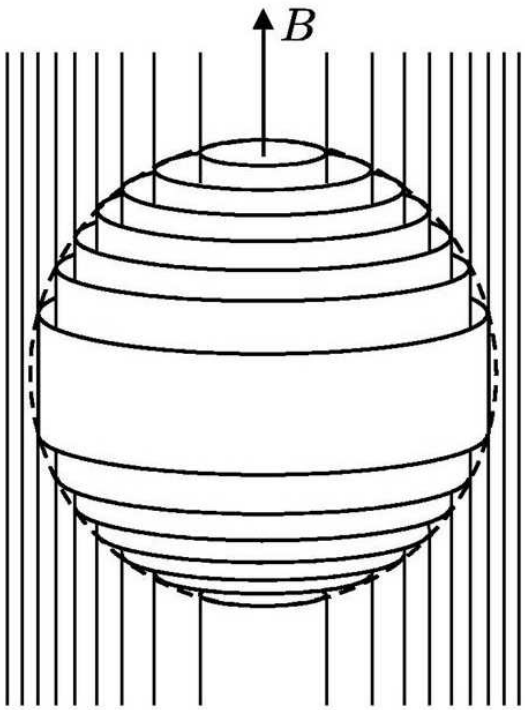

Figure 2.2: Landau tubes for the simple case of a spherical Fermi surface under an applied field. Increasing field will cause the outermost tube to pop out of the surface

The Fermi surface consists of occupied states lying on Landau tubes [19], rather than being quasicontinuous. From (2.50) it is clear that the k-space area (and hence degeneracy) of each tube increases with B, leading to tubes "popping out" of the Fermi surface. The tubes depopulate and the quasiparticles are accommodated by the remaining tubes within the Fermi surface [19]. This depopulation causes a change in the free energy and the largest changes occur when a Landau tube crosses an extremal cross section of the Fermi surface [19]. From equation (2.50)

this occurs when

$$(1+\zeta)\frac{2\pi eB}{\hbar} = A_{ext} \tag{2.51}$$

where A_{ext} is the k-space area of the extremal cross section. Therefore we will see periodic oscillations in the free energy in $1/B$ with a frequency [20] (in Tesla) given by

$$F = \frac{\hbar}{2\pi e}A_{ext} \tag{2.52}$$

These oscillations in the free energy/density of states are reflected in oscillations in the properties of the material studied and are known as magnetic quantum oscillations. This work will be confined to oscillations in the magnetoresistance (Shubnikov-de Haas effect). Each extremal orbit gives rise to a magnetic quantum oscillation frequency and this allows detailed information to be deduced about the size of the quasi-2D Fermi surface sections [2]. These frequencies are extracted by taking the Fourier transform of the oscillations.

2.3.2 Extracting the effective mass

The magnetic quantum oscillations of 2-D charge-transfer salts are widely analyzed using the Lifshitz-Kosevich formalism [2], which was developed for conventional 3-D metals [20]. The additional dispersion in the direction of the magnetic field results in much less distinct oscillations than in the 2-D case and hence one of the assumptions of the Lifshitz-Kosevich formula (LKF) is that the chemical potential, μ, is constant and that the oscillations in the free energy are small [20].

That this may not be the case for 2-D systems is of some concern. However a comparison of the results for the 2-D and 3-D forms [21] shows that, while the phase, absolute amplitude and the rate at which the amplitude of the oscillations grows with magnetic field change, the damping of oscillation amplitude with increasing temperature is not affected. This damping arises from "smearing out" of the Fermi-Dirac distribution of filled and empty states at finite temperatures. It results in less significant modulation of the density of states around μ, caused by

the Landau tubes moving though the surface. The thermal smearing also implies that we will only see oscillations at low temperatures ($\hbar\omega_c > k_B T$) [1] and this allows us to use the thermal 'phase-smearing' term, R_T, of the LKF to derive the effective mass, as long as the amplitude of the oscillations is small [22]. When this is the case, the temperature dependence of the oscillation amplitude, $\mathcal{A}$, is

$$\mathcal{A} \propto R_T = \frac{\chi}{\sinh\ \chi}, \tag{2.53}$$

where $\chi = 14.7 m^*_{cr} T/B$ and this allows us to relate the temperature dependence of the oscillations and m^*_{cr} [21]. 'Small' oscillations occur in these types of materials at magnetic fields of less than $\sim$ 30 T [1]. At fields above 30 T a full numerical simulation is required as the Landau levels become extremely sharp, resulting in large oscillations in μ.

2.4 Effective masses from different techniques

The mass from simple band structure calculations only includes renormalization due to the interaction of the electron with a static, periodic lattice. This gives a periodic potential and hence bands. However, the lattice is normally made up of charged ions or molecules and so the electron will introduce distortions into the lattice as it passes through. These Coulomb interactions can be thought of as virtual phonons surrounding the electron [1] and they increase its apparant mass. Cyclotron resonance experiments do not include any interactions between charge carriers [1], but do include interactions with the lattice, i.e. the average mass over one orbit is renormalized by electron-phonon interactions, but not by electron-electron interactions. Hence the mass from bandstructure calculations, m_b is related to the mass from cyclotron resonance experiments, m_{cr}, (known as a dynamical mass) by

$$m_{cr} \approx (1 + \lambda_e) m_b, \tag{2.54}$$

where λ_e is the electon-phonon coupling constant (this is typically between 0.1 and 1 for BEDT-FFT salts [1]). If we probe the mass by fitting the temperature dependence of magnetoresistance oscillations (the Shubnikov-de Haas effect), the electron-electron interactions need to be taken into account as well [1]. This gives the effective mass, m^*, to be

$$m^* \approx \left(1 + \frac{F_s^l}{3}\right) m_{cr}, \tag{2.55}$$

where F_s^l is a constant known as a Fermi-liquid parameter [24]. However, if the plasma frequency is measured optically, the mass calculated is

$$m_{opt} \approx m_b. \tag{2.56}$$

This is because the electron is excited from its ground state so the contribution from surrounding electrons and virtual phonons is negligible [1].

Chapter 3

Experimental Details

3.1 Overview

In this chapter I shall discuss the experimental apparatus used for the work in this thesis, as well as any practical difficulties encountered, and how they were overcome. Section 3.2 is a brief overview of Fourier transform spectroscopy. Section 3.5 covers the Bruker Fourier transform spectrometer, used for all the infrared measurements and all the cryostats used for low temperature infrared measurements. Finally, section 3.4 deals with high pressure techniques and the three different pressure cells/systems used for this work.

3.2 Fourier transform spectroscopy

The Fourier Transform (FT) spectrometer is based on a Michelson interferometer, where a beam of broad band radiation is divided by a beamsplitter. These two beams then follow different paths through the optical system and are recombined at the output. Interference results due to the differing phase introduced by the path difference. In the FT spectrometer, this path difference is continually varied by an oscillating mirror (Figure 3.1).

The frequency components present in the light affect the interferogram. For

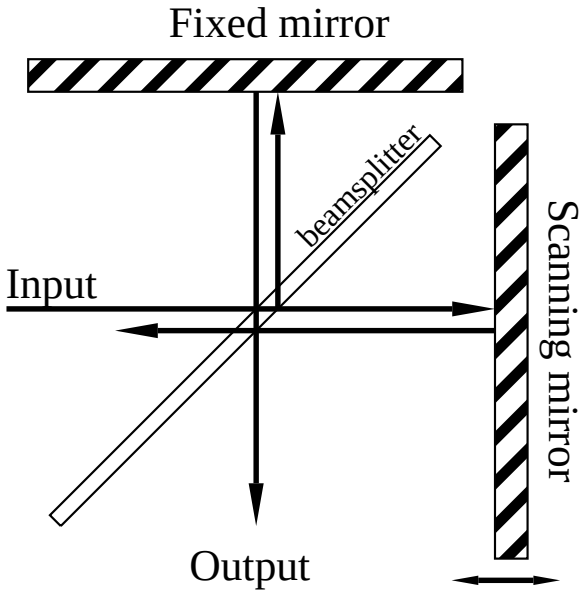

Figure 3.1: A simplified Michelson interferometer.

example, a monomodal laser beam gives a pure sinusoidal interferogram as it is a coherent delta function of frequecy. The interferogram from a sample is much more complicated, containing many frequency components (see Figure 3.2).

FT spectrometers use a laser to track the moving mirror, as the sinusoidal interferogram allows its position and velocity to be determined exactly. This is essential as it ensures the correct addition of interferograms, so the signal increases faster than the random noise, as well as allowing correct interpretation of the interferogram [25]. The signal to noise ratio (S/N) increases as the square root of the number of scans.

FT spectrometers, despite their name, do not perform a Fourier transform of the light (unlike many other spectrometers). A computer performs the Fourier transform of the signal from the spectrometer and this gives the spectrum. The FT spectrometer was invented by Michelson at the end of the 19^{th} century, but a lack of sensitive detectors and Fourier transform algorithms calculable using pen and paper made it impractical. Their use has greatly increased since the advent

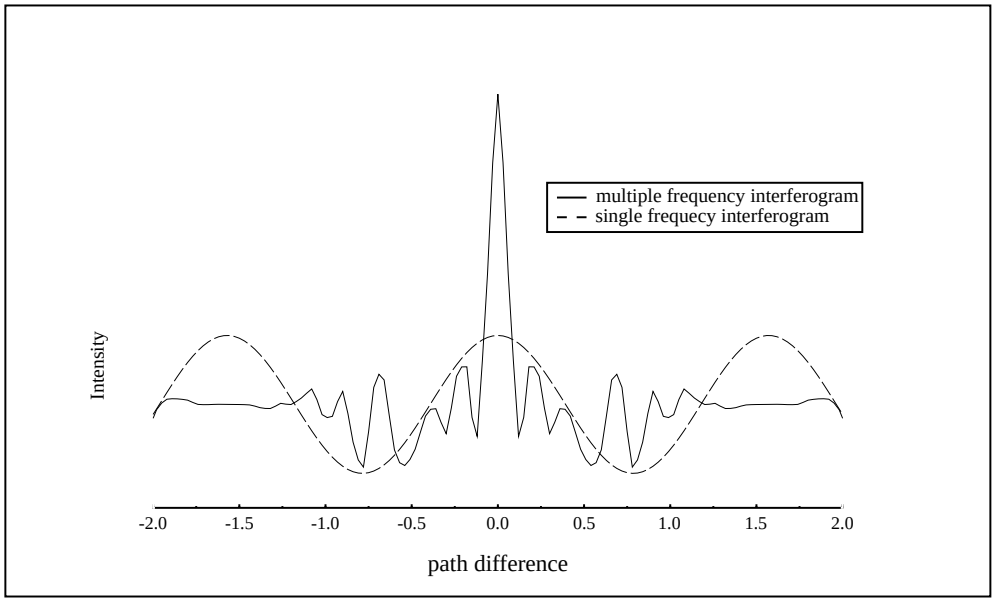

Figure 3.2: sample interferograms.

of modern computers.

For both reflection and transmission spectra, the sample is placed in the path of the beam between the interferometer and detector. Absolute values are calculated by dividing the spectrum by a background, i.e. one with no sample present. For IR reflection a gold mirror is used, as gold is a near perfect reflector in this range. The vast majority of my samples are opaque and so most of my experiments have been reflection studies.

A spectrum is obtained by taking an inverse Fourier transform of the interferogram. The Fourier transform of a function, $F(x)$, is defined as:

$$A(v) = \int_{-\infty}^{\infty} F(x) e^{+i2\pi vx}\, dx \equiv \mathcal{F}\{F(x)\} \quad , \tag{3.1}$$

and the inverse of this function is:

$$F(x) = \int_{-\infty}^{\infty} A(v) e^{-i2\pi vx}\, dv \equiv \mathcal{F}^{-1}\{A(v)\} \quad , \tag{3.2}$$

Equations 3.1 and 3.2 are valid if:

1. $F(x)$ is finite everywhere; discontinuities are finite in size and number.

2. The derivatives of $F(x)$ and $A(v)$ must exist except at a finite number of points, and then, the left and right derivatives must exist.

3. $\int_{-\infty}^{\infty} |F(x)|\, dx < \infty$ i.e., $F(x)$ is absolutely integrable.

To find the resolution limit of the spectrometer, we must consider two closely spaced spectral lines. Changing the optical path difference makes the interferograms of the two lines go in and out of phase. This is observed as a beat frequency that enables us to resolve the lines. If the path difference changes by the reciprocal of the beat frequency one complete period will be observed in the combined interferogram, meaning the lines can just be resolved. The maximum resolution is therefore limited to the reciprocal of the maximum change in optical path length, Δx [25].

Since Fourier integrals have infinite limits, an error will be introduced when computing a spectrum as the moving mirror can only have a finite displacement, leading to a finite optical path difference. This has the same effect as its convolution with a 'top hat' function: we see broadened spectral features and sidelobes. To visualise this, consider a monochromatic source. The inverse Fourier transform of this is a sinusoidal interferogram, as previously discussed. The intensity can be represented as the FT of two delta functions, one at ω_1 and one at $-\omega_1$, as the symmetric limits make it mathematically elegant. Thus the intensity, $I(x)$, is given by

$$I(x) = \int_{-\infty}^{\infty} 1/2[\delta(\omega - \omega_1) + \delta(\omega + \omega_1)]e^{i2\pi\omega x/c}\, d\omega = \cos(2\pi\omega_1 x/c), \qquad (3.3)$$

where x is the path difference. This gives a sinusoidal interferogram.

The path difference is twice the maximum mirror displacement, $\Delta x = 2L$, so, using symmetry and the Euler relation [1], this gives the inverse Fourier transform

[1] Euler's relation is: $e^{ix} = \cos x + i \sin x$

to be:

$$I(\omega) = \int_{-L}^{L} 2\cos(2\pi\omega_1 x/c)e^{-i2\pi\omega x/c}\,dx = \int_{-L}^{L} 2\cos(2\pi\omega_1 x/c)\cos(2\pi\omega x/c)\,dx \tag{3.4}$$

The solution of this can be obtained with the aid of trigonometric identities[2]:

$$I(\omega) = 2L[\mathrm{sinc}\{2\pi(\omega_1+\omega)L\} + \mathrm{sinc}\{2\pi(\omega_1-\omega)L\}] \tag{3.5}$$

Here the second term is dominant, giving a peak at ω_1, but with pronounced side lobes which would be interpreted as false intensity in adjacent frequencies. This can be partially prevented by multipling the interferogram by an apodizing function [25] (Figure 3.3). Apodization means literally "removing the foot" and is where a discontinuity at the edge of a function is smoothed or removed by using a window function.

Figure 3.3 uses a triangular window function because it is easy to see what is happening. Unfortunately, triangular apodization only gives positive side lobes and there are other functions that give equally good resolution and smaller side lobes so it is generally avoided. A Blackman-Harris three term function removes all the side lobes at the expense of a 50% increase in the half-height line width of a resolution-limited spectral feature [25]. It is good for general purpose spectroscopy at moderate resolution and is the function I mainly used.

The sharper the feature present in a spectrum, the higher the frequency components of the interferogram needed to interpret its true line shape [26]. Hence sampling frequency plays an important role in the accurate representation of a spectrum. The basis for this can be seen in Figure 3.4, the continuous line represents an interferogram which has been sampled at the points indicated by the black dots. This leads to an incorrect frequency being measured and this frequency cannot be separated from any real components at this frequency. In real spectra, it is rarely

[2] $\cos(a)\cos(b) = 1/2[\cos(a+b) + \cos(a-b)]$

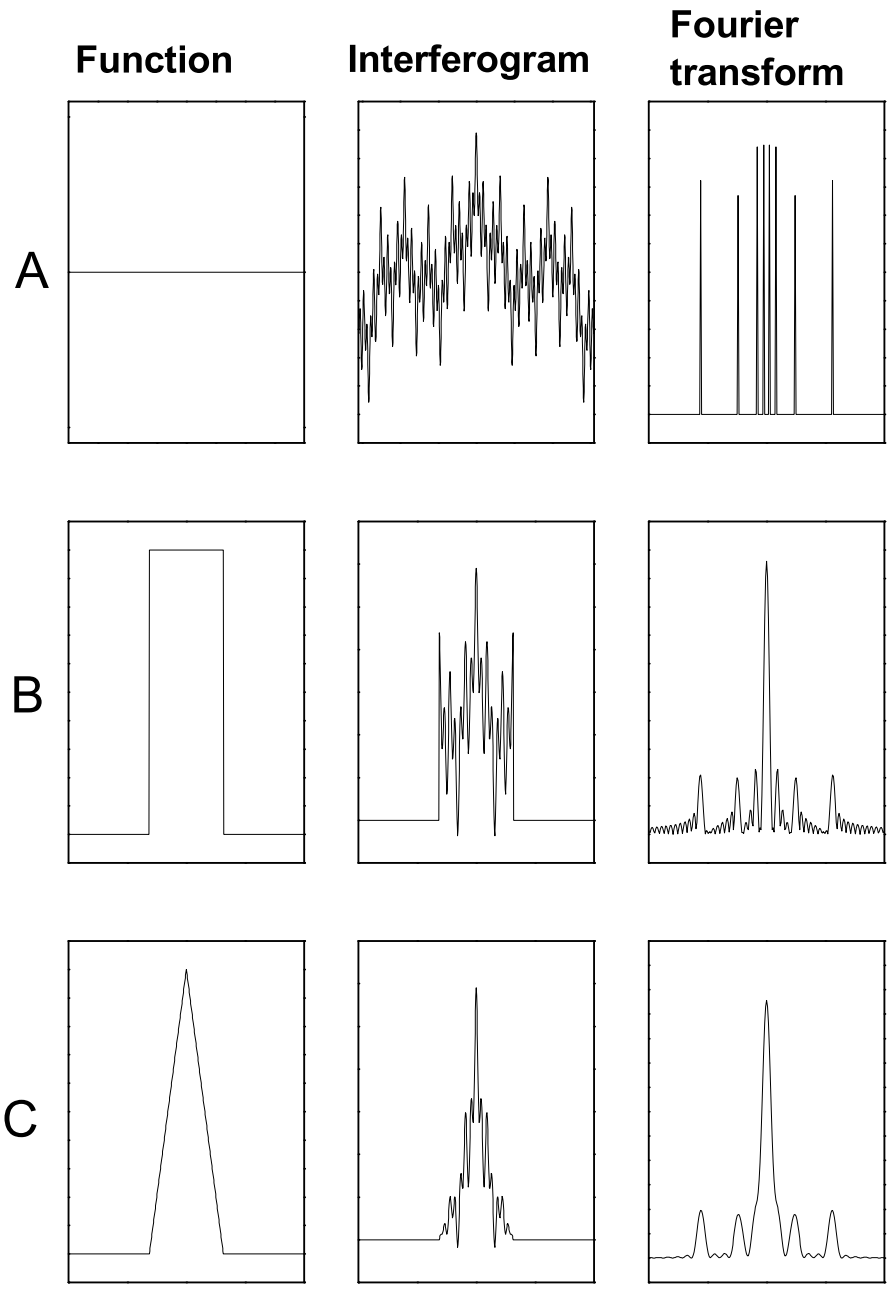

Figure 3.3: Showing the effects of triangular apodization. Initally, in cases A, B & C an interferogram of infinite length is taken. The first column shows the function this is convolved with, the second shows the resulting interferogram and the final column shows the Fourier transform of this function. Row A shows the case of an infinite function leading to sharp δ-functions in frequency, Row B shows the physically more realistic case of a finite mirror displacement- i.e. convolution with a "top-hat" function, showing a wide range of additional, false frequencies and Row C shows the benefits of a triangular apodization fuction- a reduction in false intensities, at the cost of a broadening of the peaks.

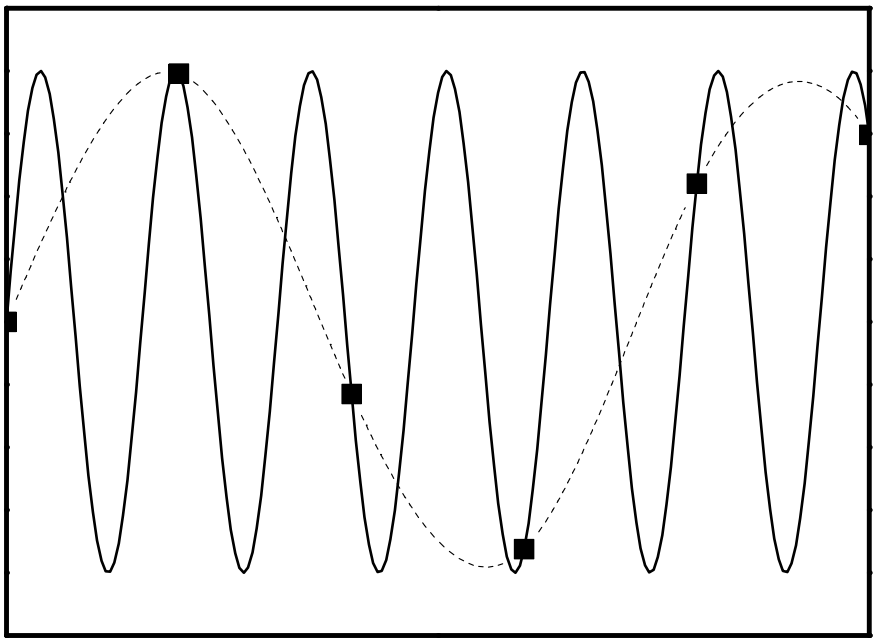

Figure 3.4: Sampling of a interferogram (continuous line) at too low a frequency (the black squares) leads to an incorrect frequency being inferred (the dashed line).

as neat as this due to many different frequencies being affected. The loss of such high frequency components due to insufficient sampling results in a broadening of the spectral lines and is known as spectral folding or aliasing. However, this is not generally a problem with this apparatus as the interferogram is sampled at a high enough multiple of the laser interferogram zero-crossing frequency to prevent this.

Before computing the spectrum, the interferogram is renormalised by subtraction of the intensity due to incoherent interference. At zero mirror displacement, the waves from all frequencies will interact coherently. At infinite mirror displacement, the waves, when recombined, are separated by more than a wave-train length and will therefore interact incoherently. In practice the incoherent intensity is obtained by scanning the mirror at large displacements, $x \rightarrow \infty$. This is useful if the interferometer is not perfectly aligned, in which case there will be an additive intensity error, ΔI, reaching the detector. The coherent interference intensity, $I(0)$, of n equal waves of

electric field E, is proportional to n^2E^2, the sum of the beams' individual electric fields squared, whereas the flux from incoherent intensity, $I(\infty)$ is proportional to the sum of the individual intensities, nE^2. As there are two beams, $n = 2$, the renormalised interferogram $I(x) - \frac{1}{2}I(0)$ [25] may be written as $I(0) - I(\infty)$. An additive error thus cancels out when the interferogram is redefined as the fluctuation about the large mirror displacement intensity:

$$[I(x) + \Delta I] - [I(\infty) + \Delta I] = [I(x) - I(\infty)] \tag{3.6}$$

Further problems can arise if the exact mirror displacement that corresponds to an identical optical path length for both arms of the interferometer is not known when computing the spectrum. A Fourier transform performed with the wrong origin leads to a 'phase sampling error' which can be seen as a major distortion of the lineshape. This displacement is determined to be that giving a maximum to the interferogram. It is particularly important to get this right when using the interferometer in 'single-sided' mode as it only measures in one direction and assumes the calculation to be symmetric about this point.

3.2.1 The advantages of Fourier Transform Spectroscopy

The Fourier transform spectrometer, while having disadvantges such as requiring computing power, has two distinct advantages that more than make up for this:

1. The Jacquinot, or throughput, advantage [25]. This states that in a lossless optical system, the brightness of an object equals the brightness of the image. The FT spectrometer closely resembles this ideal and thus there is a much higher flux reaching the detector than in, for example, a grating spectrometer where a small aperture is needed for good resolution.

2. The Fellgett or multiplex advantage [25]. This can be explained by considering the resolution, $\delta\omega$, or number of spectral elements, M, in the frequency range $\Delta\omega$, which is

$$M = \Delta\omega/\delta\omega. \tag{3.7}$$

If a grating or prism instrument is being used, each small band of width $\delta\omega$ can only be observed for a time t/M, where t is the total observation time. The signal from each element is proportional to this time and hence the signal to noise ratio is proportional to $\sqrt{t/M}$. However, in the case of a FT instrument the entire spectrum is observed for time t and hence the signal to noise is proportional to $\sqrt{t}$, a factor of $\sqrt{M}$ higher. This is true in the IR, where detector noise dominates, but this advantage is lost when using the visible or UV as the better detectors in these ranges allow individual photons to be detected. The noise is governed by statistical fluctuations in the number of photons emitted and this only depends on source intensity leading to signal to noise being proportional to $\sqrt{I}$. The Jacquinot advantage is not affected so FT interferometers still have a larger throughput in the visible.

3.3 Bruker IFS 66v

The spectroscopic work in this research has been carried out, for the most part, using a Bruker IFS 66v Fourier Transform Spectrometer, the layout of which is shown in figure 3.5, with a Spectratech IR microscope attached. If the sample is mounted in the main sample chamber then the instrument can be evacuated. For smaller samples, or samples mounted in a pressure cell, the microscope is needed so the system is purged with nitrogen, as it cannot be sealed. Strong CO_2 and water bands in the mid-IR and large amounts of water noise in the far-IR make this essential for a good signal. Another advantage lies in increased repeatability, as the air in the room can change over the course of a long run, leading to increased noise. The instrument and sample chamber have separate pump access and vents so the sample can be changed without having to repump the rest of the interferometer.

The instrument has three different lamps for different ranges:

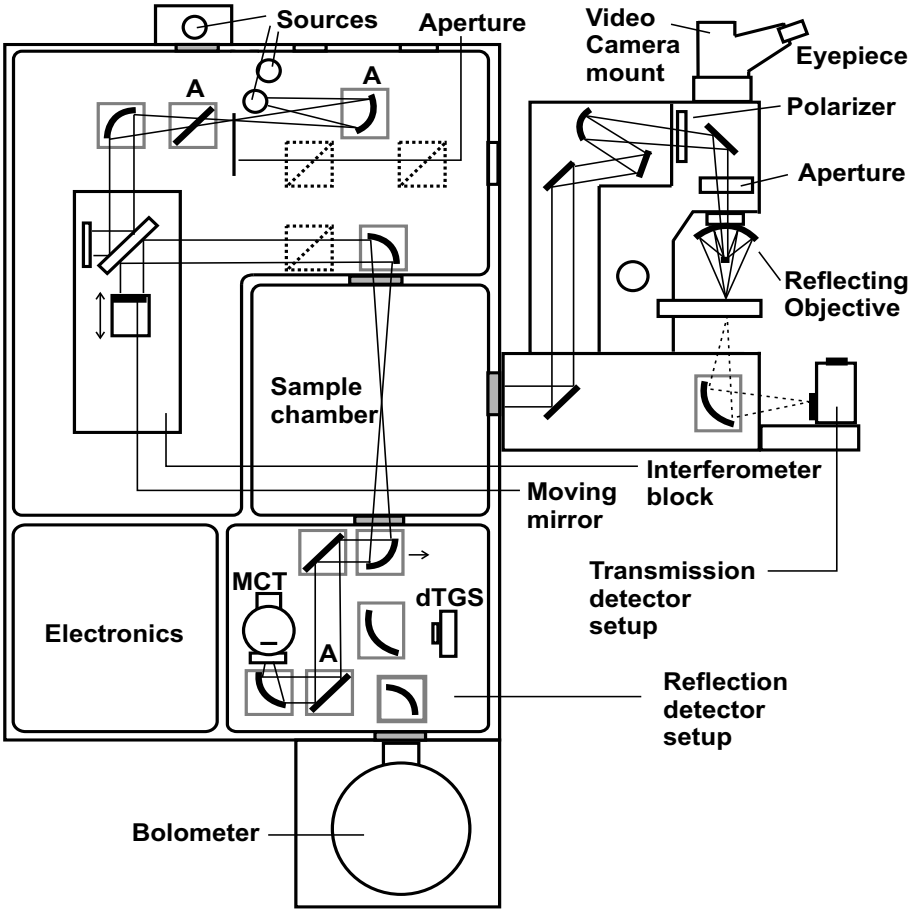

Figure 3.5: General schematic of Bruker IF66v and Spectratech IR Microscope. Mirrors marked A rotate under computer control for different source and detector combinations. Note that, in reality, the microscope is perpendicular to the plane of the spectrometer

- a tungsten lamp for the near IR, 6000 cm^{-1} and upwards
- a glowbar lamp for the mid-IR and some far-IR, 100-7500 cm^{-1}
- a mercury vapour lamp for far-IR 10-120 cm^{-1} .

These lamps can be apertured prior to the beam entering the interferometer to aid collimation and prevent overloading the detector. However this is only useful when the microscope is not being used. The maximum aperture size is 12 mm and this places a limit on the resolution of $\delta\omega = 0.1\,\mathrm{cm}^{-1}$ at $100\,\mathrm{cm}^{-1}$ and $\delta\omega = 1\,\mathrm{cm}^{-1}$ at $1000\,\mathrm{cm}^{-1}$, a far higher resolution than we used.

There are several beamsplitters to cover this range:

- a silicon film on a quartz substrate for the near visible, 5300–25000 cm^{-1}
- silicon on a calcium fluoride substrate for NIR, 2000–10000 cm^{-1}
- germanium on a potassium bromide substrate for MIR, 550–7500 cm^{-1}
- a germanium on mylar for 50–600 cm^{-1}
- free standing mylar films 10–500 cm^{-1}

A slightly different (and critical) alignment of the mirrors is needed for each of the beamsplitters and moving between each is controlled by the software through stepper motors. The moving mirror rides on a nitrogen cushion and is tracked with a HeNe laser, reflected off, and transmitted by, a partially silvered spot in the centre of the beamsplitters and detected by two photodiodes.

There are detectors to cover these ranges, both cooled and non-cooled. The detectors that are not cooled are of limited use for the present experiments due to the high levels of noise and low sensitivity and they are:

- A pyroelectric dTGS detector for FIR
- a second dTGS with a different window for MIR
- a silicon diode for NIR and visible

Most of the time, the following cooled detectors are used:

- a liquid nitrogen cooled InSb detector for NIR
- a liquid nitrogen cooled MCT detector for MIR. This has a high-gain amplifier built in to aid with small signals from samples.
- a liquid helium cooled silicon bolometer with a hold time of more than 24hrs. This is generally used in the FIR although it could be used for some of the MIR.

The arms of the interferometer are at 90° to each other and this leads to different beam strengths in the horizontal and vertical directions. This is due to the difference between the Fresnel relations for s- and p-polarized light [27]. In practice one is about $2/3$ the strength of the other so both axes can be used for measurement of an anisotropic sample. If one axis is a much worse reflector than the other, it is advantageous to align the strong sample axis with the weak beam axis. The polariser, not the sample, is rotated.

3.3.1 The sample chamber

Light enters the sample chamber through the aperture at one side, is focused in the middle and then leaves through the aperture on the other side. Large samples can be placed in a mount at this focus for transmission and for reflection. For the latter I modified and used a reflection rig that fits in the chamber (Figure 3.6). With this, the roof-shaped mirror directs the light from in the plane of the interferometer upwards to be reflected off the sample and then back into the plane of the instrument again. With this setup, the instrument can be pumped down. A small metal disc with an indent covers the sample so it does not blow away when pumping or venting. Crystals down to 0.6 mm^2 have been measured using this arrangement.

There is also an Oxford Instruments continuous flow cryostat that can be fitted in the lid of the sample chamber so that the window lies in the path of the beam. This can be used for larger samples (> 4 mm^2) and has a range of RT$\rightarrow 10$ K. However, very few of the organic molecular crystals studied are anywhere near this size so a more complex setup is needed.

3.3.2 SpectraTech IR microscope

For smaller samples we need to be able to visually focus, adjust and aperture the beam and an IR microscope allows us to to do this, as well as closely spaced sample and background measurements. I spent considerable time and effort redesigning and modifying the system to get it to work well. First we needed to get the beam out of the

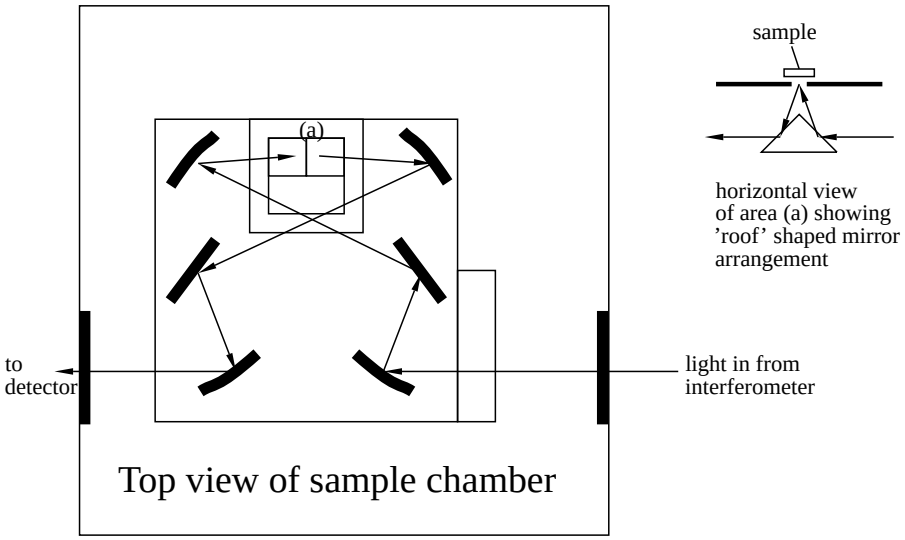

Figure 3.6: Reflectivity mirror set

Bruker sample chamber and into the microscope. This is done using a setup of mirrors (Figure 3.7) that allows the beam to be reflected out the side port of the sample chamber and then back in, while making sure that the beam is still perpendicular to the entrance and exit aperture of the sample chamber. The beam then passes into the microscope and through a reflecting objective lens, allowing focusing down to a small spot on the sample. The much longer path through the microscope results in a larger spot size so most of the main mirrors in the microscope and the sample chamber were replaced with larger ones. This altered many of the focal lengths necessitating many of the positions of the mirrors being altered. Some clipping of the beam still occurs, but the overall throughput of the system is much increased.

The microscope has also been modified to allow transmission experiments. A 45° gold coated focusing mirror is mounted below the translation stage and detectors are mounted onto the microscope (see Figure 3.5) using the external channel from the Bruker and an extension cable. This was relatively simple for the MCT and InSb detectors, but the much larger size and weight of the bolometer presented much larger design challenges. The best solution involved partially replicating the design of the

Bruker's original bolometer mount and bolting it to the front of the microscope, to maintain alignment, and clamping it to the bench, giving it sufficient support.

Most of the low temperature work has been done using a couple of external cryostats in conjunction with the side port of the microscope.

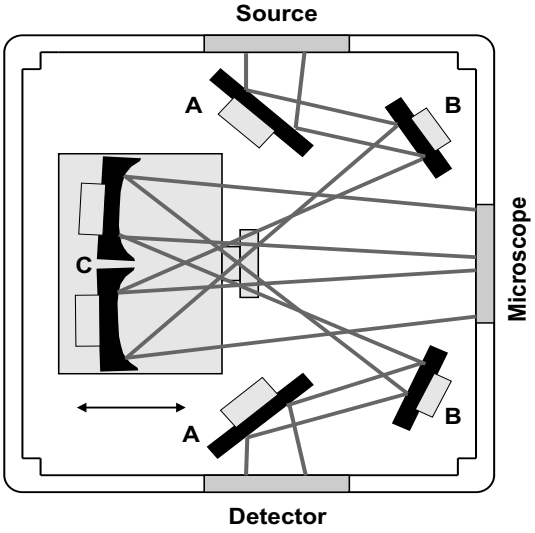

Figure 3.7: Mirror setup for using the microscope. Mirrors A are fixed, B are adjustable with screws on the back and C are adjustable and can be moved forwards and backwards

3.3.3 System Alignment

Mirrors, instead of lenses, are used throughout the system because they eliminate chromatic aberration, which is caused by the refractive index varying with frequency, and also allow observation of the sample, as lenses to focus in the mid and far IR are opaque in the visible. Other deviations from Gaussian optics are due to the breakdown of the paralaxial approximation for deriving the focal lengths of optics. This relies on the small angle approximation for sin and cos and it is true for rays close to, or making small angles to the optical axis. These aberrations arise from the higher order terms in the power expansion and are spherical aberration, coma, astigmatism (these three deteriorate the image, making it unclear), distortion and field curvature (these two deform the image) [27].

Aberrations that distorts the image are not really a concern as they are monochromatic in nature and a FT spectrometer relies on a single element detector so, up to a point, spatial distortions have no effect. However distortion that increases the spot size to much larger than the detector element and/or creates a frustrated minimum is more of a problem and virtually impossible to eliminate.

Off-axis focal mirrors are much harder to align than lenses as they are designed to work at a particular angle; they have different horizontal and vertical curvatures which only produce a single focal plane when viewed at the correct angle. The incoming beam direction and the needed beam steering using the mirror may not be (and in practice never are) at the correct angle for perfect focusing, with astigmatism and coma leading to a frustrated minimum.

Spherical aberration is also a problem as our globar source is neither sufficiently point like or bright. The only way round this is to use a synchrotron as a source. Unfortunately, when we tried this at the Brookhaven National Laboratory in the USA using their Synchrotron Light Source, the highly coherent nature of such a source caused major interference problems between window and sample, preventing us from obtaining useful results. If this problem could be surmounted, then the vastly increased intensity would be very useful for our small and not very reflective samples. Further spherical aberration is caused by the optically thick windows needed for the cryostats and the diamond anvils in the pressure cell. The reflecting objective is able to at least partially compensate for this by adjusting the separation of its two mirrors.

Alignment of the system is complicated by the fact that the optics are in a 3 dimensional arrangement (the sample chamber mirrors are in a horizontal plane and the microscope a vertical one) and that the whole system has to be slightly misaligned to work. This is because the mirrors in the sample chamber that send the beam out of and receive it back through the side port to the microscope have centres which are about 5 cm apart, so the beam needs to be at a slight angle (Figure 3.7) so this distance is covered over the $\sim$1.5 m path through the microscope. This requires a narrow, collimated beam and since we cannot have both some trial and error is

involved. Normally we have a compromise where maximising the intensity at the detector, i.e. optimizing the throughput, is sufficient.

3.3.4 Optical Cryostats

Most of the optical reflectivity work at low temperatures has been done using one of two helium cooled continuous flow cryostats, one for simple experiments where the sample is mounted on a gold plated cold finger and capable of 4.2 K and the other for holding an optical pressure cell , attaining temperatures of down to 23 K and capable of measuring the pressure *in situ* (Figure 3.8). As the two cryostats are based on the same design, only the more complex will be discussed at length here. This one required much work by myself, both in the design and construction.

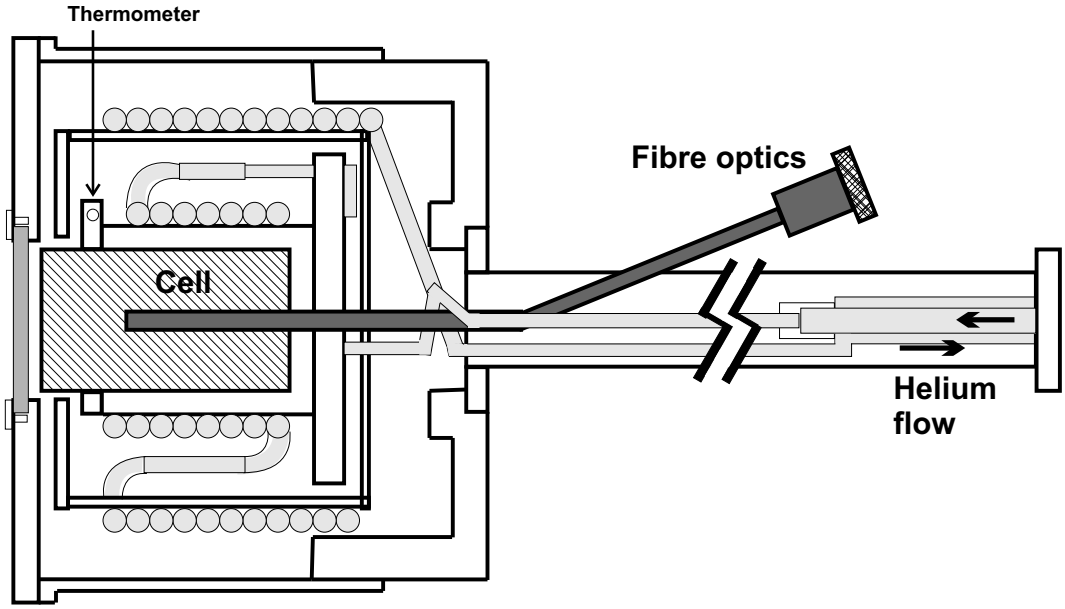

Figure 3.8: Diagram of pressure cell cryostat. Light grey marks the path of helium, dark grey marks the fibre optics

The large space required for the pressure cell (a cylinder of approximate dimensions 30 mm diameter and 60 mm length) inside the cryostat presented several design and operation challenges. The cell is made of steel and so is a relatively poor conductor of heat (compared to copper) and the sample is in the 1 cm of the cell that is not in direct

contact with the copper body of the cryostat. This gives a very slow response time for the system. In practice it was found that the cell only achieved the temperature of the rest of the cryostat about 30 minutes after the thermometer showed a stable temperature (this was determined by repeated measurement of the ruby pressure line (see next section of this chapter) as it is both pressure and temperature dependent. Once the ruby line stopped shifting at constant pressure the system was taken to be in steady state). To try to minimize the time lag, the thermometer was embedded in a copper ring that was clamped to the top of the cell and the main body of the cryostat. The diameter of the cell, the depth of the metal cone to the diamond with the sample and the angle required for, and focal length of, the reflecting objective of the microscope made it necessary to have a large front window (40 mm diameter) with a very low profile surround. It was found that a conventional clamping system for the KBr window, with bolts that are tightened in sequence, did not create completely even pressure and that this was enough to cause failure of the window on pumping. KBr, necessary for IR measurements, is very fragile compared to window materials such as quartz. A system was devised where the clamping ring was threaded on its outside and the whole thing screwed into the front plate of the cryostat (Figure 3.9). This was much more low profile than other, more traditional, designs and ensured even loading.

The fibre optic feedthrough consists of seven fibres in a bundle that runs from the back of the pressure cell anvil (there is about 5 mm of clearance between the two to allow for the decrease in length when the cell is tightened and any contraction upon cooling) and out through the fibre port where they are individually terminated. The central fibre goes to a 15 mW YAG laser to excite the ruby fluorescence line and the surrounding six to a Triplemate 1877e triple axis grating spectrometer to measure the position of this line (for safety and operation see Appendix B). The fibres take considerable time to make and polish so great care has to be taken if they need to be removed or reinserted (if for example joints need resoldering on the cryostat). To remove the fibres, the whole fibre terminator array can be unscrewed

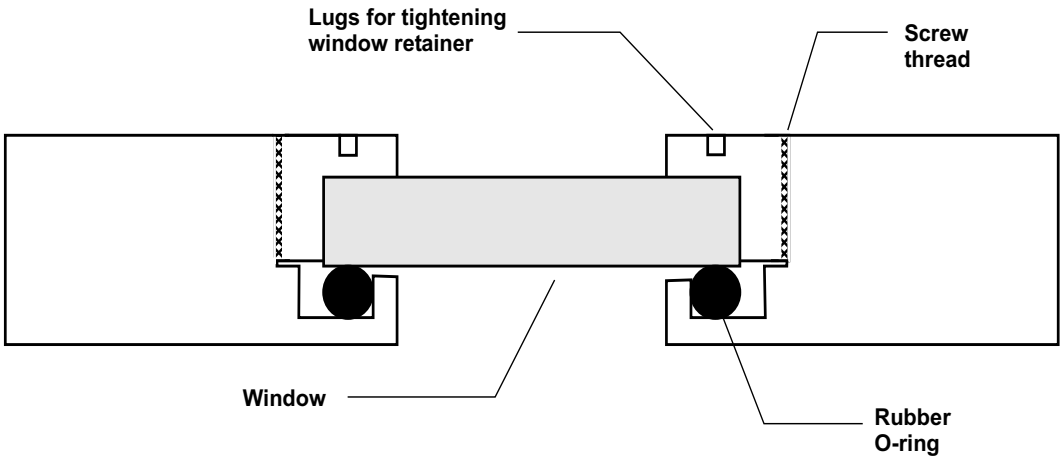

Figure 3.9: Schematic of the cryostat front window mount. A specially made tool fits into the lugs for tightening the window in place

and gently withdrawn. Putting them back is much harder. To aid this, the central copper column that feeds the fibres up through the inside of the cell is only glued in with low temperature glue so it can be easily removed. Then a narrow, tight-fitting rubber tube is fitted over the exposed ends of the fibres and threaded through the cyrostat. This can be used to pull while the other end is pushed to get them back in. Failure to do this results in the fibres catching on the inside of the feedthrough and the 6 cm stripped ends breaking.

During operation of the cryostat it is continuously pumped by a turbopump so a low pressure ($\approx 10^{-5}$ mbar) can be maintained despite very small, unavoidable leaks around the large o-ring seals. A turbopump is used to prevent any oil contamination of the optical surfaces. Temperature in the cryostat is controlled by an Oxford Instruments temperature controller. This provides manual control of the pumping rate and manual or automatic control of the heaters to attain a given temperature once the flow rate is set. The thermometer in the cryostat is Rhodium-Iron.

3.4 Pressure measurements

Pressure measurements have been carried out in the range of 0–20 kbar for both infrared and transport measurements using three different cells and pressure media, which will be discussed in the rest of this chapter.

3.4.1 Safety concerns

Pressure cell work presents some dangers to the operator which will briefly be discussed. There is a vast amount of energy stored in a loaded pressure cell, and as such it should be handled with extreme caution (for more details, see Appendix B) since it is possible for explosive failure to occur. Wearing safety glasses and good ear protection (in the case of large volumes of compressed gas) when handling such loaded cells is essential and any handling time should be kept to a minimum. The user should never point the end of a loaded cell at anyone or look down the end (even when wearing eye protection); the ends are where failure is most likely to occur. A method of shielding the user from the cell while it is not being handled is needed and this can range from small polycarbonate screens to large blast shields (in the case of gas pressure systems). Every pressure system will come with instructions and safety precautions and these should be studied before any use of the cell.

3.4.2 Diamond/Sapphire anvil clamp cell

Overview

The pressure cell was originally designed to run with two sapphire anvils. This was changed to one sapphire and one diamond to gain increased signal in the IR as sapphire has some absorption bands in the range we were interested in. In some of the final measurements, this was further changed to two diamonds due to chromium ions present in our sapphires obscuring the pressure reading. As the diamonds were much stronger they were able to be thinner for the same available pressure. This necessitated some additional spacers, but otherwise the cell was fundamentally unchanged.

See Figure B.1 for an exploded diagram of the parts. A copper gasket separates the anvils and the pressure medium is argon gas. The fluoresence line (excited by an argon laser) of small ruby chips in the cell is used to determine the pressure. It is loaded by cooling the cell with liquid nitrogen and then pumping argon through it. Pressure is changed using a press while the cell is at room temperature. The working pressure range is 20 kbar. Users should try to use the cell at pressures lower than this or its working life may be shortened. Full details of the operation of this cell can be found in appendix B. This cell is used in conjunction with the Bruker IFS 66v for measurements primarily in the mid-infrared (600–7000^{-1}) at either room temperature or in the cryostat discussed earlier.

Loading the sample

The small area available to mount the sample (Figure 3.11), the presence of a pressure medium (with non-unitary refractive index) and the fact that the anvils surfaces are highly reflective presents a number of challenges for mounting a sample and the subsequent pressure loading if we want useful results. The size means that all mounting work must be done using a binocular microscope and the sample surface must be of very high quality as there will not be much signal reaching the spectrometer in the best case (typical measurable sample area $<$ 0.2 mm^2).

Another major concern is that samples must be sufficiently flat so that they can be mounted on the back of the diamond window, such that there is no gap between them and the diamond. If the sample is not sufficiently flat, coloured interference fringes can be seen under a microscope and, more disastrously, in the measured spectra. Similarly, any specks of dust, traces of solvent residue or grease prevent good contact. As the sample is held to the diamond by electrostatic forces, any slight gap also greatly increases the chances of the sample falling off during pressure loading.

Latex gloves were worn while mounting the sample to prevent contamination of the surfaces with oils and all sample and diamond faces were carefully cleaned using ethanol and lens tissue (while some heavier, less volatile, organic solvents clean better,

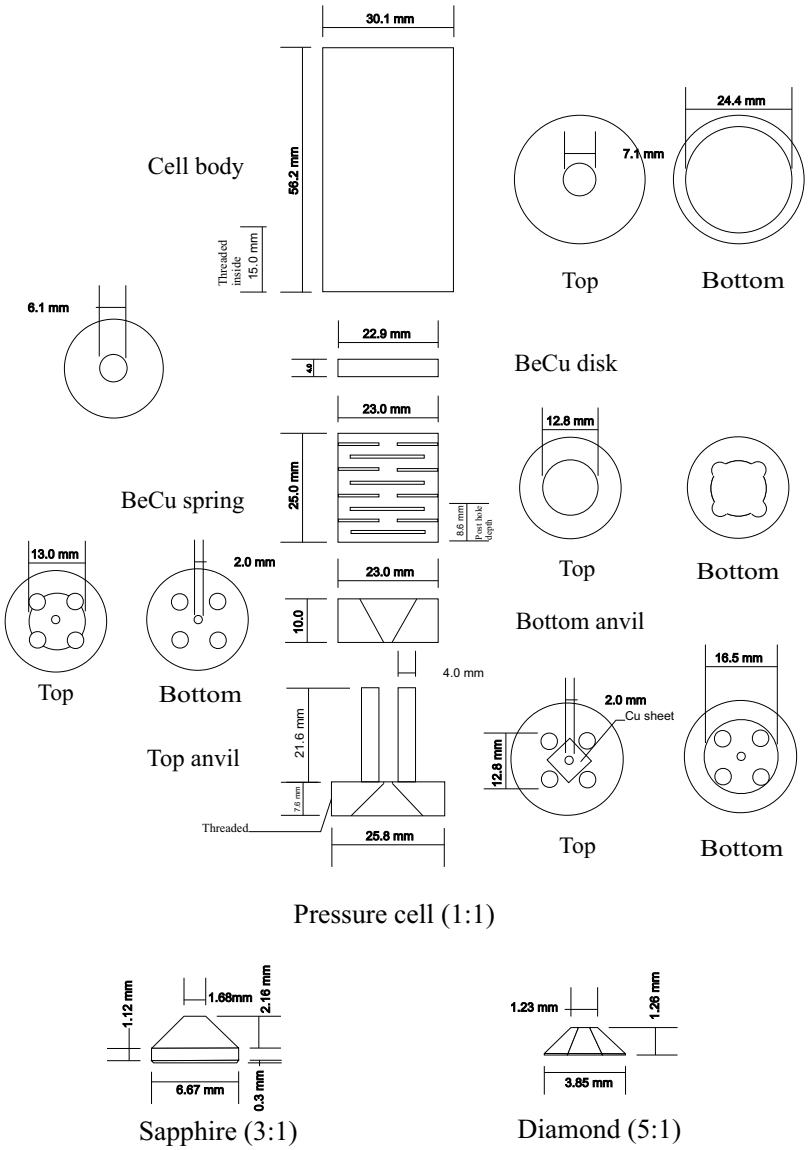

Figure 3.10: Exploded diagram of the anvil cell

it was found that the residues left behind were, in many cases, worse than the dirt). I personally found that a human eyebrow hair mounted in the end of a short wooden stick was ideal for handling the samples, but others have found great success with cat's whiskers (wait for them to fall out!) or tiny pieces of feather, though all need aggressively cleaning before use. Any cleaving of samples was done using a fresh razor blade on a clean glass slide.

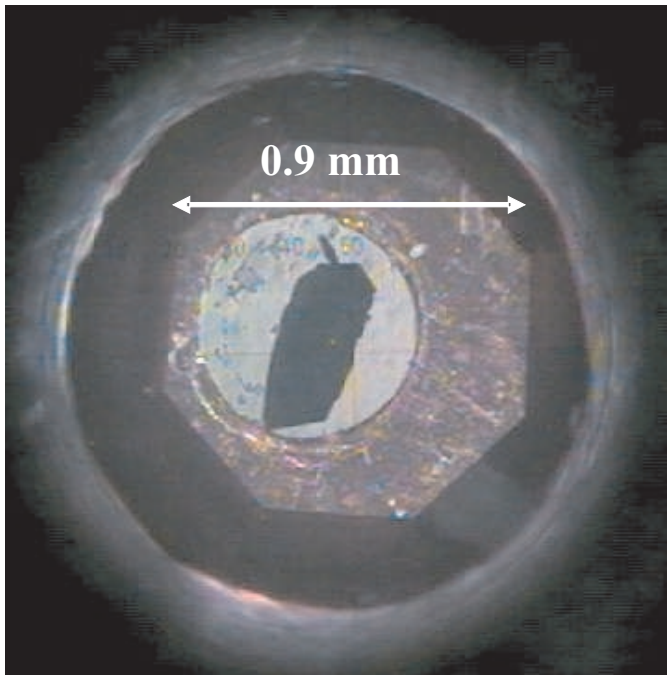

Figure 3.11: View into the loaded pressure cell. Note the octagonal imprint in the copper gasket caused by the diamond culate, the circular hole containing argon gas under pressure and the sample, in this case d_8-κ-BEDT-TTF$_2$Cu(SCN)$_2$

Measurement of the pressure

A small annealed ruby chip was placed into the cell along with the sample. The fluorescence lines R_1 and R_2 of ruby near to 700 nm has a well characterized pressure dependence [29]

$$P = \frac{1904}{B}\left[\left(1+\frac{\delta\lambda}{\lambda_0}\right)^B - 1\right] \tag{3.8}$$

where P is in GPa, λ_0 is the ambient pressure wavelength at room temperature and $\delta\lambda$ is the R_1 line wavelength shift in nm, B= 7.665 for hydrostatic conditions and B=5 for non-hydrostatic ones. However, things are not quite this simple as the wavelength also shifts with temperature [28], requiring an additional correction to the wavelength. This was found by cooling the pressure cell down while empty and measuring the ruby shift.

If T $<$ 80 K

$$\delta\lambda_T = +0.92\text{nm} \tag{3.9}$$

If T $\geq$ 80 K

$$\delta\lambda_T = -6.8581 * 10^{-3}\Delta T - 4.9137 * 10^{-3}\Delta T^2 + 3.3064 * 10^{-3}\Delta T^3 \mathrm{nm} \quad (3.10)$$

where ΔT is the difference between room temperature and the measured temperature.

This wavelength of this fluorescence line and a pair of neon calibration lines is measured using a SpectraTech Triplemate 1877e triple axis grating spectrometer (which is vastly more versatile than is needed for this task) and then a program written in Matlab was used get the pressure from these spectra and the temperature.

A major difficulty encountered with this pressure measurement was that many of the sapphires we used as anvils contained trace amounts Cr^{3+} (it is this that makes rubies red). This is not normally a problem as any fluorescence was very slight and undetectable in normal conditions. However, in this cell very small ruby chips need to be used to allow maximum amount of sample in the limited space. This means relatively long (several minutes) capture times were required. As the whole of the sapphire is illuminated the large volume meant that there was sufficient fluorescense from the sapphire anvil to alter the centre of the peak position enough to alter the pressure readings. This distortion was enough to cause the accidental destruction of several of the anvils due to overpressure while measurements showed the cell to be at no more than a few kbar. This is because the sapphire anvil is at a much lower average pressure than the small ruby chips due to larger cross-sectional area. Once this was discovered, a switch to two diamond anvils solved the problem.

Use of cell at low temperature and high pressure

This cell was also used in conjunction with the optical cryostat discussed earlier in this chapter. In principle, it still works in the same way, however a large number of additional things need to be considered.

Although temperatures down to 23 K are possible with this setup, reaching this base temperature from 50 K took several hours at extremely high ^{4}He flow rates, which

resulted in ice deposition all over the cryostat. The large window needed for infrared optics and the poor thermal conduction of the cell body prevented lower temperatures. In addition, at the lowest temperatures the pressure cell tended to leak. As 23 K is well outside the range of T_c, the critical temperature of the superconductor, of the materials studied, the experiments were performed between 300 K and 50 K.

The cell had previously only been used at room temperature and indeed was only designed for such use. This presented several challenges at low temperatures. Firstly argon gas is not ideal as a pressure medium. It is desirable to be able to measure below the boiling point of argon and any samples without "perfect" contact with the diamond surface tended to be "washed off" by the liquid. This severely limited the materials and samples which could be studied. Unless the whole surface of the sample was completely flat with no raised or overhanging ends it would lift off. The only way to ensure no lift off was to press quite firmly on the back of the sample. Initial work was performed with $TMTSF_2PF_6$, but the formation of slip dislocations [3] on the surface when pressure was exerted on the back made it unusable and the only measurements obtained were for ambient pressure (see Appendix A).

It was not possible to predict the pressure in the cell as it was cooled. On some measurements it would rapidly decrease, yet on others it would remain nearly constant. This is probably due to the fact that, at room temperature, the force of the spring in the cell is balanced by the pressure of the gas between the anvils. As the temperature is decreased, the pressure of the gas decreases so the anvils try to move closer together. If the gasket flows inwards under the increased pressure of the anvils this may result in the pressure dropping more slowly than would be expected. If the gasket does not flow as easily (or flows outwards), other components of the cell contract or the cell leaks slightly we see a much more rapid pressure drop. However, in general, the pressure at room temperature was much greater than that at 50 K, limiting the maximum pressure at low temperature.

The maximum possible size of hole in the gasket is a circle of 0.5 mm diameter, and this obviously limits the maximum size of sample which can be studied. In practice, this

turned out to be an area of about 0.25 x 0.25 mm^2. Although larger samples would fit initially, movement and/or shrinking of the hole on cooling or pressure increase would crush them or, at the least, dislodge them from the surface of the diamond. This small sample size, combined with the highly reflective diamond anvil and the 3 mm thick KBr window on the cryostat (the thickness was necessary due to the width of the window, 40 mm, needed to cover the entire front of the cell) resulted in quite a small reflected signal. While this signal was within the capabilities of the apparatus to measure, it did result in a lower signal to noise ratio than other measurements undertaken using the Bruker IFS 66v. This noise is due to detector dark noise and backscatter from the apparatus and was up to 25% of the total measured signal in the most difficult measurements– in non-pressure cell experiments this would normally be less than 5% of the total.

Measurements were performed purely in the mid-infrared (700 cm^{-1}–6000 cm^{-1}) as the modifications to the interferometer necessary to measure small samples in such a cell made changing ranges, and the subsequent re-alignment, take at least a day. As the pressure was not the same for repeated coolings, the joining of such spectra would be impossible. In addition, far-infrared measurements are not practical as all available window materials do not transmit visible wavelengths. Contraction of various parts of the cell on cooling and small shifts in position caused by the helium transfer line resulted in a small shift in position and focal plane of the sample for each temperature-pressure point. This can be corrected for in the mid-infrared or near-infrared, but the slow response time of FIR detectors, the highly reflective nature of other parts of the cell (the copper gasket and diamond surface) and an inability to check this position visually made such measurements very unreliable.

Measurement of a background or reference spectra

Normally, the reference spectrum is taken as the reflectance of a flat evaporated gold mirror. This works because gold is a nearly perfect reflector in the infrared. However things become more complex inside a pressure cell. Diamond absorbs in a narrow band

in the infrared (see Figure 3.12) due to impurities. The diamonds used had low levels of impurities (nitrogen), but these were enough to cause relatively strong absorption in a region between 1700 cm^{-1} and 2700 cm^{-1}. It was essential that this false feature be removed before the spectra could be analyzed, and the first step was to acquire a good reference spectrum.

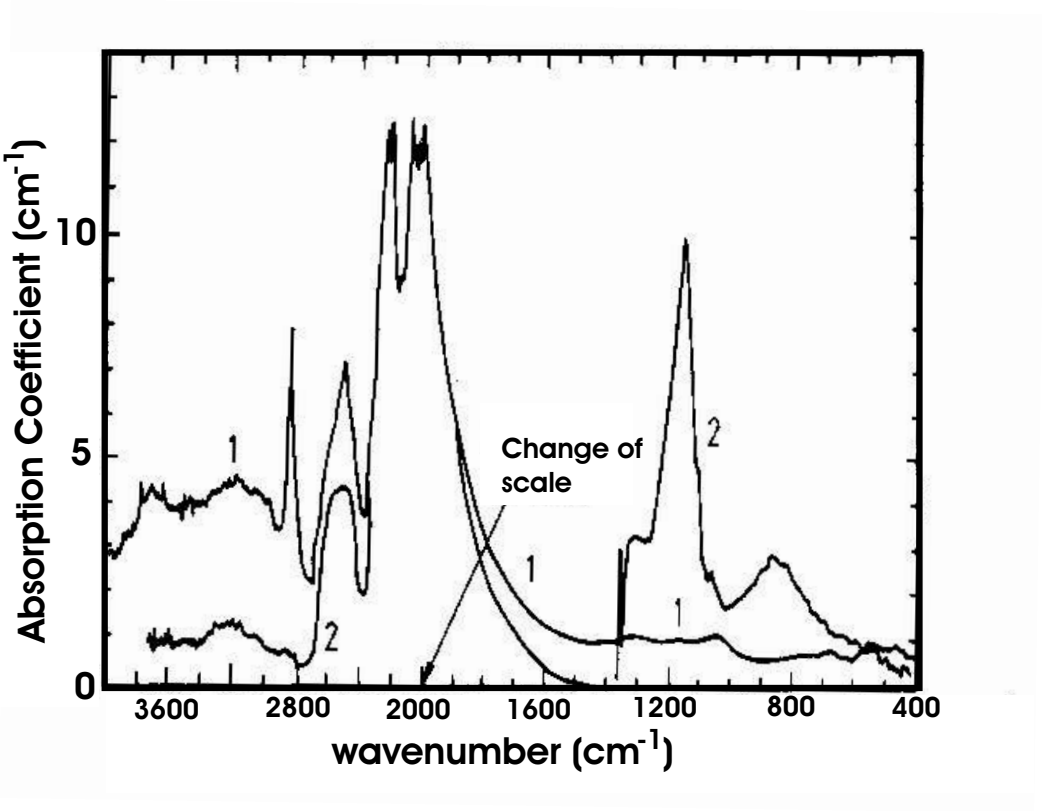

Figure 3.12: Infrared absorption spectra of diamond where in 1 the main impurities are boron atoms and in 2 the main impurities are nitrogen atoms. Figure from [32]

There are several ways background measurements for the spectra can be performed with these sort of samples. One of the most accurate techniques, in terms of absolute reflectivity, is the evaporation of gold onto the sample surface and then repeating the measurement. This was impractical as the same exact pressure cannot be achieved twice. Another possible technique would involve using a external gold mirror for the background as would be done in the non-pressure cell case. Unfortunately this leaves the diamond absorption in the spectrum which is highly undesirable. A mirror cannot be mounted inside the cell as there is not enough space for this as well as a sample.

A potential solution to this was to evaporate gold onto the gasket itself, turning it into the mirror. Although this initially appeared very promising it was found that the exact absorption due to the diamond was highly sensitive to the exact beampath. It is believed that this is due to the reflecting objective of the microscope. This has a very short focal length and a very wide focal angle when compared to a lens and this means part of the beam "clips" the edge of the diamond and is internally reflected if an area near the edge of the diamond culate is measured.

The solution to the problem turned out to be a several stage process. First the sample is measured as normal, R_s (see Figure 3.13a), along with a measurement of the bottom surface of the diamond next to the sample. This enabled the spectrum to be quickly checked to make sure that nothing obvious had gone wrong. Then a further measurement of the top surface of the diamond directly above the sample, R_{td1}, was taken. This allows any short term fluctuations such as those from water noise to be removed. There is a band of water vapour absorption lines centered at about 2200 cm^{-1} and the exact strength of the absorption depends on the concentration of water vapour at a given time. As this will change by the hour, an immediate reference measurement is needed.

After the the whole experiment had been finished the sample was removed and its position on the diamond surface carefully noted. The cell was then cooled down with nothing in and a measurement of the bottom diamond surface where the sample had been, R_{bd} (see Figure 3.13b), and the top diamond again, R_{td2}, was taken. This allows the exact path of the beam through the diamond to be matched, and absorption to be removed

$$R_{clean} = \frac{R_S/R_{td1}}{R_{bd}/R_{td2}} \tag{3.11}$$

Where R_{clean} is the reflectance of the sample with the absorption removed. This works because R_{td1} and R_{td2} only differ by any minor short term fluctuations in the signal which cancel out in R_S and R_{bd} respectively. There is an additional correction factor, A_D, as diamond is not a perfect mirror in the infrared. From the refractive index of diamond, which is virtually constant in the infrared (outside absorption) at a value of

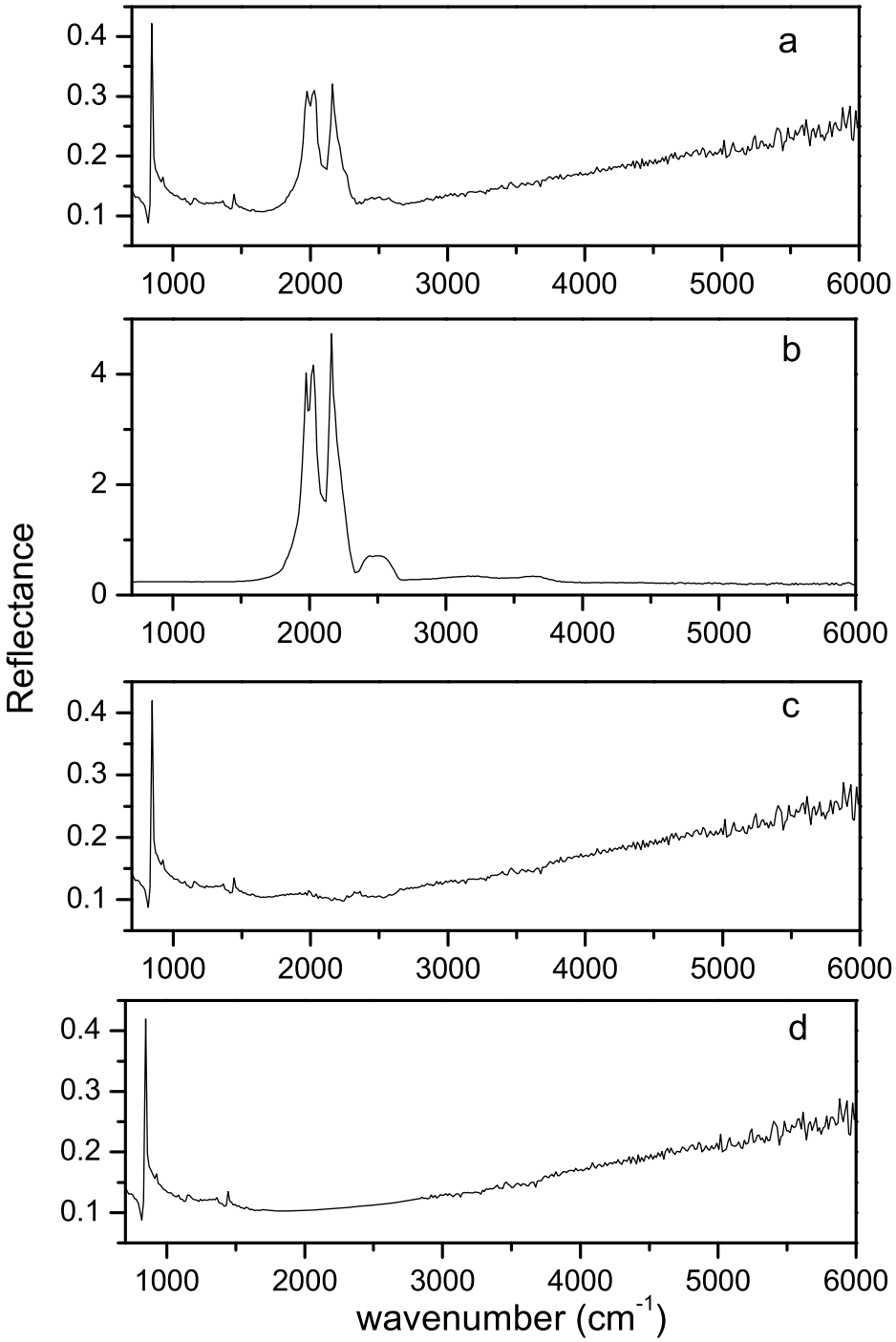

Figure 3.13: a) Spectrum measured under diamond. b) diamond absorption. c) spectrum with diamond absorption removed. d) spectrum with absorption removed and polynomial fit through region. Sample: $(TMTSF)_2PF_6$

2.39 [28], we find that 17% of the light is reflected at an air-diamond interface giving us an A_D of 0.17. So the corrected reflectance, R, is

$$R = R_{clean} A_D \tag{3.12}$$

This resulting spectrum has virtually all the diamond absorption removed (see Figure 3.13c). However, not all removals of the absorption work as well as this one and, in cases where the spectrum is fitted using oscillators, the fitting program attempted to fit the small "bumps" so a low order polynomial was fitted through this region. This is acceptable if the underlying shape is preserved and there are no small features of interest in this range (see Figure 3.13d).

3.4.3 Piston cylinder cell

This cell is made of a non-magnetic steel and is designed to allow magnetoresistance measurements to be carried out at low temperature and high magnetic field at pressures of up to 20 kbar (see Figure 3.14). In this work, a large volume ^{3}He cryostat and an Oxford instruments superconducting magnet were combined to give temperatures down to 700 mK and fields of up to 17 T. The sample is mounted using gold wires stuck to the surface with graphite paste and these gold wires were soldered to the copper wires that feed into the cell through a stycast resin plug. Ideally the sample surface to be measured is exactly perpendicular to the magnetic field, although the confined nature of the space and the inherent "springiness" of the copper feedthrough wires made this very difficult. Hence any misalignment was corrected for by comparison with ambient pressure data.

The pressure medium used was Fluorinert FC75. This is a hydrocarbon analogue in which fluorine has been fully substituted for hydrogen. It is a thermally and chemically stable liquid at room temperature with a high dielectric strength (> 13000 Volts/mm) and good heat transfer properties [30], making it a good choice for low temperature, high pressure measurements in most cases.

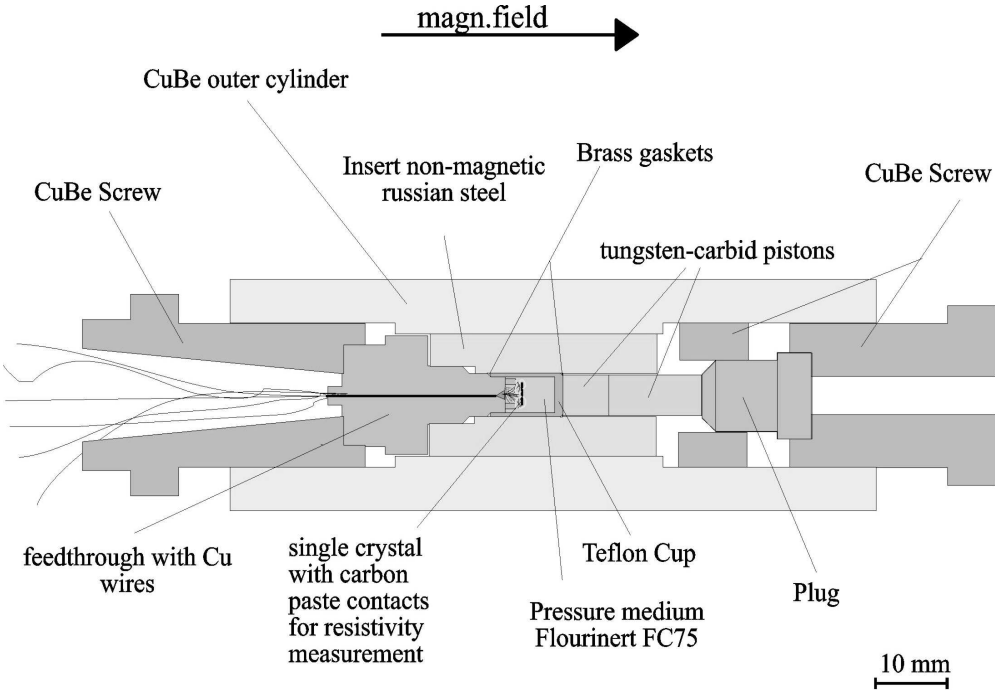

Figure 3.14: Diagram of piston cylinder cell for use in transport measurements. Figure from [28]

Pressure was applied to the cell using a hydraulic press (the same as used for the diamond anvil pressure cell; see earlier in this chapter and Appendix A). This force is transferred to the sample through the liquid enclosed in a Teflon cap by the piston and the outer body of the cell is screwed down to hold the new pressure. This pressure was measured using a small coil of manganin wire with a known pressure and temperature coefficient [28] mounted just underneath the sample.

The cell was cooled from room temperature to 4.2 K over a period of approximately 12 hours to reduce the risk of introducing shear stresses to the sample as the media freezes. Temperatures were measured with a Pt thermometer above 50 K and a ruthenium oxide thermometer at low temperatures. The actual temperature of the field sweeps was taken to be the average of the temperatures before and after, as the resistance of the thermometer is altered by magnetic field.

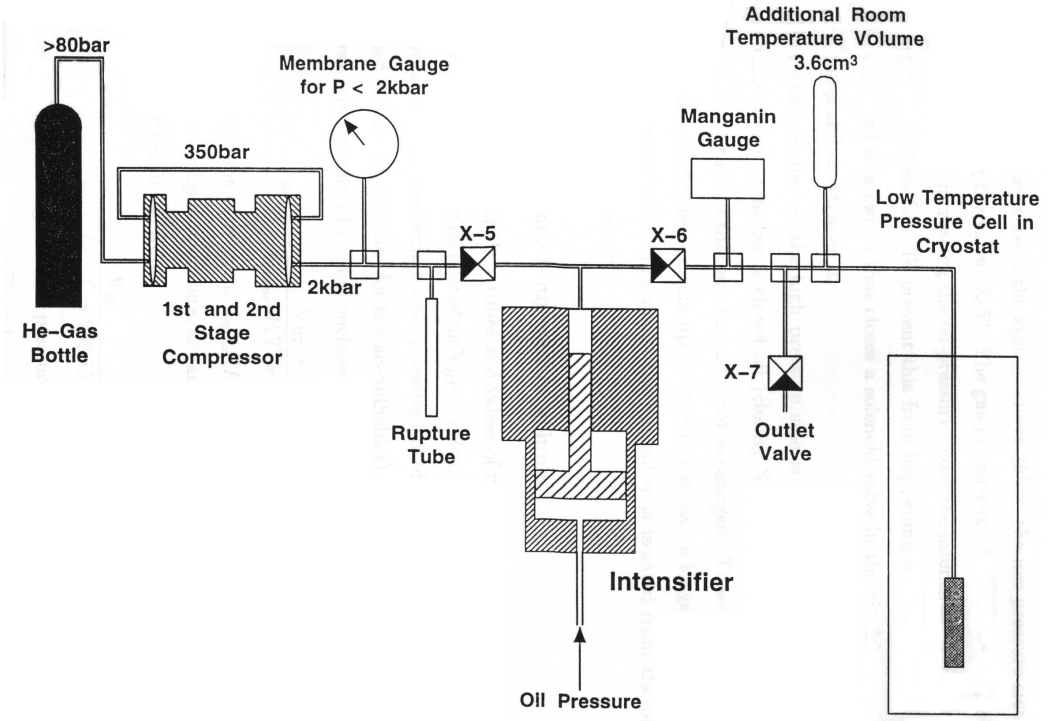

Figure 3.15: A sketch of the ^{4}He gas pressure system (from [33])

3.4.4 ^{4}He gas pressure system

This pressure cell was made by Unipress and is attached to a Harwood Engineering compressor system using helium as the pressure medium (see Figure 3.15). The helium gas from a gas bottle is first run through a two stage compressor and then into a reservoir which is compressed by a large hydraulic ram, enabling pressures of up to 14 kbar to be achieved. This reservoir, which is maintained at room temperature, is permanently attached to the cell by a Cu-Be capillary. This reduces any decrease in pressure in the cell while cooling down. Unfortunately this also presents the greatest risk to the operator as the capillary is $\sim$2 m long, very fragile and containing gas at very high pressure. Large shields need to be used to protect the user from high velocity shrapnel if the capillary were to fail (calculations suggest that this could be of similar energy to a small bullet). Having said that, the versatility of this system more than made up for the drawbacks. The pressure inside the cell is measured using a manganin wire gauge [28].

The cell is large enough, and can have enough wires in the feedthrough, to measure two small samples at the same time. The obvious advantage of this is that it allows direct comparison between two different materials under exactly the same conditions. The electrical contacts to the samples themselves were made using fine platinum wire and graphite paste. The other end of the wire was then soldered to the copper wires from the feedthrough. Any misalignment was allowed for by comparison with ambient pressure measurements.

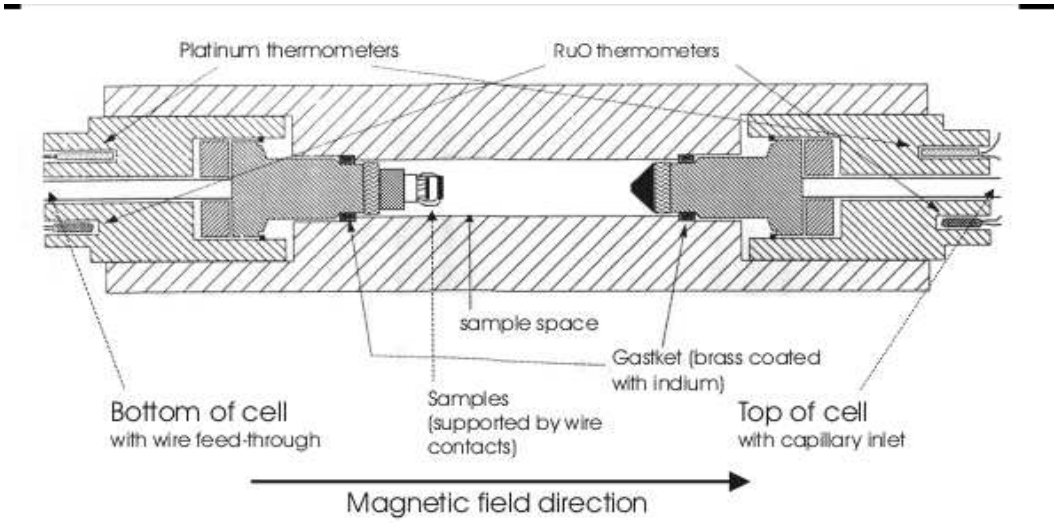

Figure 3.16: A diagram of a Unipress cell for ^{4}He gas pressure measurements. The cell is mounted vertically in the cryostat (from [33])

The cell is mounted in a variable temperature insert in a cryostat with an Oxford Instruments superconducting magnet, allowing samples to be studied in fields of up to 15 T and temperatures down to 1.5 K. The temperatue of the system was measured using a ruthenium oxide sensor for low temperatures (< 40 K) and a platinum resistor for higher temperatures, thermally anchored to the top of the cell. Temperature control is achieved using the variable temperature insert and two heaters mounted on the cell body.

Great care needs to be taken when cooling the system to low temperatures as the high pressures mean that the helium pressure medium freezes at temperatures of up to 60 K [28]. To prevent non-hydrostatic conditions in the cell and the capillary blocking with a helium plug, the sample is cooled very slowly from 10 K above to 10 K below

the transition ($\sim$0.1 K/min). This was achieved by using the variable temperature insert to cool the cell while, at the same time, using the top heater to ensure that the top of the cell was at a higher temperature than the bottom, reducing strain in the sample [31]. This heater needed to be controlled by hand as temperature controllers were found to have difficulty moving smoothly through the gas-solid transition.

Below the freezing point of ^{4}He, the pressure on the sample was determined using experimentally determined temperature-pressure data for solid helium [34]. The pressure loss along an isochore from the melting temperature to 0 K is smaller for helium than any other solid because the zero-point vibrations give rise to most of the internal pressure, again making it a good choice for this type of pressure work.

To change the pressure in the system, it is necessary to warm the cell to well above the phase transition. Failure to do this could result in changing the pressure in the capillary and reservior but not in the cell, as it is still frozen. This would result in highly non-hydrostatic conditions due to the much larger pressure at one end of the cell. In practice that meant warming to 100 K for the pressures used.

Chapter 4

Magnetoresistance Measurements on $d_8 - \kappa$-$(ET)_2Cu(SCN)_2$

4.1 Overview

The nature of superconductivity in organic superconductors is much debated in the literature [1]. The close proximity of an antiferromagnetic to a superconducting ground state in the temperature-pressure phase diagram means this phase diagram bears a remarkable similarity to the phase diagram of cuprate superconductors (see Figures 4.1 and 4.2).

This has led to suggestions that similar mechanisms may be governing superconductivity [37]. In the cuprate superconductors, the properties can be altered by changing the carrier concentration [38] or the pressure. However, in organic superconductors, such changes have only been linked to the pressure so far, as it is very difficult to change the carrier density. It is not possible to vary the number of charge carriers in a similar way to the cuprate superconductors because any added dopants destroy the crystal structure and hence the properties we are interested in. In addition, in charge transfer salts, the charge carriers are provided by the organic donor molecules and these typically donate $1/2$ or 1 electron each– far less variation than the continuous variation available from doping cuprates. A further drawback is that these

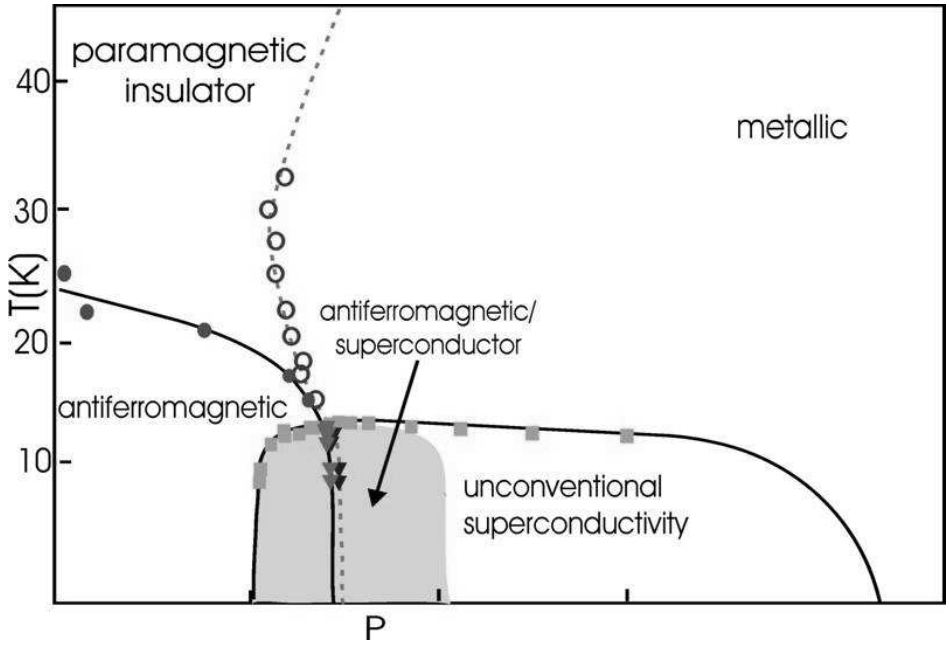

Figure 4.1: Typical temperature-pressure phase diagram for an organic superconductor (after [35])

changes require, at the least, a change of inorganic cation meaning that you are not even measuring the same compound. A method of linking the changes in pressure to changes in carrier concentration would be very useful in furthering these comparisons and this will be investigated in this chapter.

κ-$(ET)_2Cu(SCN)_2$ is an interesting material to study in this context as it is a typical quasi-two-dimensional organic superconductor. Its highly anisotropic nature is reflected in its Fermi surface, which features both closed and open sections and can be studied through Shubnikov-de Haas oscillations. The closed section, or α-orbit, gives rise to oscillations at $\sim$600 T at ambient pressure (see Figure 4.3). However, at higher fields and low temperatures we observe magnetic breakdown. Magnetic breakdown is due to electrons tunnelling between states of equal energy in adjacent sections of the Fermi surface when the cyclotron energy is of the order of the splitting between the associated bands. This can be seen as a larger k-space orbit, called the β-orbit (see Figure 4.3). The orbit encompasses parts of both the quasi-two and quasi-one dimensional sections of the Fermi surface [44]. As this orbit has the same cross

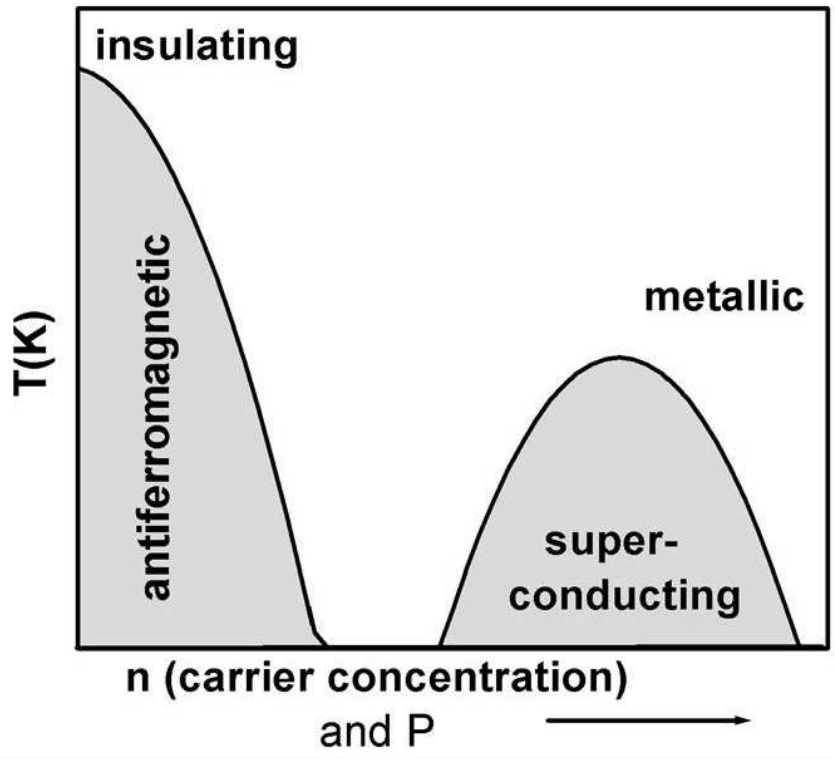

Figure 4.2: Typical phase diagram for a cuprate superconductor. Increased doping leads to higher carrier concentration and this is the normal method for achieving different values of n. However pressure also changes n, but to a lesser extent (after [36])

sectional area at the Brillouin zone, the change in this frequency with pressure gives us a measure of the low-temperature compressibility of the material. When combined with the α-orbit it also enables the exact shape of the quasi-two-dimensional Fermi surface to be calculated from the effective dimer model [39].

κ-(ET)$_2$Cu(SCN)$_2$ also displays a "negative isotope effect" when the terminal hydrogen atoms are removed and replaced with deuterium, i.e. the superconducting critical temperature, T_c, goes up [40][41]. Substituting all other atoms with heavier isotopes produces a very small normal or no isotope effect [41]. A deuterated sample was chosen to further investigate this effect. Initially, measurements using Fluorinert as a pressure medium pointed to a more rapid suppression of T_c with pressure, suggesting that the superconductivity mechanism is very strongly influenced by small changes in the Fermi surface [42]. However, ac-susceptibility measurements using helium as a

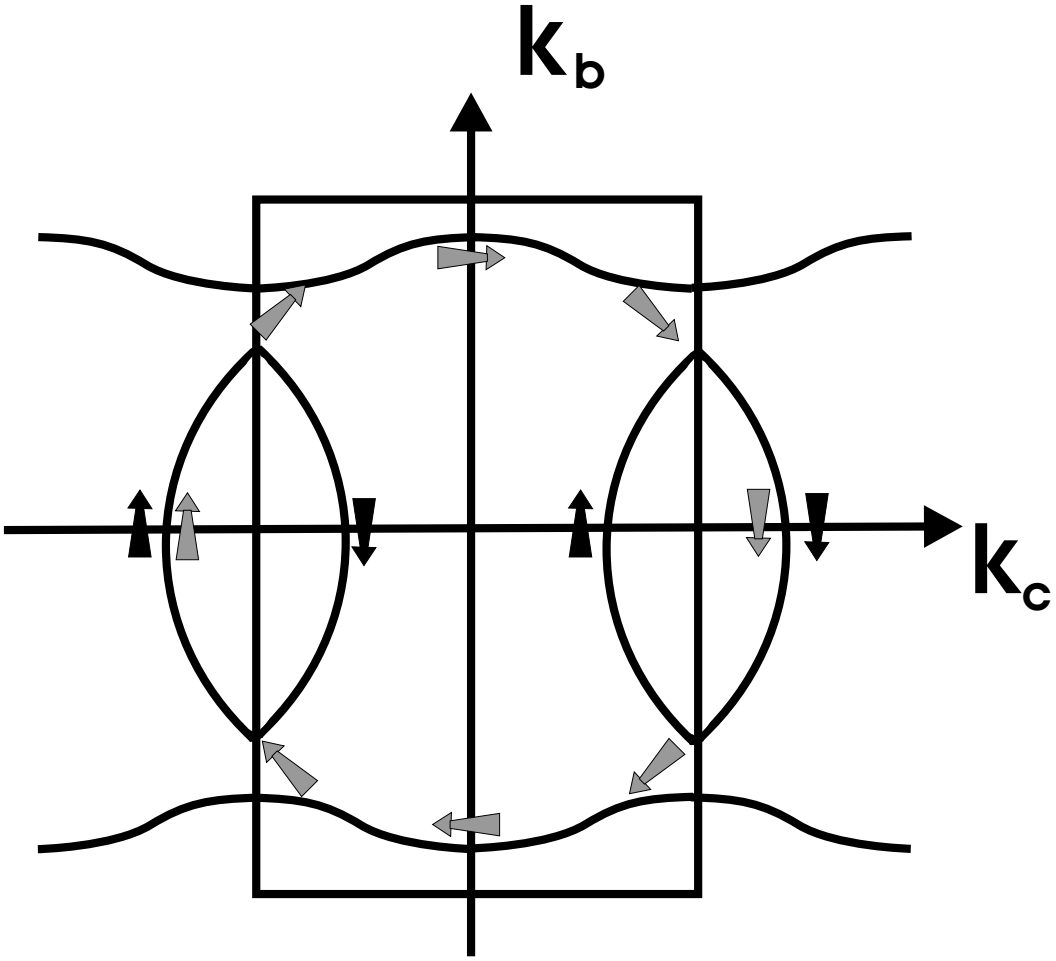

Figure 4.3: the Fermi surface of d_8-κ-$(ET)_2Cu(SCN)_2$. The black arrows denote the α-orbit and the grey arrows the β-orbit (based on [44])

pressure medium [43] have shown that the difference seen in the deuterated sample in [42] is not due to isotope composition. To further clarify matters, the magnetoresistance measurements described in this chapter were performed using helium gas as a pressure medium on both the normal and deuterated compounds. These results can be compared and contrasted with my measurements using Fluorinert and earlier measurements by Caulfield *et. al.* using petroleum spirit [45]. This comparison shows that the properties of this material at a given pressure will depend on the pressure medium itself, i.e. the experimentally determined value of the pressure and measurements at that pressure cannot be compared to those of a different experiment unless the

same pressure medium is used. From now on, we shall refer to properties which can be compared in experiments using different pressure media, such as temperature, as *transferable parameters* and those which cannot, such as pressure, as *non-transferable parameters*. The comparison will also allows us to relate the pressure induced change in carrier concentration to T_c.

4.2 The experiment

Two separate sets of experiments were performed, one using a liquid loaded cell with Fluorinert as a pressure medium, and the other a gas loaded cell using helium as the pressure medium. The first will be discussed and then any differences for the second set will be mentioned.

The first set of experiments was performed using the piston cylinder cell with Fluorinert FC 75 as the pressure medium.

The samples used were single crystals of κ-$(ET)_2Cu(SCN)_2$ in which the end hydrogens had been isotopically substituted by deuterium. They were approximately 0.7 x 0.5 x 0.1 mm^3 in size. In order to check for extrinsic effects, two samples, made in different labs (Strasbourg and Sendai), were used. No systematic differences were observed so both sets of results have been combined.

The magnetoresistance of the samples was measured using standard four-wire AC techniques (frequency f = 15–180 Hz, current I = 1–20 μA) [1]. A lock-in amplifier was used for voltage detection as this allows good signal to noise ratio for a much lower current, reducing the chance of heating the sample. Contacts were glued to the upper and lower surfaces and the voltage was measured in the interlayer direction. This is because the interplane resistance is several orders of magnitude bigger than the intraplane and so is easier to measure and the irregular shape of the crystals mean that any intraplane measurements will contain all components of the resistivity tensor whereas interplane measurements will contain only ρ_{zz} [1].

The ^{4}He cryostat enabled temperatures down to 1.5 K to be achieved, though a

^{3}He insert was required to reach down to 0.7 K. The limited amount of ^{3}He and the limited amount of space available to condense it into meant that only one, or for higher temperatures two, field sweeps could be made per"shot" of ^{3}He. This scarcity of ^{3}He made controlling the temperature with the pumping valve quite challenging and the fact that the thermometer did not read accurately at high field combined to increase the error in the measured temperature and gave a higher minimum temperature. A range of pressures up to 11.5 kbar was measured.

For the helium gas pressure measurements, a Harwood Engineering compressor was attached to a cell made by Unipress. Pressures up to 7 KBar were measured. Both the normal and deuterated samples were grown by the same laboratory (Argonne). The normal sample was approximately 1.2 x 0.4 x 0.1 mm^3 and the deuterated sample was approximately 1.0 x 0.7 x 0.2 mm^3. The deuterated sample was found to be aligned with its out of plane axis $\sim$21° to the magnetic field by comparison with ambient pressure data [1] and corrections were made accordingly. The protonated sample was misaligned by $\sim 18^\circ$ and corrected for in a similar manner.

Temperatures down to 1.5 K and fields of up to 15 T were used for the experiment.

4.3 Analyzing the data

Shubnikov-de Haas measurements allow us to study the areas of the various Fermi surface pockets (see Figure 4.3). The small, closed loops, or α-orbits, are easily measured but the magnetic breakdown orbit, called the β-orbit (see Figure 4.3) is only seen at higher fields (> 14 T).

Typical data from the first set of experiments can be seen in Figures 4.4 and 4.5. As both experiments are Shubnikov-de Haas experiments, the results are qualitatively the same and so the method of analysis is the same. It can be easily seen that even comparatively low pressures start to suppress the superconductivity. The traces are only up to 15 T because the superconducting magnet needed to be below 2.2 K to sustain higher fields and previous studies have shown that the amplitude of the

oscillations is strongly attenuated at higher temperatures as well [45]. As a result of this, the higher field regions were only measured at lower temperatures. A blown-up section of a 12 T–17 T trace at low temperature can be seen in Figure 4.6, where the oscillations are clearly visible. At the lower fields, we see primarily a single frequency, due to the α-orbit, but as the field increases, additional components arise due to magnetic breakdown orbits.

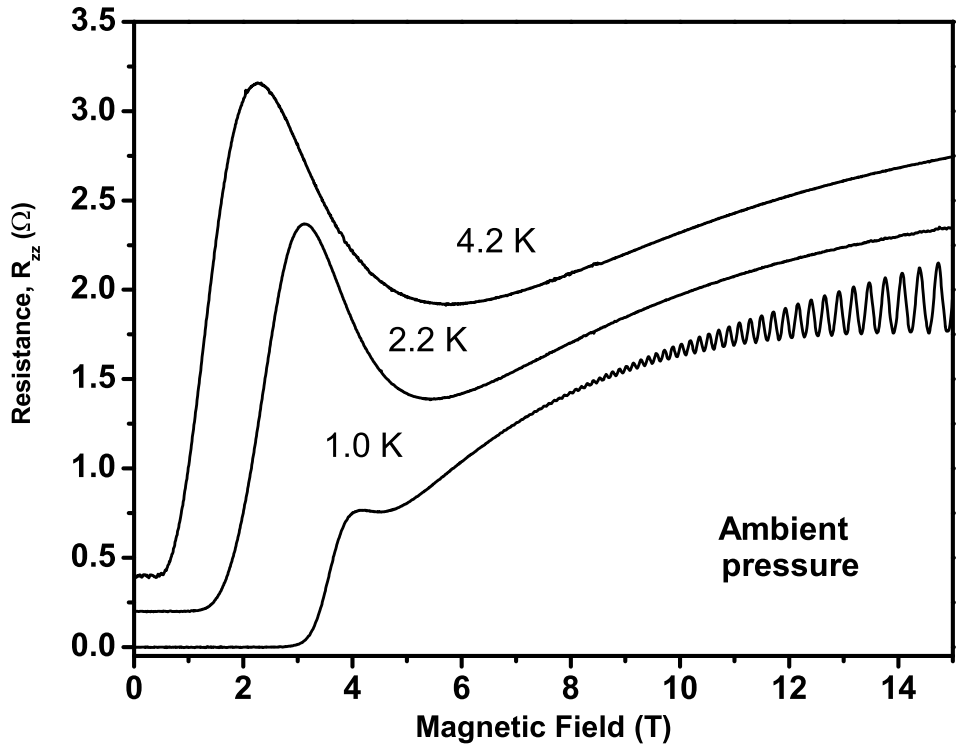

Figure 4.4: A selection of magnetoresistance data for d_8-κ-$(ET)_2Cu(SCN)_2$ at ambient pressure. The spectra have been offset for clarity

The exact oscillation frequencies were extracted using a fast Fourier transform of the data. However, first one needs to remove the background magnetoresistance, as this is a strong function of field. For a quasiparticle, the probability of scattering is proportional to the number of states it can scatter into. This probability is oscillatory as the density of states at the Fermi energy, $g(E_F)$, is itself an oscillatory function [20].

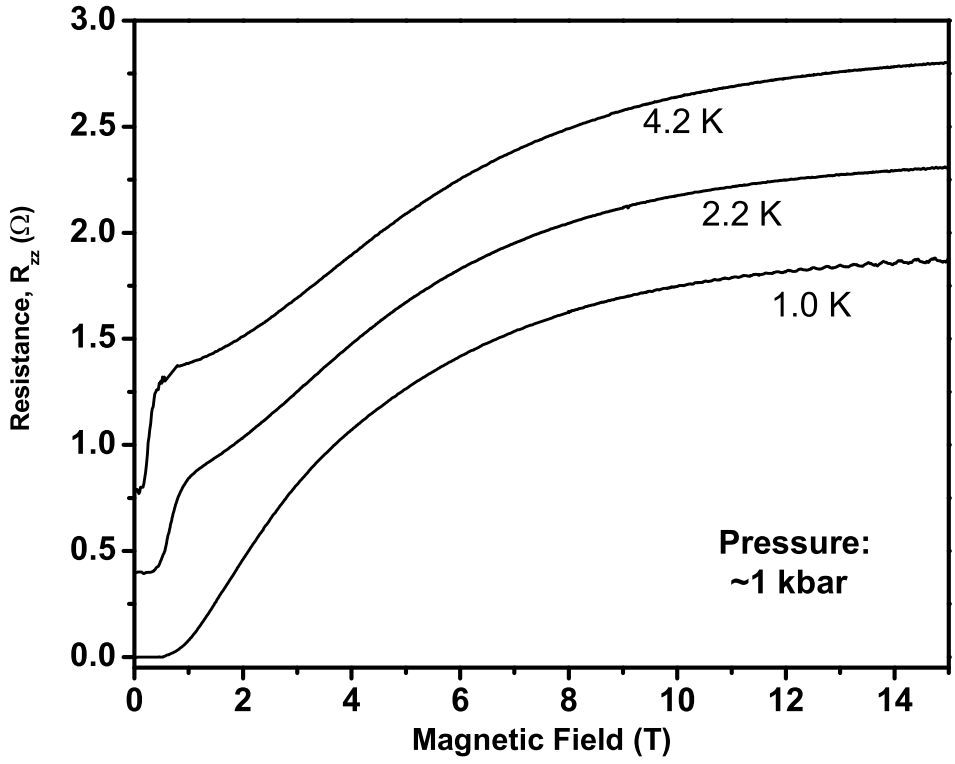

Figure 4.5: A selection of magnetoresistance data for d_8-κ-$(ET)_2Cu(SCN)_2$ at 1 kbar with Fluorinert as a pressure medium. The spectra have been offset for clarity

This results in the resistivity and quasiparticle relaxation time, τ, also being oscillatory. If we consider the simple case of a single Fermi surface pocket we would expect [1]

$$\frac{\rho_{osc}}{\rho} \sim R_T \frac{g_{osc}(E_F)}{g_0(E_F)} \tag{4.1}$$

where ρ_{osc} and ρ are the oscillatory and background resistivities respectively, R_T is the temperature reduction factor (defined in equation 2.53, Chapter 2) and $g_{osc}(E_F)$ and $g_0(E_F)$ are the oscillatory and non-oscillatory components of the density of states [20]. As, from this equation, the background resistivity acts to normalize the amplitude of the SdH oscillations, division by a polynomial fitted to the data is the best way to remove background magnetoresistance [1]. Although this material is more complex

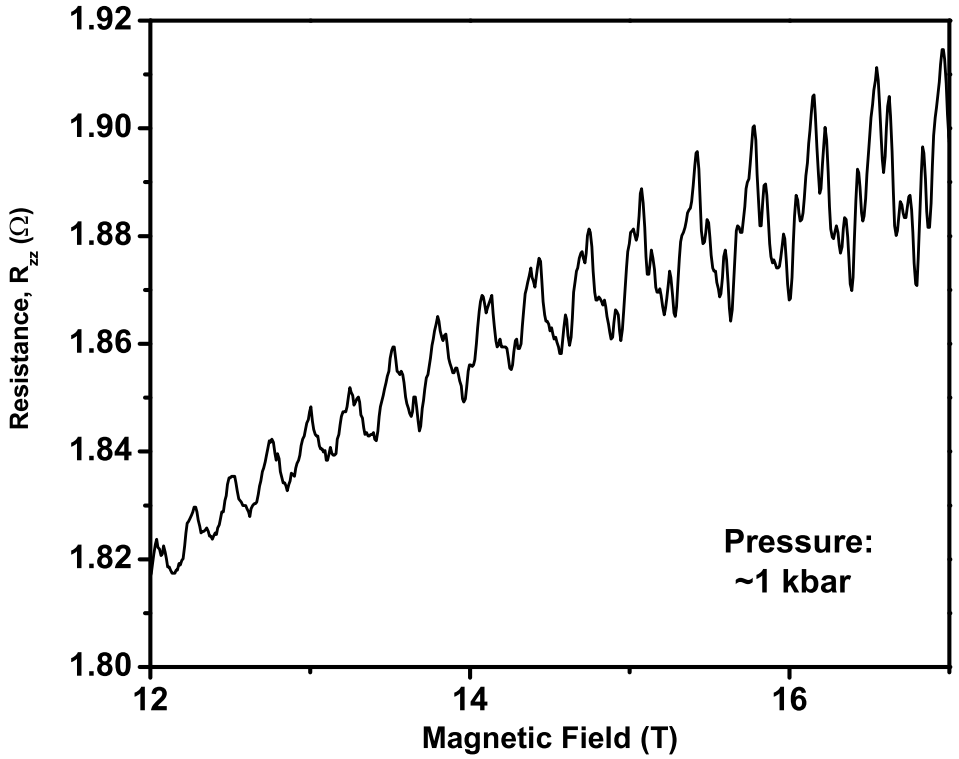

Figure 4.6: A section of magnetoresistance data for d_8-κ-$(ET)_2Cu(SCN)_2$ at 1 kbar and 1.0 K with Fluorinert as a pressure medium. At lower fields the oscillations are relatively smooth, however additional components can be seen as 17 T is approached. This is caused by additional frequencies being present due to magnetic breakdown and possibly the pinning of the chemical potential to very sharply defined Landau levels [1].

than this simple case, it has sufficient similarities so that this is still the preferred method [1].

A fast Fourier transform of the oscillatory component gives the α, β, $\alpha - \beta$ and $2\alpha - \beta$ frequencies. A representative trace can be seen in Figure 4.7.

The α-frequency has by far the strongest peak but the β-frequency is also present. The peak at low frequency is due to low frequency noise from a range of sources, including imperfect fitting of the polynomial. What is initially more surprising is the frequencies of the form $F_\beta - nF_\alpha$. These frequencies cannot be understood classically as they appear to represent non-physical situations. However, these frequencies are

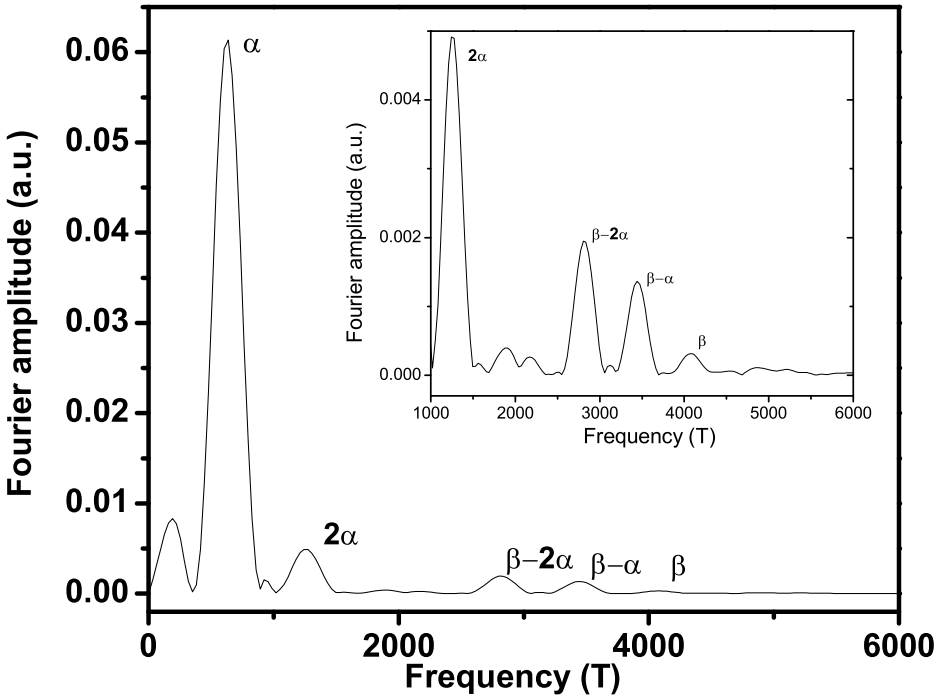

Figure 4.7: A fast fourier transform of the 15 T–17 T magnetoresistance data for d_8-κ-$(ET)_2Cu(SCN)_2$ at ambient pressure and 0.7 K. The insert shows a blown up part of the main figure as the large relative intensity of the α-peak makes discerning the lower intensity peaks extremely difficult. Peaks of note are the α-peak, at around 600 T, and the β-peak, at approximately 4000 T. It is possible that the peaks of the form $\beta - n\alpha$ are due to pinning of the chemical potential at sharply defined Landau levels.

not thought to be due to Stark quantum interference as the $F_\beta - F_\alpha$ frequency has been observed in de Haas-van Alphen experiments [1]. As Stark quantum interference is due to interference between different possible paths and not due to orbits about closed sections of the Fermi surface it will not affect the free energy and hence the magnetization [1]. A possible explanation could be pinning of the chemical potential to very sharply defined Landau levels. This causes the allowed orbits to pass through the chemical potential more slowly resulting in a downward shift in frequencies of an amount close to the α-orbit frequency [46]. These frequencies are much stronger than observed in similar experiments performed on an undeuterated sample [45].

4.4 Results

4.4.1 Direct pressure comparisons across media

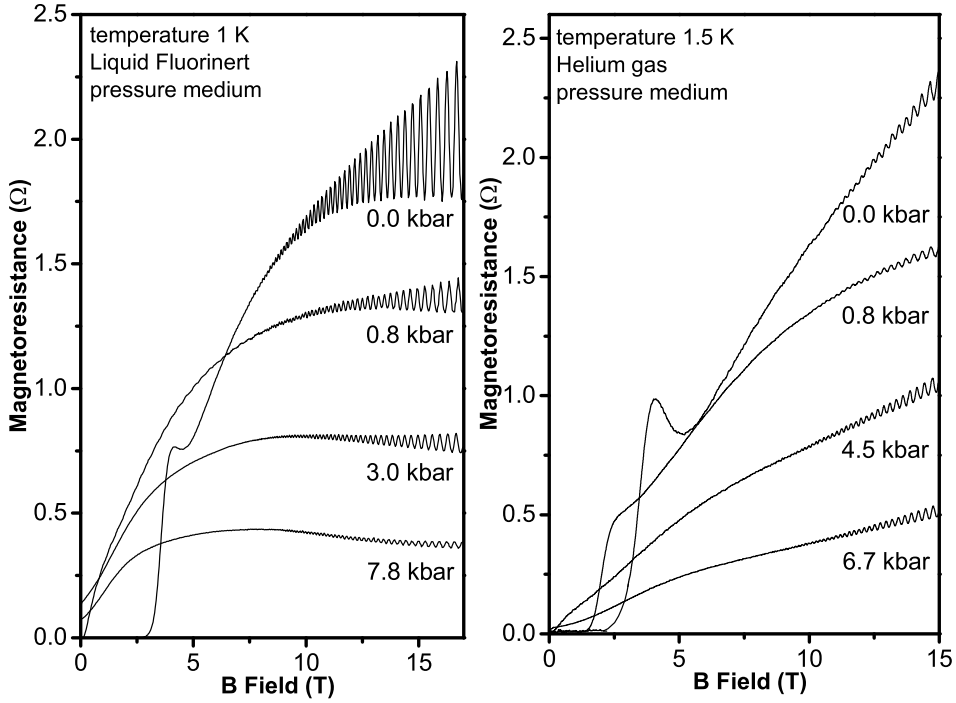

Figure 4.8: Magnetoresistance traces for d_8-κ-$(ET)_2Cu(SCN)_2$ at a selection of pressures with Fluorinert and Helium gas as the pressure media

Magnetoresistance oscillations at a selection of pressures for both the helium and Fluorinert experiments are shown in Figure 4.8. The first thing to notice is that the pressure medium appears to make a difference. Even looking at the traces, it is seen that the basic shape and the field at which superconductivity is suppressed are different between the two media. Superconductivity in the lower temperature Fluorinert measurement is more rapidly suppressed (3.0 kbar) than the higher temperature helium measurement (4.5 kbar), strongly suggesting that this effect is not due to temperature. The fact that the shape of the traces is different also suggests that it is not the case of slight inaccuracies in the pressure scale in one measurement; there is no

simple way to map one onto the other. It is possible to think that it might be a combination of pressure and temperature, but an examination of the α-orbit frequencies (see Figure 4.9) makes this very unlikely.

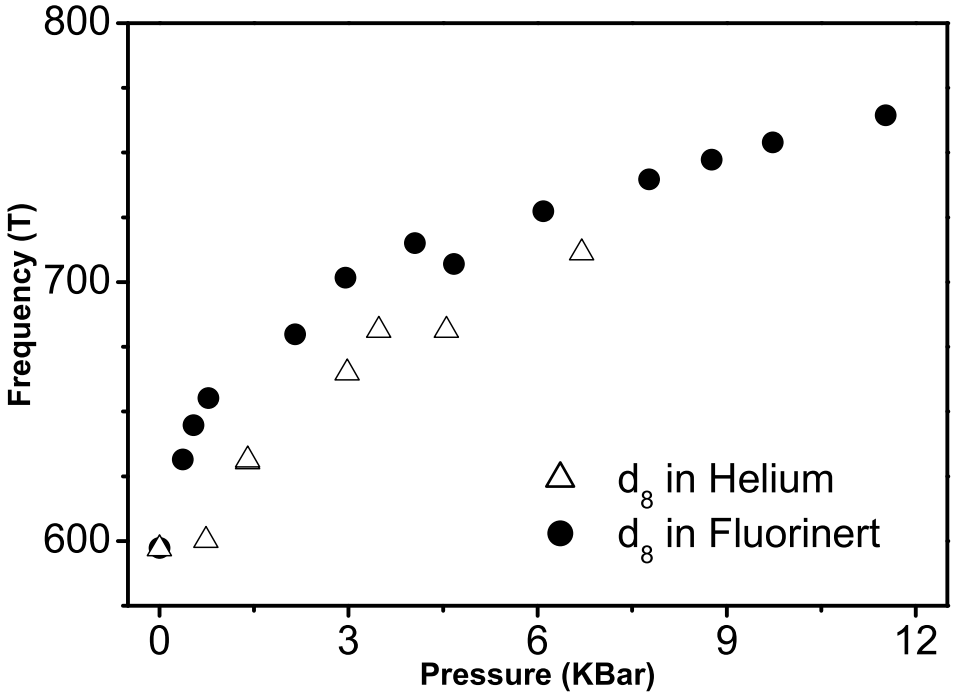

Figure 4.9: A comparison of the α-orbit frequencies for d_8-κ-$(ET)_2Cu(SCN)_2$ with Fluorinert and Helium gas as the pressure media

As the α-orbit is calculated for each pressure from a range of temperatures (see chapter 2) this leaves only an offset in the pressure scale. However it is not possible to map one set of points onto the other by a simple stretch or translation of the pressure scale. Another possibility would be that we have introduced shear stresses into the samples. However great care was taken to slowly cool the sample and we see no evidence of broadening of the superconducting transition with increasing pressure, indicative of a pressure gradient [55]. There was no observable degradation of the sample surface which would suggest it was reacting with the pressure medium. As we determined that the source of the sample does not affect the measurements by using

multiple samples from different growers, the only variable left to influence the results is the pressure medium itself.

This phenomenon is not limited to Fluorinert and helium. A comparison of the T_c data for the undeuterated sample with helium with a similar sample using petroleum spirit [6] shows noticeable differences (see Figure 4.10). Again this cannot be explained

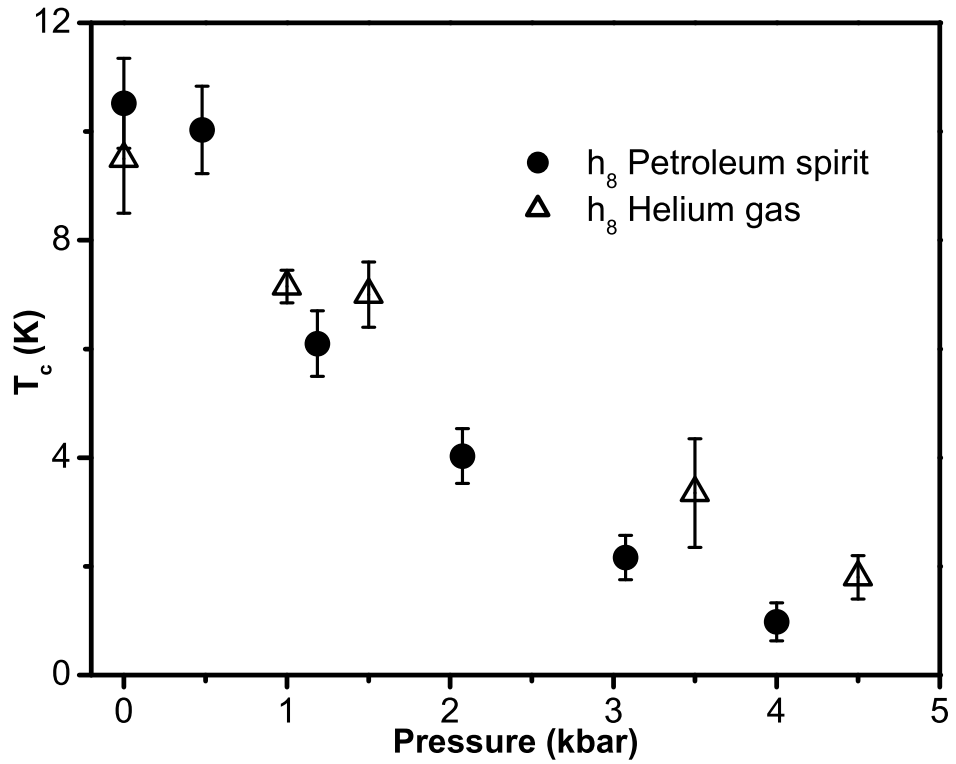

Figure 4.10: A comparison of T_c for h$_8$-κ-(ET)$_2$Cu(SCN)$_2$ with petroleum spirit and helium gas as the pressure media

by a shift in the pressure scale. However, if we compare experiments performed by different groups using the same pressure medium (e.g. Fluorinert: this work and [47]) we find an identical T_c dependence. This strongly suggests that in pressure experiments on this material the pressure scale will only be repeatable if the same pressure medium is used.

A good question is why would the pressure medium affect the properties of the sam-

ple? κ-(ET)$_2$Cu(SCN)$_2$ is highly compressible and anisotropic ($\kappa_a = 1 \times 10^{-3}$ kbar^{-1}, $\kappa_b = 2.5 \times 10^{-3}$ kbar^{-1} $\kappa_c = 3.6 \times 10^{-3}$ kbar^{-1}, linear anisotropic compressibility from pressure X-ray studies [48]). All the pressure media studied will be in solid form for at least some of the measurements so we have our soft sample frozen in a block of pressurized solid. All the pressure media used form relatively isotropic solids so the difference between their uniform contraction and the anisotropic contraction of the sample on cooling (anisotropic uniaxial pressure coefficients from thermal expansion measurements: a^*-axis ($\perp$ to the conducting plane)= -(6.2$\pm$0.25) K/kbar, b-axis = -(0.14$\pm$0.1) K/kbar, c-axis = +(3.44$\pm$0.15) K/kbar [49]) will result in non-hydrostatic stresses on the sample. This is not a new phenomenon as similar effects are seen in zinc [31][50].

Of these pressure media, helium is probably the most likely to be a true reflection of hydrostatic conditions as it is considered to be the softest and most hydrostatic pressure medium, even when solidified under pressure [31]. The solid bulk modulus of helium at a pressure of 1 kbar is $\sim$6 kbar [34]. This is much lower than the $\sim$123 kbar [48] shown by κ-(ET)$_2$Cu(SCN)$_2$. Recent work [55] has shown that Fluorinert FC75 remains hydrostatic to a pressure of 13 kbar at room temperature and that, with slow cooling ($\sim$1 K/min), hydrostaticity is maintained down to low temperatures. However, this was tested using the superconducting transition of lead, which is relatively isotropic and has a bulk modulus of 460 kbar, nearly four times that of our sample. This suggests that we may well see non-hydrostatic effects from Fluorinert in the pressure range measured, even before we consider the anisotropic nature of the sample.

The β-orbit frequency gives a measure of the magnetic breakdown orbit and hence reflects the size of the Brillouin zone in the conducting bc-plane. How it changes with pressure is a direct measure of the in-plane compressibility. Figure 4.11 shows how the β-frequency changes with pressure for both deuterated and protonated sample with three different pressure media. All samples show a low temperature in-plane compressibility of 0.4% kbar^{-1}. It is interesting to note that the rate of change of the

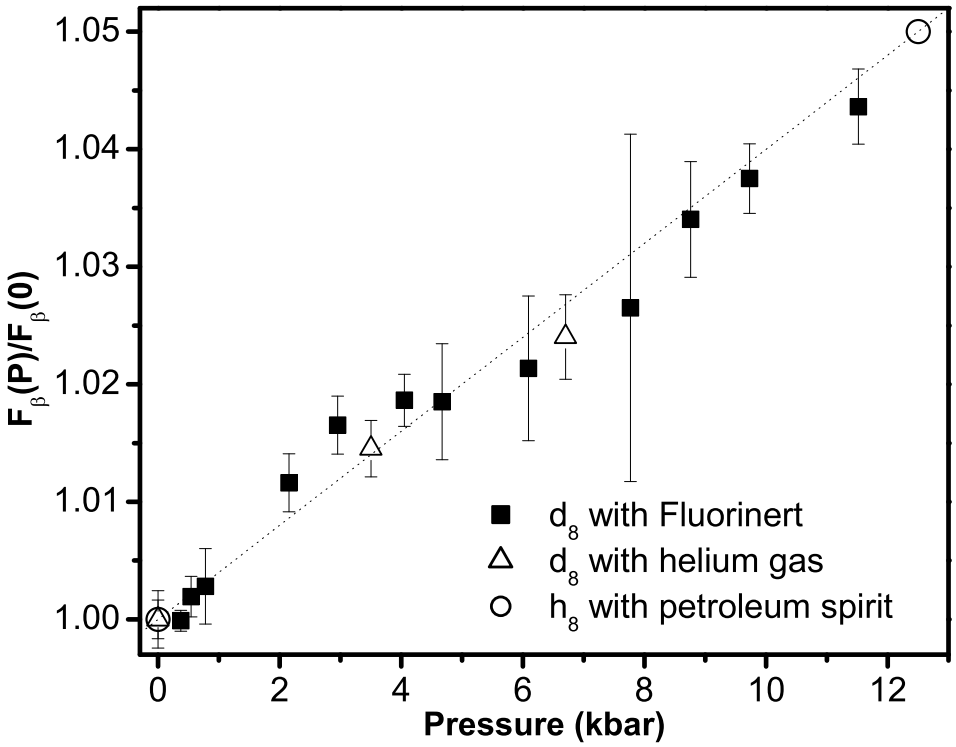

Figure 4.11: A comparison of the β-frequencies normalized to the ambient pressure value for both h_8- and d_8- κ-$(ET)_2Cu(SCN)_2$ with both helium and Fluorinert used as pressure media for the deuterated sample and petroleum spirit used for the protonated sample [6]. The dotted line is a guide to the eye.

β-frequency is independent of both deuteration and pressure medium. Comparing the two deuterated samples tells us that the previously discussed non-hydrostatic effects do not affect the overall size of the Brillouin zone; they appear to be confined to the quasi-two-dimensional pockets only. This also confirms that the differences seen are not due to an inaccurate pressure scale– this would give different sized Brillouin zones for the same "pressure" with different media. A comparison of the deuterated and protonated samples shows that deuteration does not affect the in-plane compressibility and hence a change in this is not the cause of the inverse isotope effect in this material. This on its own does not rule out the interplane compressibility playing a part, something which will be discussed later.

The exact effect of these stresses on κ-(ET)$_2$Cu(SCN)$_2$ is extremely hard to predict as unaxial strain has different effects depending on which in-plane direction is it applied. For example T_c has been observed to initially increase with strain $\parallel c$ but decrease if the strain is applied $\parallel b$ [51]. However, it may be possible to get an idea of the size of such strain by assuming that the maximum of any strain will be along the c-axis, from a consideration of the pressure coefficients. Uniaxial strain measurements on the c-axis of κ-(ET)$_2$Cu(SCN)$_2$ show an increase in T_c of $\sim$1 K under a pressure of 1 kbar [52], but relatively little change up to 0.5 kbar. As we do not see any overall enhancement of T_c, this puts a tentative upper limit on the difference in pressure experienced by the different axes. While higher strains reduce T_c again, they also affect the shape of the superconducting transition and eventually suppress it [51], something we do not observe.

4.4.2 Non pressure scale-dependent comparisons

This leaves us with the interesting situation of having several experiments on the same compound at pressures which cannot be directly compared due to having a pressure scale which is consistent only if the same pressure medium is used. However, even if we cannot relate the pressures measured, we would expect the characteristics to be broadly the same for any given pressure.

Firstly we shall look at the relationship between the critical temperature, T_c, and the effective mass of the α-orbit pocket, m^*_α, as Weiss *et al* [53] have suggested that there may be a universal relationship between these two quantities in κ-phase BEDT-TTF superconductors. Figure 4.12 shows such a plot for samples under three different pressure media. The data from all three samples varies in a qualitatively similar fashion. However, it does not seem possible to state that they obey the same relationship. The deuterated data form two sets: the majority of the Fluorinert data lie below the protonated measurement data while the majority of the helium data lie above it. The lack of any universal relationship, combined with the knowledge of non-hydrostatic effects due to pressure media, leads to the conclusion that it is not

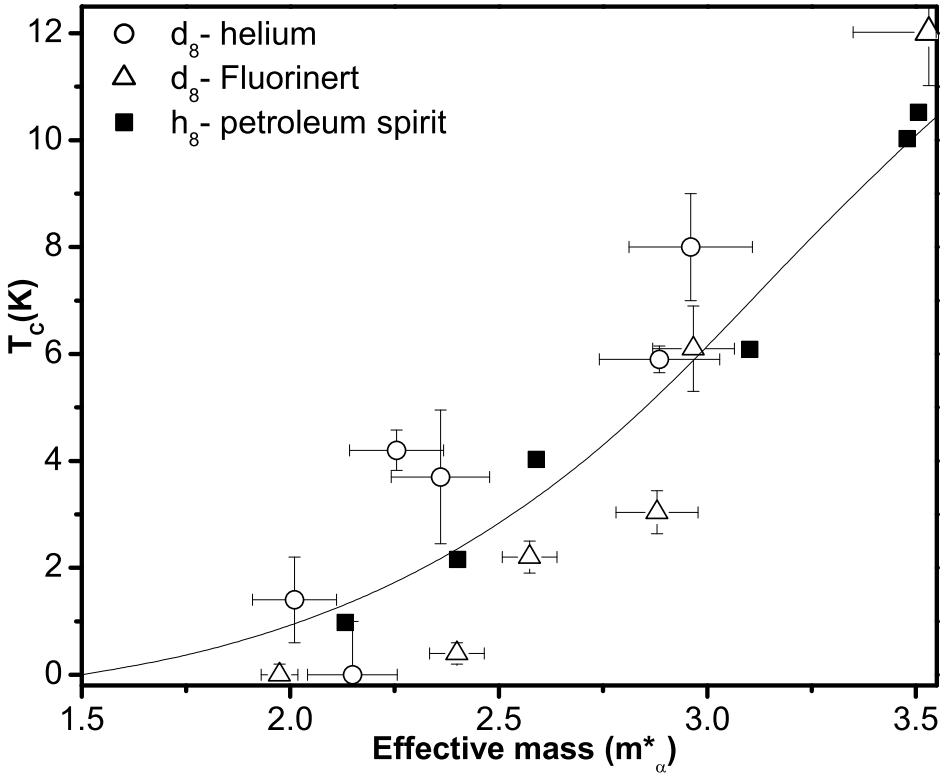

Figure 4.12: T_C against m^*_α for both h_8- and d_8- κ-$(ET)_2Cu(SCN)_2$ with petroleum spirit [6], Fluorinert and helium gas as the pressure media. The curve is a linearized Eliashberg solution from [54] as seen in [42]

possible to compare effective mass measurements under different pressure media in this material. m^*_α is affected by small non-hydrostatic effects, a topic which would be worthy of further investigation.

However, there are other characteristics of the material which were measured at the same temperature and pressure so we shall investigate if these are pressure-media independent, starting with the frequency of the α-orbit and T_c.

Figure 4.13 shows very good correlation between T_c and the α-orbit frequency for three different pressure media and both protonated and deuterated samples. Both protonated and deuterated samples show a suppression of T_c at very similar values of the α-frequency. Such strong correlation between T_c, indicative of the bulk prop-

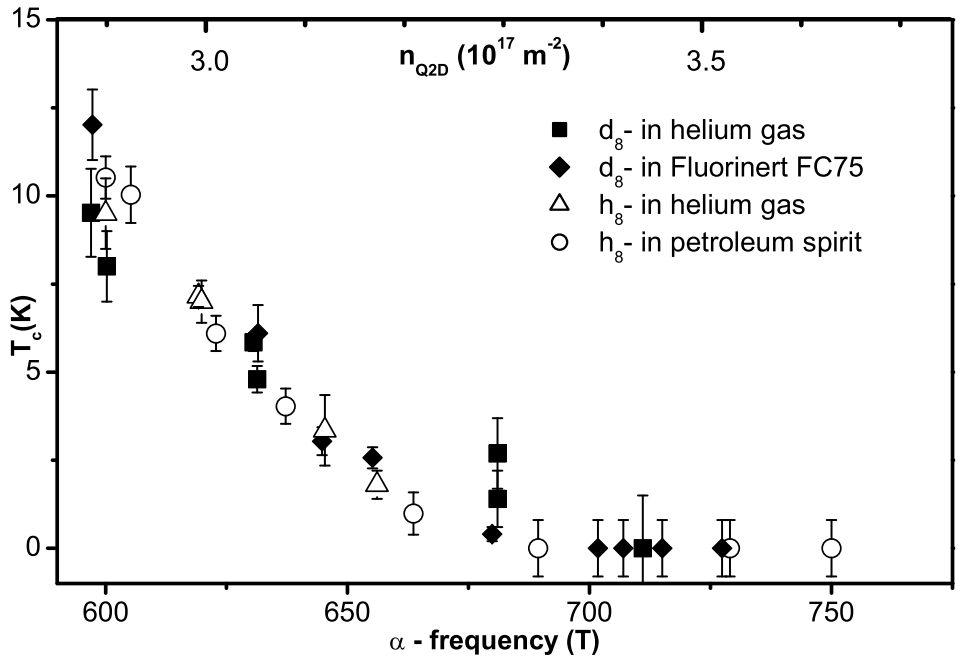

Figure 4.13: T_C against α-orbit frequency for both h_8- and d_8- κ-$(ET)_2Cu(SCN)_2$ with petroleum spirit [6], Fluorinert and helium gas as the pressure media

erty of superconductivity, and the α-orbit frequency, which describes the quasi-two-dimensional Fermi surface pocket, suggests that superconductivity in this material is due to the quasi-two-dimensional conducting planes. Earlier work [42] suggested that small changes in Fermi surface topology, particularly in the interlayer direction, were mainly responsible for changes in T_c; This suggestion cannot be true and was, at least in part, based on the assumption of the transferability of the pressure scale. Any such contribution would have to be small. Instead, Figure 4.13 suggests that a smaller α-frequency, and hence smaller quasi-two-dimensional Fermi surface pocket, leads to a higher T_c. The fact that the protonated sample at ambient pressure displays an α-frequency of 600 ± 1 T and the deuterated sample an α-frequency of 597 ± 1 T [42] may be important in explaining the inverse isotope effect.

Even though κ-$(ET)_2Cu(SCN)_2$ has a three-dimensional Fermi surface due to a measurable interlayer transfer integral [39], this is more than three orders of magnitude

smaller than the interdimer transfer integrals [39], which give a good measure of the intralayer bandwidth. This allows us to treat it as a two-dimensional system in the following calculations.

We shall now look at relating the density of charge carriers to other measured properties [56]. Quantum mechanics [19] tells us we can only have a certain number of states, N, in a given volume of phase space:

$$N = 2\left(\frac{1}{2\pi}\right)^{p} V_k V_r, \tag{4.2}$$

where p is the number of dimensions, V_k and V_r are the k-space and real space volumes respectively and the initial 2 is because, as electrons are Fermions, we can have two per available state. In a two-dimensional system the number of states is

$$N = \frac{1}{2\pi^2} A_{\mathrm{FS}} V_r, \tag{4.3}$$

where A_{FS} is the area of the two-dimensional Fermi surface pocket. So we can write carrier density, $n_{Q2D} = N/V_r$, as

$$n_{Q2D} = \frac{1}{2\pi^2} A_{\mathrm{FS}}. \tag{4.4}$$

Now, from equation 52 in chapter 2, we know that the area of this orbit is given by

$$A_{\mathrm{FS}} = \frac{2\pi e}{\hbar} F_\alpha, \tag{4.5}$$

where F_α is the frequency of the α-orbit. Combining equations 4.4 and 4.5 gives

$$n_{Q2D} = \frac{e}{\pi\hbar} F_\alpha. \tag{4.6}$$

This allows us to relate the carrier density for the quasi-two-dimensional Fermi surface pocket to the oscillation frequency of that pocket. The top axis of Figure 4.13 shows that the quasi-two-dimensional carrier density, nQ2D, increases by nearly one third,

vastly more than would be expected from just the compression of the Brillouin zone. If we consider the increase in size of the β-orbit to be a measure of the decrease in size of the Brillouin zone we find that, over a similar range, it decreases by only $\sim$5%. The pressure dependence of the lattice parameters from pressure X-ray studies [48] also gives a similar decrease of the Q2D unit cell size of $\sim$5% over $\sim$10 kbar.

The extra charge carriers must come from somewhere, and the most likely place is the quasi-one-dimensional sections of the Fermi surface (as the experiments are performed at relatively low pressures, the overall carrier density per unit cell will be constant). Thus the result of applying pressure to the system can be thought of as the transfer of charge carriers, in this case holes, from the quasi-one-dimensional section to the quasi-two-dimensional section. A similar process is seen in cuprate superconductors, where pressure transfers holes into the quasi-two-dimensional conducting layers of CuO_2 from insulating charge reservoir layers [57]. In both cases, pressure increases the number of charge carriers in the superconducting layer. However, it is not possible to determine from these experiments whether it is this increase, or the associated decrease in other areas, that is the cause of the suppression of superconductivity in this material.

Due to this in-plane transfer of charge in κ-$(ET)_2Cu(SCN)_2$ it seems that the in-plane pressure, not the bulk pressure, is more relevant in determining its superconducting properties. This idea has been supported by ac-susceptibility measurements under pressure, demonstrating a link between compression of the in-plane unit cell and superconducting properties [43].

4.4.3 In-plane transfer integrals

We shall now consider the in-plane transfer integrals in this material. Transfer integrals give a measure of how easy it is for a quasiparticle to move from one atom, or in this case a dimer, to the next. The cross-sectional area of the α-pocket is determined by the ratio of t_b/t_c [39] and an increase in t_b/t_c elongates the overall Fermi surface cross-section in the k_c-direction by 'fattening' this pocket [6]. As a consequence, the

corrugation of the quasi-one-dimensional sheets changes somewhat; the regions next to the breakdown gap become slightly more pointed, whilst away from the gap the sheets flatten slightly. Theoretical calculations [59] also support this, showing that this ratio increases with pressure, leading to a change of Fermi surface shape and consequently, a change in the nesting properties.

This ratio can be determined, by using the method in [58], from the effective dimer model, which has been shown to accurately represent the quasiparticle dispersion, $E(k)$ [39]:

$$E(k) = \pm 2\cos\left(\frac{k_b b}{2}\right)\sqrt{t_{c1}^2 + t_{c2}^2 + 2t_{c1}t_{c2}\cos(k_c c)} + 2t_b\cos(k_\perp b) + 2t_a\cos(k_\perp a) \tag{4.7}$$

where a, b and c are the lattice parameters (which are, themselves, pressure dependent and the values have been taken from pressure X-ray work [48] [1]) and t_a, t_b and t_{c1} and t_{c2} (the arrangement of the lattice means that the transfer integral depends on which ET molecule the charge carrier moves from and to in the k_c direction) are the respective transfer integrals and the "$+$" results in the quasi-one dimensional sheet and the "$-$" in the quasi-two dimensional pocket. This work also showed that t_a is several orders of magnitude smaller than the other integrals, so we shall ignore it here. In addition, it has been shown [6] that the difference between t_{c1} and t_{c2} is much smaller than their magnitude, so we shall approximate

$$t_c \approx t_{c1} \approx t_{c2}. \tag{4.8}$$

This allows us to write the intralayer dispersion as:

$$E(k) = \pm 2\cos\left(\frac{k_b b}{2}\right)\sqrt{2t_c^2 + 2t_c^2\cos(k_c c)} + 2t_b\cos(k_\perp b). \tag{4.9}$$

[1] There is a typographical error in the equation for the c-axis lattice parameter's pressure dependence in this paper (the crystal appears to get larger with increasing pressure). However, using the data points given the paper gives a sensible result and this has been used here.

Manipulating equation 4.9 leads to

$$k_c = \pm\frac{2}{c}\cos^{-1}\left(\frac{t_b}{t_c}\frac{\cos(k_b b)}{2\cos(\frac{k_b b}{2})} - \frac{E(k)}{t_c}\frac{1}{4\cos(\frac{k_b b}{2})}\right) \tag{4.10}$$

and this allows us to plot out the Fermi surface in k-space [39], giving the areas of the α- and β-orbits (see figure 4.14). The size of these is governed by the ratios t_b/t_c and

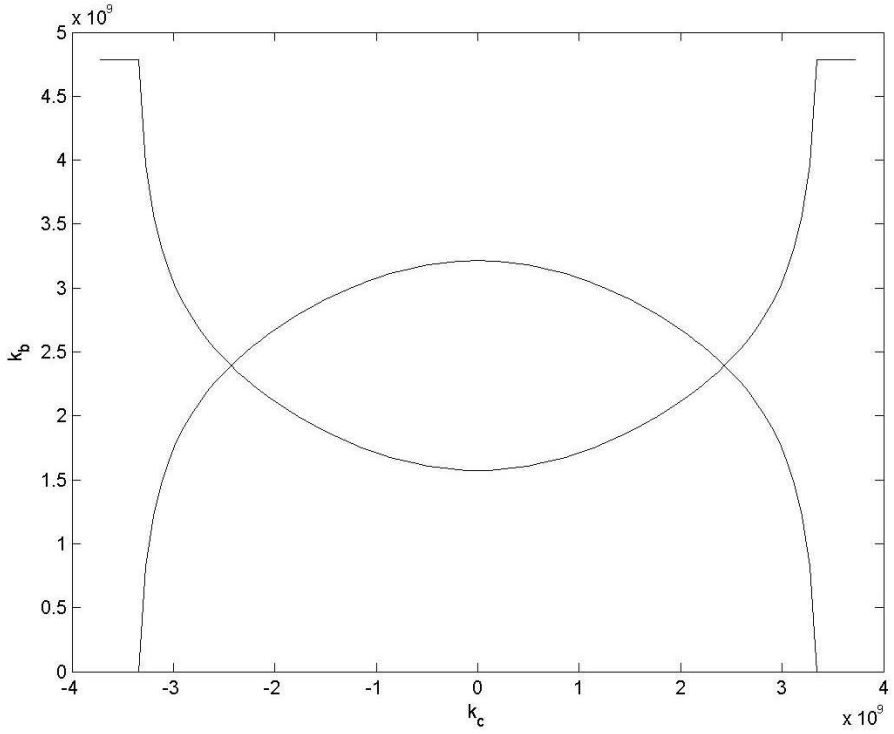

Figure 4.14: Plot of k_c against k_b from the effective dimer model. The area under the lower curve corresponds to half the area of the β-orbit and the area between the two curves is the α-orbit

E/t_c and there is only one value which gives the correct experimentally determined sizes for both orbits. The simplest method to determine this size is to calculate the areas, in terms of the frequency measured, for a range of t_b/t_c and E/t_c for each orbit and them plot them both on a contour map; the intersection of the two contours of the correct value gives t_b/t_c and E/t_c (see Figure 4.15). Once a rough value is known, a more accurate value can be determined by narrowing the search range and repeating

the calculations.

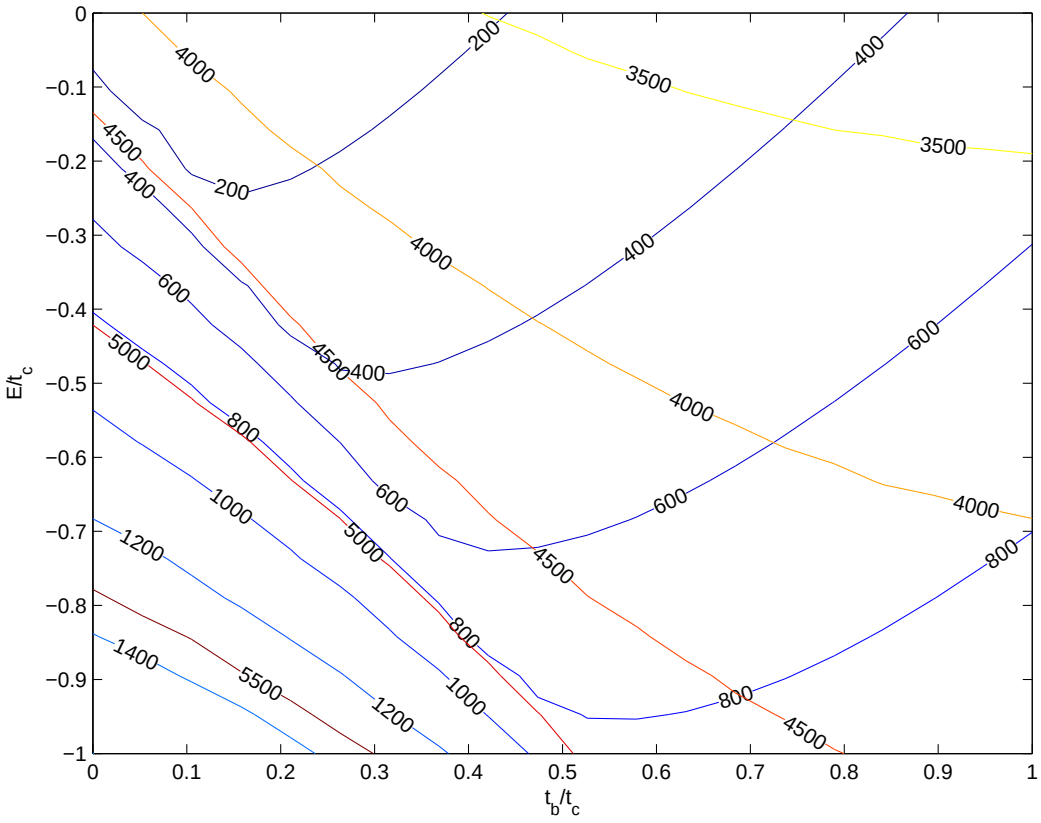

Figure 4.15: Contour plot of t_b/t_c against E/t_c for an example data point. The solution here is near to where the 4000 and 600 contours cross.

The lower fields used in the helium measurements made the detection of magnetic breakdown orbits more difficult and hence we see far fewer points than from the Fluorinert measurements. Comparing the ratio t_b/t_c for deuterated and protonated samples with a range of pressure media (see Figure 4.16) we once again see pressure media dependent effects. This is to be expected if the pressure media are creating small shear stresses in the samples leading to greater compression along one axis, causing a change in the transfer integrals and Fermi surface shape. Pressure causes an increase in t_b/t_c in the deuterated sample. As both the helium and Fluorinert deuterated measurements show larger increases in t_b/t_c with pressure than in the protonated sample under petroleum spirit this may be a real increase. This is because helium is the 'softest' pressure medium and the helium points lie in between the two

'harder' pressure media, Fluorinert and petroleum spirit. If this effect was purely due to pressure media, we would expect the helium points to be either to the top or bottom of the other points. How large an increase this really is cannot be determined here.

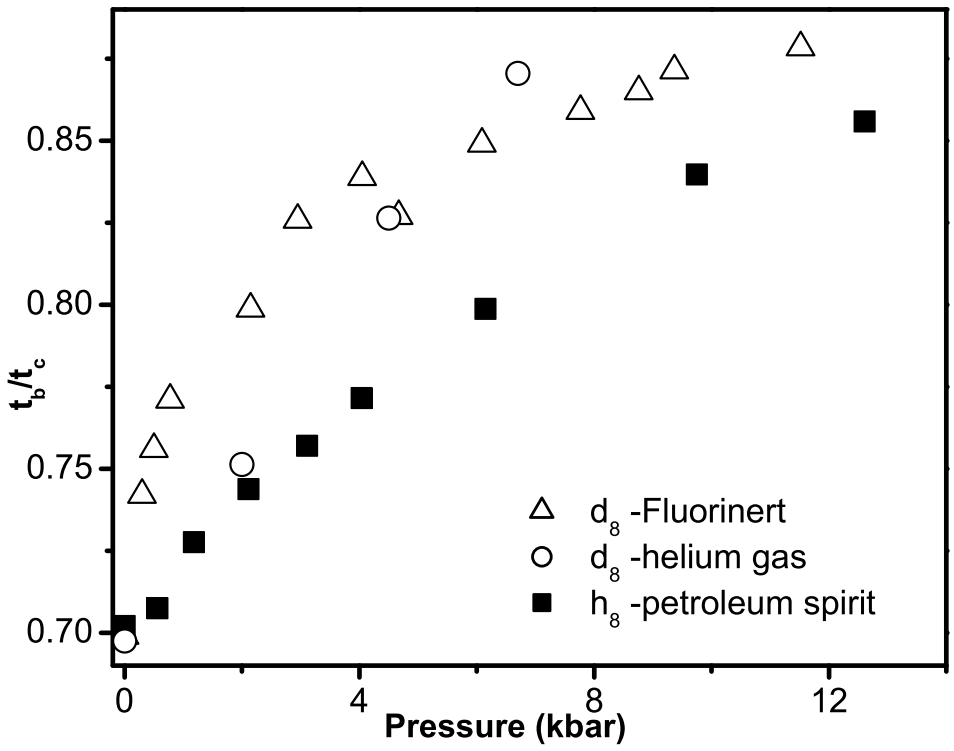

Figure 4.16: Plot of t_b/t_c against pressure for both deuterated and protonated [6] κ-(ET)$_2$Cu(SCN)$_2$ using different pressure media

One additional source of error is the X-ray determination of the lattice parameters under pressure [48]. These were made using Fluorinert as a pressure medium at room temperature whereas these experiments were at a range of temperatures. We are forced to assume that these will not change much on cooling and also that the pressure medium will not have affected the results, despite the findings of this work so far. This is reasonable as it is believed that the non-hydrostatic effects are caused by freezing of the pressure media. However, we cannot rule this out for certain using the work done here.

As we have shown that it is possible to eliminate pressure media dependent effects by choosing variables which are not directly linked to the measured pressure (as for T_c and the α-orbit frequency in the previous section of this chapter), we shall attempt a similar approach here. Figure 4.17 is a plot of T_c against t_b/t_c. Here we see similar

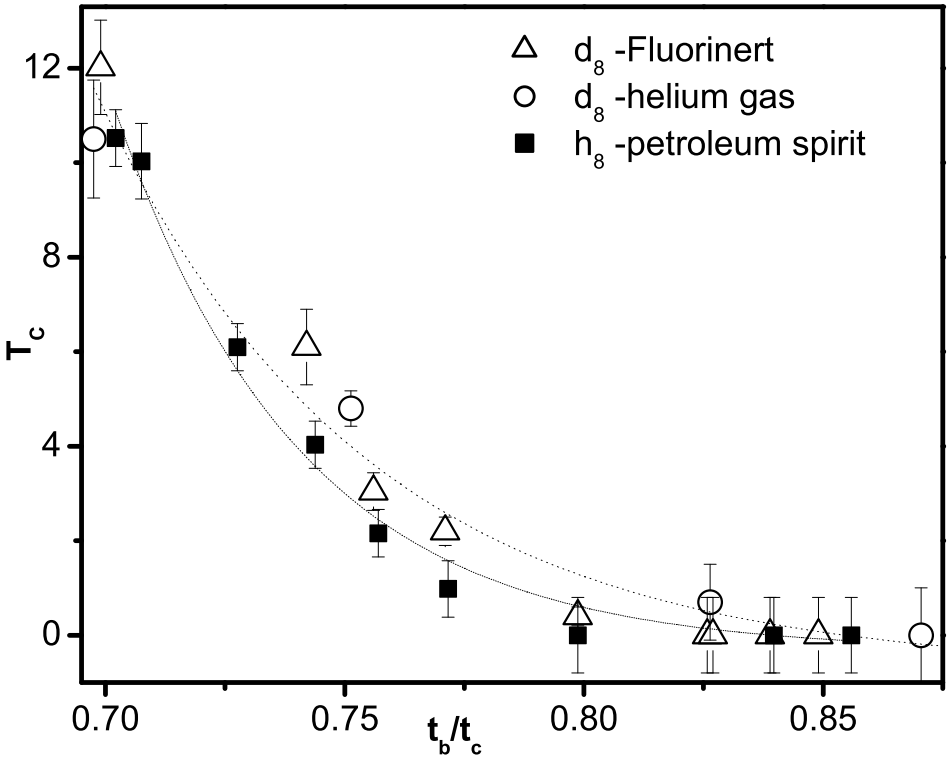

Figure 4.17: Plot of T_c against t_b/t_c for both deuterated and protonated [6] κ-$(ET)_2Cu(SCN)_2$ using different pressure media. The lower dotted line is a three term exponential decay fit to the h_8 data and the upper dotted line is a similar fit to the combined d_8 data

trends for for all three measurements, with T_c being suppressed over a similar range of t_b/t_c. However it does appear that T_c is initially more rapidly suppressed in the protonated sample than either of the two deuterated samples. The fact that the helium and Fluorinert points appear to lie on approximately the same curve suggests that the difference is not due to different pressure media in this case. The curves drawn through the data are three term exponential decay fits to all the deuterated

and protonated data. These are not intended to be an accurate representation of the relationship, although they do serve to show the difference in initial slope upon deuteration. While this difference is small, it does appear to be real.

4.5 Conclusion

A comparison of magnetotransport measurements on κ-(ET)$_2$Cu(SCN)$_2$ under three different pressure media has shown that pressure is not a transferable parameter in this material. This is possibly due to the anisotropy of the material; on cooling it contracts by different rates along each axis and this introduces non-hydrostatic strain when combined with a much more uniform, but frozen, pressure medium. Neither the pressure measured nor m^*_α can be compared between different pressure media. However good media-independent correlation is seen between the number of charge carriers in the α-pocket, n_{Q2D} and T_c. This suggests that the action of pressure on the system transfers carriers from the quasi-one-dimensional Fermi surface sections to the quasi-two-dimensional Fermi surface sections. This result has parallels with the case of the cuprate superconductors: pressure causes the transfer of holes to the superconducting sections of the Fermi surface which leads to the eventual suppression of superconductivity in both materials.

As for the observed inverse isotope effect upon deuteration in this material, it is possible to state that it is not due to a change in the in-plane compressibility of the material from a comparison of the β-orbit frequencies. A comparison of T_c and the α-orbit frequency shows a strong relationship between the two for both protonated and deuterated samples. As the deuterated sample displays a lower α-orbit frequency at ambient pressure [42] than the protonated sample, this suggests that the size of the quasi-two-dimensional Fermi surface section is important in explaining this effect. The comparison of t_b/t_c with T_c supports this idea, linking an elongation of the overall Fermi surface cross-section and "fattening" of the quasi-two-dimensional pocket to a decrease in T_c. Whether the small changes in this relationship upon deuteration and

the associated changes in the quasi-one-dimensional section of the Fermi surface are important is something that warrants further investigation.

Chapter 5

Investigation into the phonon modes of d_8-κ-$(ET)_2Cu(SCN)_2$ using infrared reflectivity

5.1 Overview

Experiments on κ-$(ET)_2Cu(SCN)_2$ has shown that the phonon modes present in the infrared spectra shift linearly with pressure [60]. Comparison of the modes also present in the Raman spectra enabled the pressure dependence of the electron-phonon coupling strength to be evaluated. A comparison of this to the value given by the weak coupling limit of BCS theory suggested this material is not a simple BCS superconductor [60]. However, in one of the major modes of interest, the central C=C mode, this dependence can only be inferred as it is masked by a Fermi resonance with the C–H bond [61]. This is where the frequency of one mode is at nearly the same frequency as a harmonic of another mode. Instead of one strong mode, we see two, each shifted to higher and lower frequencies than one would expect. This occurs because the levels can interact quantum mechanically due to anharmonic terms in the potential energy. It was first observed by Fermi in the Raman spectra of CO_2 [62]. Studying a deuterated sample allows direct observation of this mode because the C–D mode is sufficiently

softened to reveal the C=C line shape. This mode is of particular interest because it is strongly active in the infrared due to strong electron-phonon coupling [63].

In this chapter, I present the results of an investigation into the pressure dependence of this and another strongly IR-active mode, the C–S mode [64], at about 880 cm^{-1}. The difference between the two modes is discussed in light of the fact that one of them is symmetric, and hence only IR-active through electron-phonon coupling, while the other is antisymmetric. The deuterated form is a superconductor below $\sim$11 K, however this is suppressed at pressures above 6 kbar [43]. If electron-phonon interactions are important in the superconductivity mechanism a sudden change in the electron-phonon coupling constant would be expected at this pressure.

5.2 The experiment

My experiments were performed using the diamond anvil pressure cell with an argon gas pressure medium in the range of 700 cm^{-1} to 6000 cm^{-1} and a resolution of 4 cm^{-1} using the Bruker IFS 66v with a polariser and KBr beamsplitter. A pressure range of up to 11 kbar was investigated. This pressure was measured using a ruby fluorescence gauge. All measurements were performed at room temperature (294 K). A background measurement was taken using a gold mirror inserted inside the cell after the experiments had been completed. Short term fluctuations were removed by taking a reference spectrum of the top diamond surface after every measurement. The b-c crystal plane was in contact with the diamond surface.

5.3 Results and Analysis

The observed infrared spectrum of d_8-κ-$(ET)_2Cu(SCN)_2$ is quite dramatically altered just by being studied through a diamond window (Figures 5.1 and 5.2).

The absolute intensity is lower under the diamond because the difference between the refractive indices is lower, and hence less radiation is reflected. The shape is also different because, while air always has a lower refractive index, diamond has either a

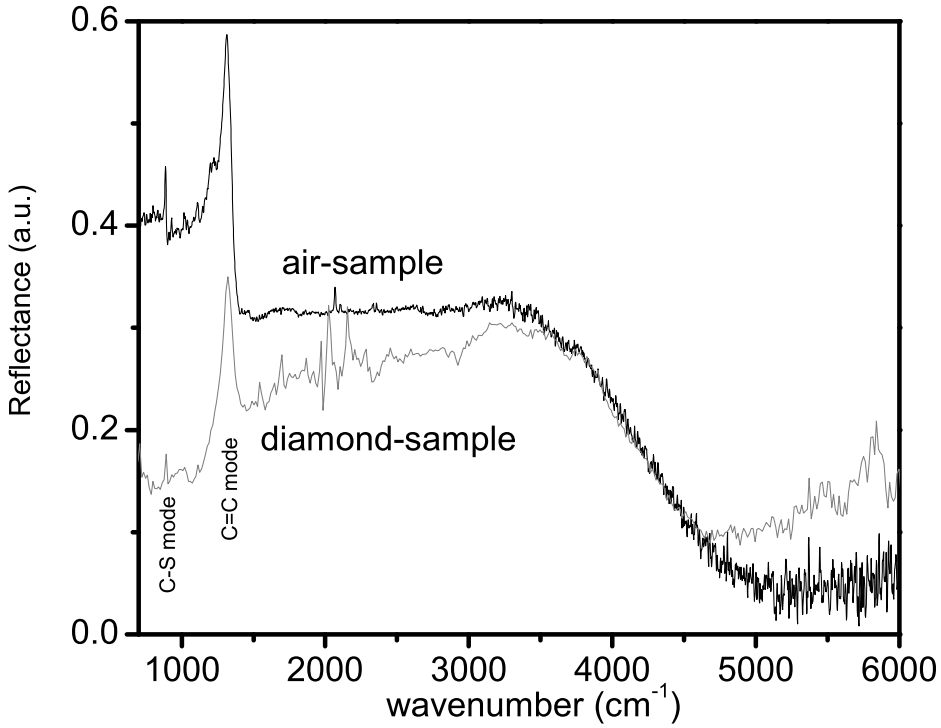

Figure 5.1: Polarized reflectance spectra of d_8-κ-$(ET)_2Cu(SCN)_2$, parallel to the b-axis, as seen through both air and diamond at ambient pressure and room temperature.

lower or higher refractive index, dependent on the frequency. A higher level of noise is also seen as the pressure cell gives a much smaller signal than a sample in air. The features visible around 2000 cm^{-1} are due to the diamond absorption, which has been mostly removed using the method discussed in Chapter 3.

Concentrating on the region containing the features which motivated these experiments we see that both the 880 cm^{-1} mode and the C=C mode shift with pressure (see Figure 5.3).

The fitting of both these peaks can be performed relatively simply as there is no Fermi resonance. The frequencies of these peaks can be extracted by fitting the Drude-Lorentz model directly to the reflectivity or from the peak frequencies of the real part of the complex conductivity. As both models yield the same results

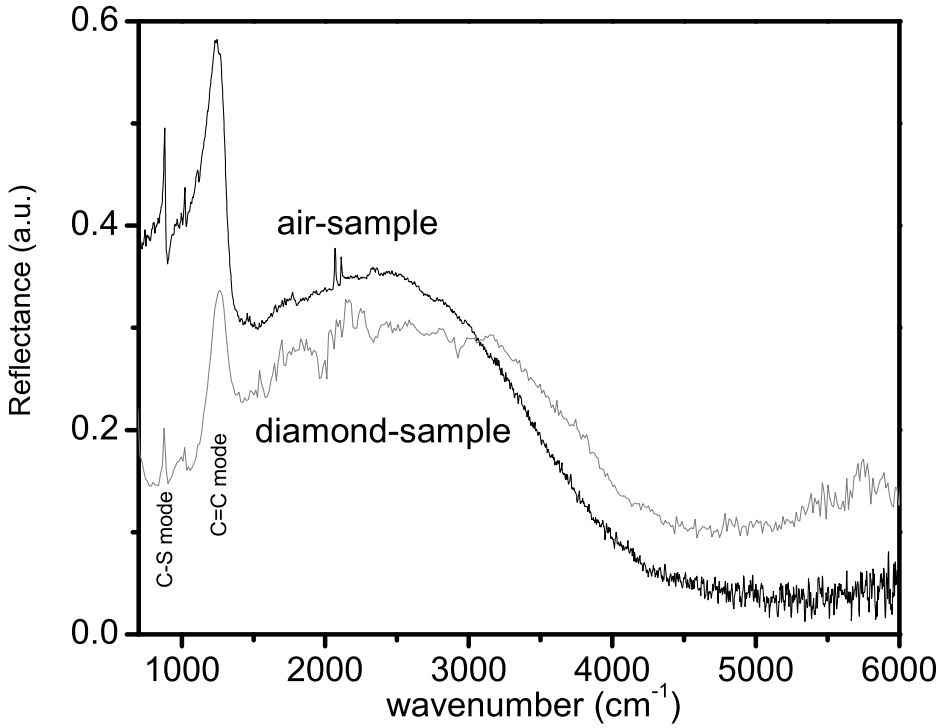

Figure 5.2: Polarized reflectance spectra of d_8-κ-$(ET)_2Cu(SCN)_2$, parallel to the c-axis, as seen through both air and diamond at ambient pressure and room temperature.

to within experimental errors [60], only the reflectivity has been analyzed here (see Figures 5.4 and 5.5). However the mid-infrared "hump", centred around 3000 cm^{-1}, cannot be reliably fitted for these experiments due to the sample becoming partially detached from the surface. This gap, while very small, is enough to change the higher wavenumber end of the spectrum in a non predictable manner which changes with pressure as the gap increases and decreases. It is believed that this is effectively a single interference fringe caused by the gap and not a real feature of the spectrum. This distortion is not seen at the low wavenumber end as the wavelength is longer than the gap so the phonon modes are not affected. This means the exact position of this feature and its pressure shift cannot be determined in these measurements.

Both phonon modes display linear shifts with pressure (Table 5.1). The much larger

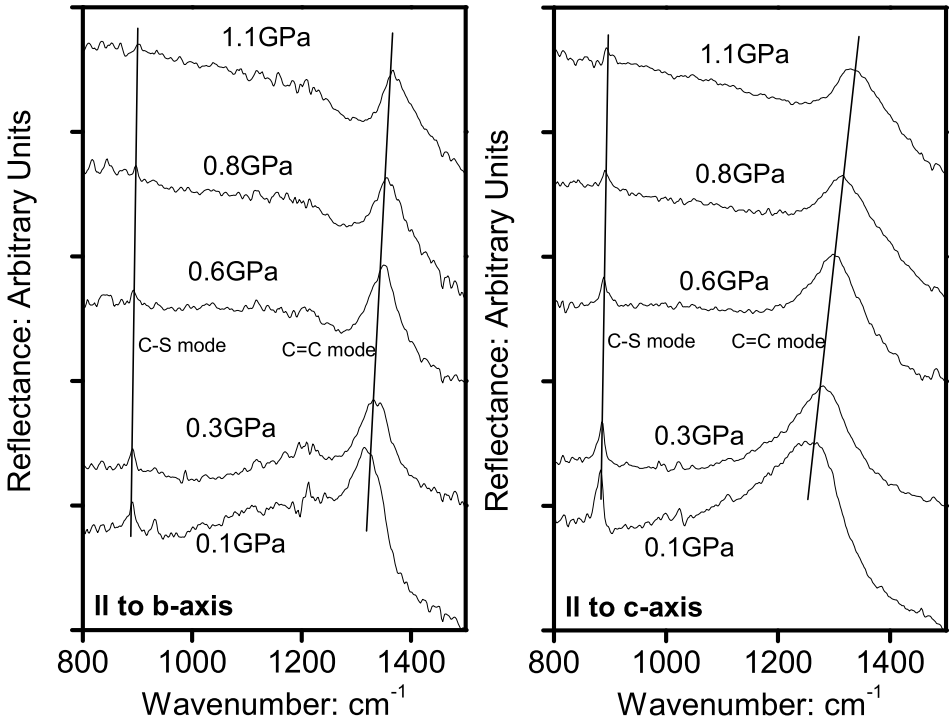

Figure 5.3: Polarized reflectance spectra of d_8-κ-$(ET)_2Cu(SCN)_2$, at room temperature and a range of pressures showing the movement of phonon modes. The lines are drawn as a guide to the eye.

errors in the C–S mode frequency result from this being a much weaker mode (see Figure 5.3) and hence noise has a larger effect. Comparing these results to work on the protonated sample (see Table 5.2) we see that both samples display a near identical shift in pressure of the C–S mode at ∼880 cm^{-1} of $\sim 0.1\%$ $kbar^{-1}$. In addition, the central C=C mode displays a remarkably similar shift with pressure in both samples, indicating that the coupled oscillator model used for the protonated sample [60] is very successful in separating the different modes from the Fermi resonance.

The C=C mode displays linear pressure dependence throughout the range investigated. As this mode is a fully symmetric A_g mode [64], it can only be observed in the infrared due to electron-phonon interactions, in this case coupling to the mid-IR band. Hence the pressure dependence of this mode gives us information about the pressure

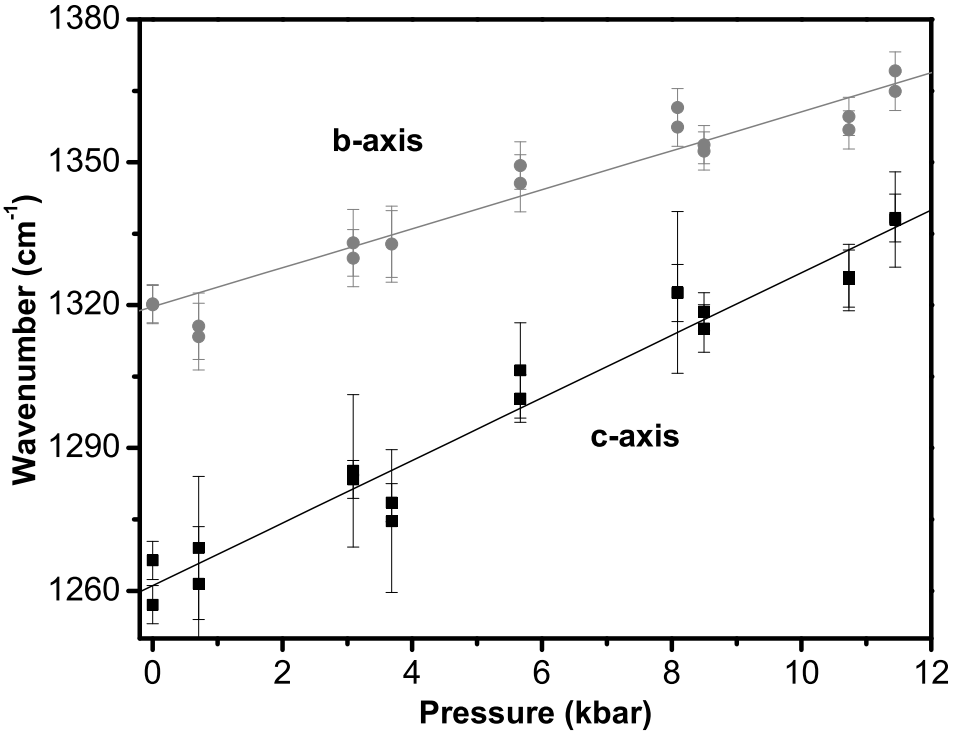

Figure 5.4: Peak position of the central C=C mode in d_8-κ-$(ET)_2Cu(SCN)_2$, at room temperature and a range of pressures for both the b and c-axis polarizations

Phonon Mode	b-axis cm^{-1} + % $kbar^{-1}$	c-axis cm^{-1} + % $kbar^{-1}$
C=C	1320 + 0.3	1261 + 0.5
C–S	889 + 0.1	883 + 0.1

Table 5.1: Positions and pressure shifts of studied phonon modes in d_8-κ-$(ET)_2Cu(SCN)_2$

Phonon Mode	b-axis % $kbar^{-1}$	c-axis % $kbar^{-1}$
C=C	+0.25	+0.55
C–S	+0.071	+0.1

Table 5.2: Pressure shifts of phonon modes in h_8-κ-$(ET)_2Cu(SCN)_2$ (from [65])

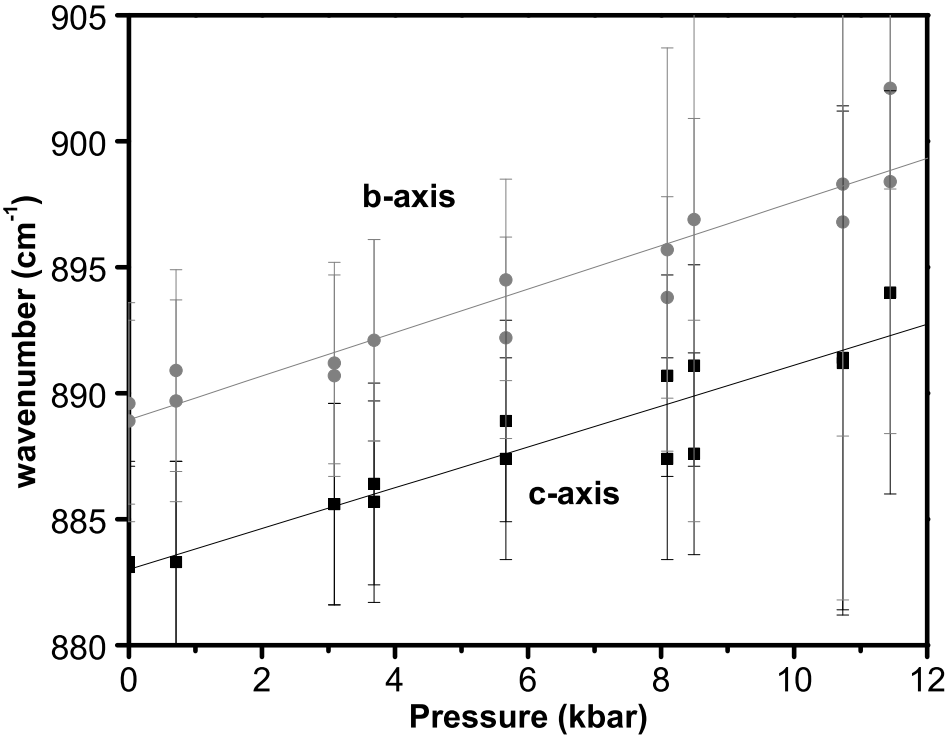

Figure 5.5: Peak position of the C–S mode in d_8-κ-$(ET)_2Cu(SCN)_2$, at room temperature and a range of pressures for both the b and c-axis polarizations

dependence of the electron-phonon coupling constant, λ_p. Raman studies [66] have shown that the bare C=C mode displays a much smaller linear pressure dependence. This difference is of an order of magnitude, 0.04% kbar^{-1}. In addition, the C–S mode is asymmetric and so does not rely on electron-phonon coupling and again we see a much smaller shift with pressure than the C=C mode. This suggests that the majority of the change must be due to changes in the electron-phonon interaction.

Superconductivity is suppressed in this material at a pressure of $\sim$6 kbar [3]. However we see no sudden change in the C=C mode and hence λ_p. This suppression is accompanied by a strong decrease in effective mass, m^*, which is then followed by a small pressure dependence in the non-superconducting state [6]. As m^* is the band mass renormalized by both electron-electron and electron-phonon interactions

and infrared measurements probe only the "bare" band mass, the small linear pressure dependence of the latter [65] suggest that electron correlations are responsible for the large change in m^* at suppression of superconductivity. As no similar change at this pressure is seen in the C=C mode, and hence in the electron-phonon interactions, this supports the idea that superconductivity in this material is not BCS-like and that electron-electron interactions may well play an important part.

Chapter 6

Temperature and Pressure dependence of the Infrared Reflectivity of d_8-κ-$(ET)_2Cu[N(CN)_2]Br$

6.1 Introduction

This chapter presents what are believed to be the first attempts to study both the pressure and temperature dependence of the reflectivity of an organic molecular metal in the infrared. The advantage of these techniques is that they allow movement along both axes of the pressure-temperature diagram without chemical substitution. The complexities of such measurements will be discussed along with the results for d_8-κ-$(ET)_2Cu[N(CN)_2]Br$. This material was chosen as it is similar to κ-$(ET)_2Cu(SCN)_2$, already studied in this work; the different anion end group effectively moves it along the pressure axis of the phase diagram (see Figure 1.3 chapter 1). It also has a paramagnetic insulator to unconventional metal transition which can be probed using the present equipment. A deuterated sample was chosen as the lack of Fermi resonance in the phonon modes makes fitting these modes using Lorentzian oscillators, and hence

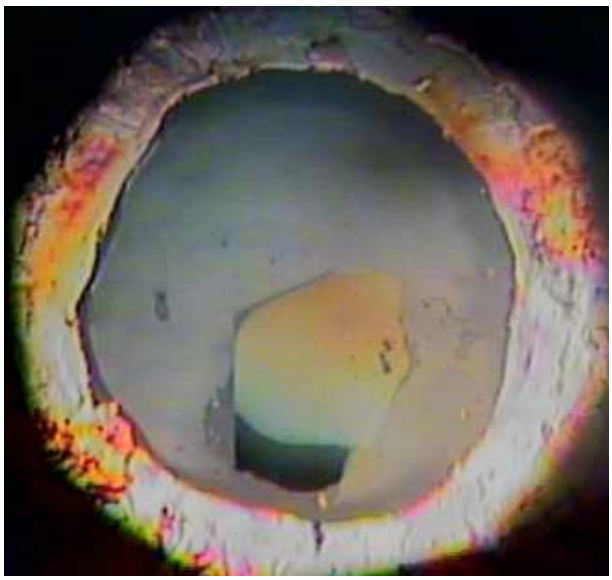

Figure 6.1: d_8-κ-BEDT-$TTF_2Cu[N(CN)_2]Br$ inside the loaded pressure cell. The outer bright ring is a copper gasket, the black area is the edge of an aperture on the optics. The faint redish circle to the right of the sample is a ruby chip. The hole is less than 0.5 mm diameter

removing them, much easier [60]. This is necessary for fitting with the extended Drude model. The extended Drude model is used to study the conductivity, effective mass and scattering rate. These results are compared to those for high temperature superconductors and ferromagnetic materials also studied using this method.

d_8-κ-$(ET)_2Cu[N(CN)_2]Br$ is an insulator at room temperature and pressure. This is unusual as it has a half filled band, which would make us expect it to be metallic, according to band theory. However, strong electron-electron interactions localize the electrons to each site, forming a Mott insulating state [3]. A combination of high pressure and low temperature can force it into a metallic state (see Figure 6.2).

6.2 The experiment

These experiments were performed using a diamond anvil cell with argon as a pressure medium, a specially designed cryostat to cool it and the Bruker IFS 66V Fourier transform spectrometer, as discussed in chapter 3. Temperatures from 50 K to 294 K

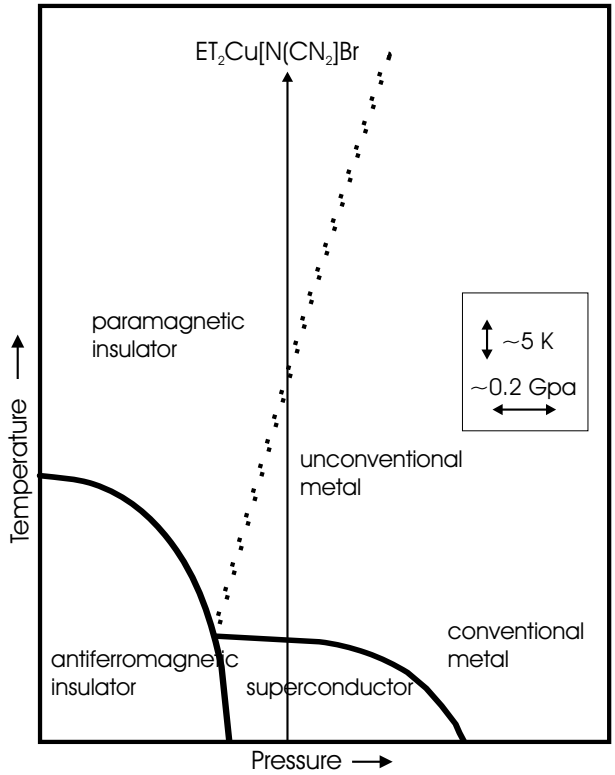

Figure 6.2: Schematic phase diagram of the κ-BEDT-TTF$_2$Cu[N(CN)$_2$]Br, after [7]

were investigated in conjunction with pressures of up to 11.5 kbar. Initial work was performed with TMTSF$_2$PF$_6$, but the phenomenon of mechanical twinning [3] made good surface contact with the diamond impossible to obtain. When force was applied to the sample to ensure such contact, a ridge was seen to form on the flat side in contact with the diamond (see Figure 6.3). X-ray diffraction has shown that these steps or kinks are due to mechanical twinning with the boundary on the (210) plane [3]. The lack of good contact across the whole surface meant that the sample lifted off when pressure was applied in the vast majority of cases and so the sample could only be fully measured at ambient pressure. Some results obtained from this sample at ambient pressure can be found in appendix A. The rest of this chapter is devoted to d$_8$-κ-(ET)$_2$Cu[N(CN)$_2$]Br.

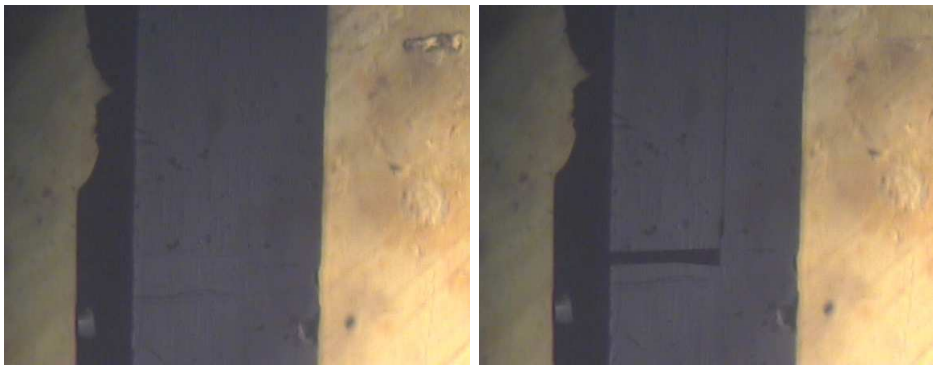

Figure 6.3: Mechanical twinning seen in TMTSF-PF_6. Before (left) and after (right) force was applied to rear of sample

6.3 Results and Analysis

6.3.1 Correcting and filtering the data

Firstly the raw spectra were filtered to remove some of the noise. Comparing the pressure cell spectra to spectra measured on samples at atmospheric pressure gave a good idea about which ranges contained fine detail, such as sharp phonon modes, and which were predominately long smooth curves. It was found that for samples of d_8-κ-$(ET)_2Cu[N(CN)_2]Br$ in this pressure cell that above about 3000 cm^{-1} there were no fine peaks which could be resolved. This allowed relatively aggressive filtering at this end of the range. Below the diamond absorption edge there are several sharp phonon peaks so only limited filtering was used (the spectra can be seen in Figures 6.7 to 6.11).

The smooth region in the spectrum between 1700 cm^{-1} and 2700 cm^{-1} is caused by removal of the diamond absorption from the spectrum. Comparison with ambient pressure reflectance data [70] showed that the method described in Chapter 2 is valid for this. Several small phonon modes are obscured but, as we are interested in the overall shape for fitting, this is acceptable.

It has been suggested that the "hump" seen in the middle of the spectrum is due to an interband transition [68] or polaron absorption [69]. The latter seems more likely

as the former cannot adequately explain the large amount of spectral weight at low ω [69]. The exact cause of this feature is not important for the initial work, but will be for the Extended Drude analysis.

It was discovered that sometimes, if the ruby chip shifted in the cell, it could sufficiently alter the path into the spectrometer that an incorrect pressure would be measured. Previous work (see Chapter 5 and [60]) showed that, at these ranges of pressures in these types of materials, the central C=C vibration mode and the C–S vibration mode of the BEDT-TTF molecule shift linearly with increasing pressure. While the exact rate of shift with pressure for this material is not known, any points which fall a considerable distance outside this linear relation are likely to be ones where the ruby chip has shifted by a large amount, and so can be removed from any further analysis. Figures 6.4 and 6.5 show the pressure dependence of the C=C and C–S phonon modes at 294 K.

At this temperature all the data points obey the expected linear relationship as the ruby has only been observed to shift upon cool down of the cell. This is probably due to a range of things including contraction of the cell parts and a decrease in size of the gasket pushing the ruby from its previous position. Table 6.1 shows that the fre-

Phonon Mode	b-axis cm^{-1} + % $kbar^{-1}$	c-axis cm^{-1} + % $kbar^{-1}$
C=C	1326 + 0.3	1268 + 0.5
C–S	888 + 0.1	883 + 0.1

Table 6.1: Positions and pressure shifts of studied phonon modes in d_8-κ-BEDT-$TTF_2Cu[N(CN)_2]Br$ at 294 K

quencies and shifts with pressure are identical, to within experimental errors, to those measured for d_8-κ-$(ET)_2Cu(SCN)_2$ (see chapter 5). However, not all temperatures gave such good results. At 200 K, Figure 6.6 shows that, while many of the points are clearly in the correct places, several indicate that the ruby has shifted leaving an uncertainty as to what the pressure actually is. In such cases, the suspicious spectra have been discarded. While it might be possible to use this data to correct the

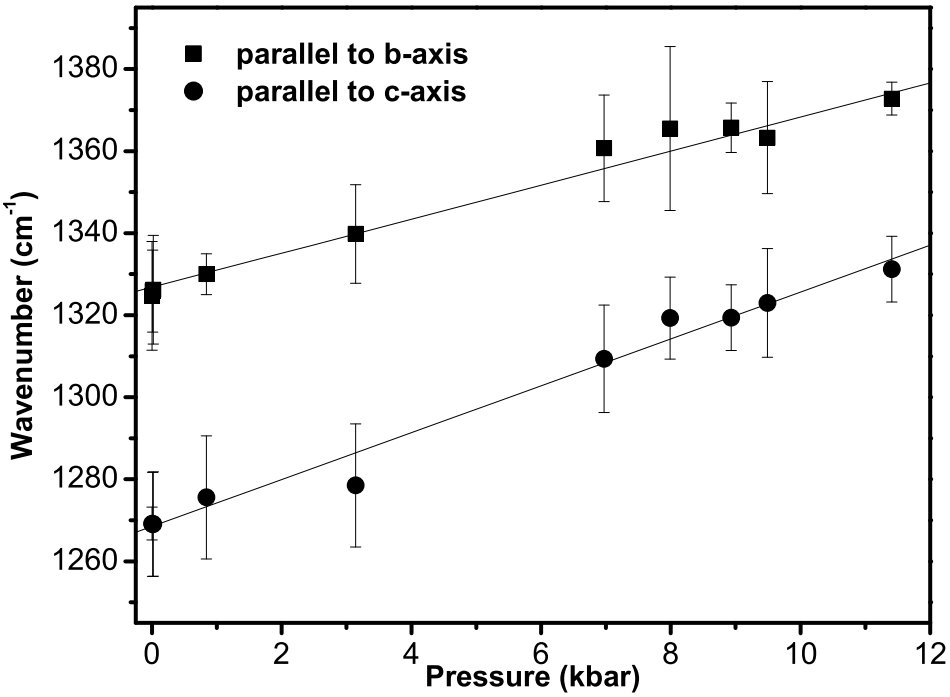

Figure 6.4: The pressure shift of the C=C vibration mode in d_8-κ-BEDT-$TTF_2Cu[N(CN)_2]Br$ at 294 K

erroneous pressure values, this has not been done here as it would introduce a large amount of further error into the values and there are sufficient data points without these values. All the remaining spectra will be investigated and their processed forms can be seen in Figures 6.7 to 6.11.

6.3.2 General overview of results

One of the first things to note is that the spectra have a noticeably different shape from spectra seen in the literature for d_8-κ-BEDT-$TTF_2Cu[N(CN)_2]Br$. This is because the samples are viewed through the surface of a diamond to which they are directly mounted. This means the spectrum we see is a sample-diamond one, rather than the usually reported sample-air or sample-vacuum spectra. This does not present any additional difficulty to analysis beyond allowing for the refractive index of diamond

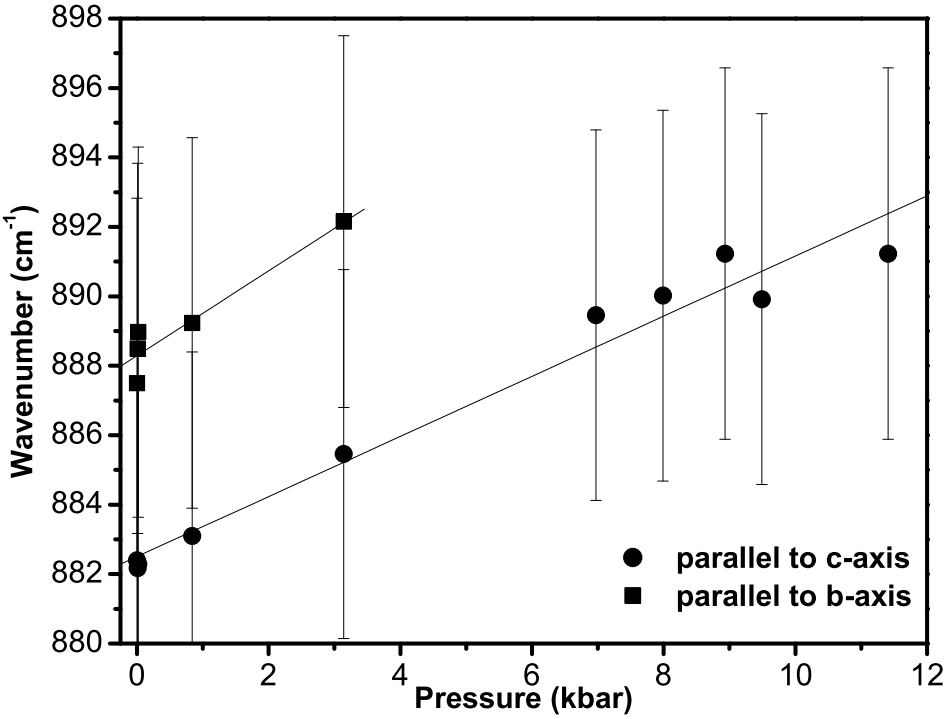

Figure 6.5: The pressure shift of the C-S vibration mode in d_8-κ-BEDT-$TTF_2Cu[N(CN)_2]Br$ at 294 K

in calculations, which can be taken as a constant in the range studied. Figure 6.12 shows modelled spectra under air and under diamond at room temperature, the only difference in the calculations being the refractive index of the diamond.

In general, we seen an enhancement of the low wavenumber reflectance as pressure increases for all temperatures, which is the region associated with intraband transitions. A dampening of the phonon modes due to the C=C and C–S vibrations is also observed with increasing pressure.

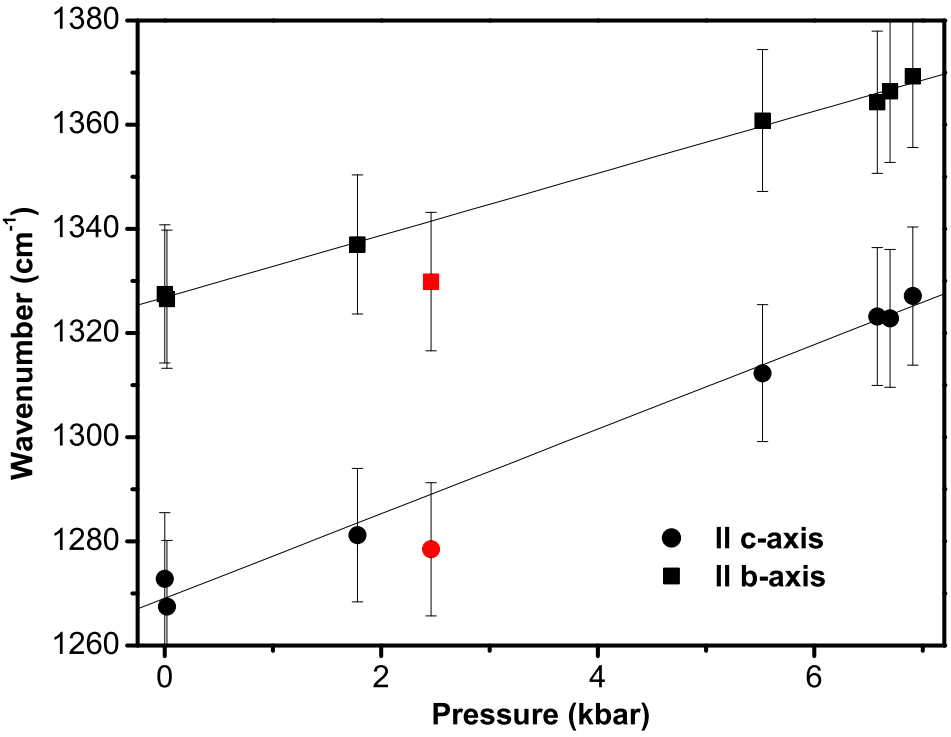

Figure 6.6: The pressure shift of the C=C vibration mode in d_8-κ-BEDT-$TTF_2Cu[N(CN)_2]Br$ at 200 K. Note the red point which does not fit with the rest of the data in either polarization. This is a point with an incorrect pressure reading, due to shifting of the ruby chip

6.3.3 Temperature and pressure dependence of phonon modes

While it was only possible to determine the pressure dependence of the C=C and C–S phonon modes for d_8-κ-$(ET)_2Cu(SCN)_2$ at room temperature in Chapter 5, now we have the opportunity to investigate both the temperature and pressure dependence for the similar compound d_8-κ-BEDT-$TTF_2Cu[N(CN)_2]Br$ (see Figures 6.7 to 6.11). Figure 6.13 shows how the frequencies of the modes shift with pressure at a range of temperatures. The C–S vibration appears to display a virtually constant pressure dependent shift, irrespective of temperature. While a slope is visible in the figure,

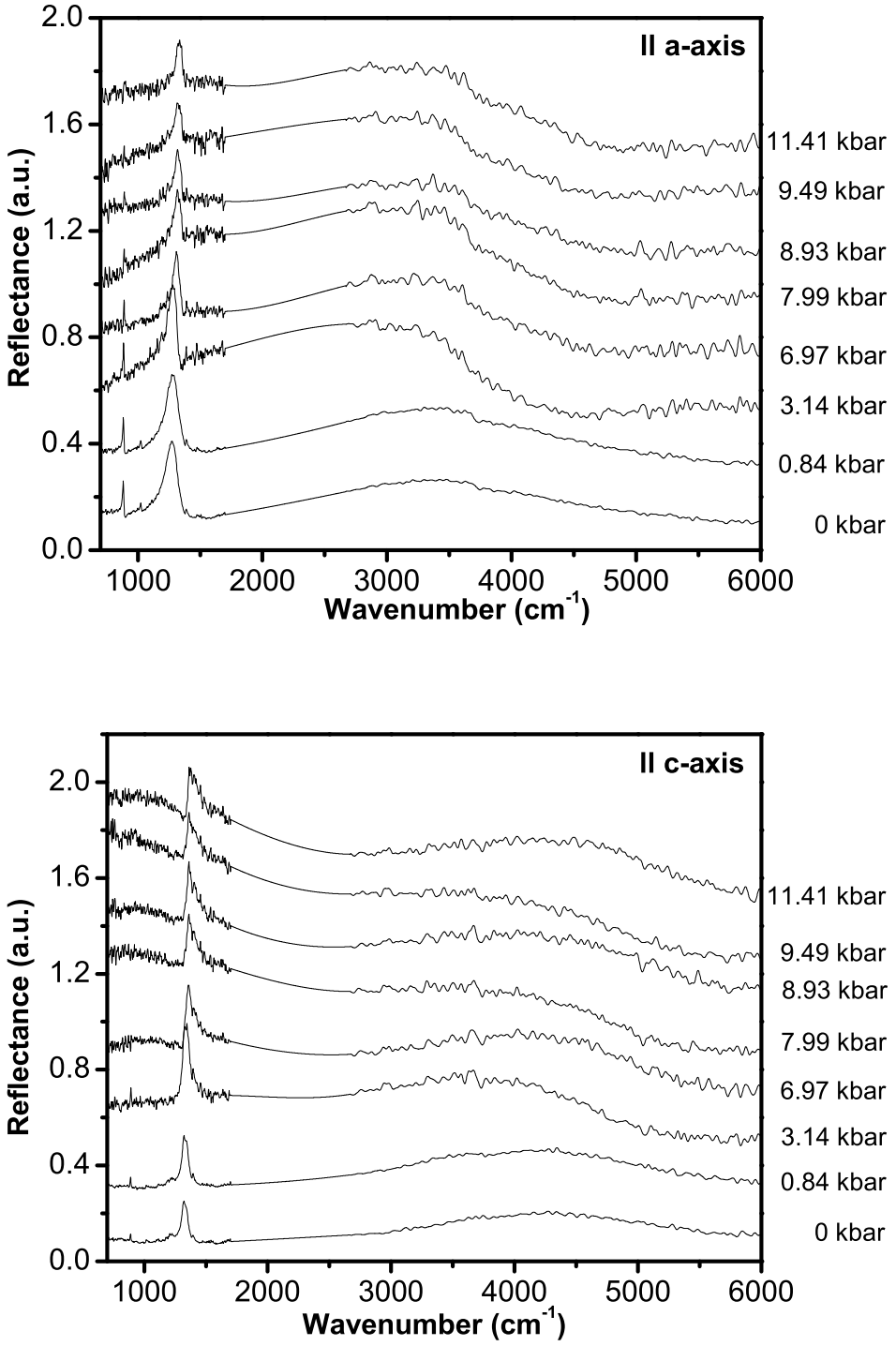

Figure 6.7: Polarized reflectance spectra for d_8-κ-BEDT-$TTF_2Cu[N(CN)_2]Br$ at at a range of pressures for 294 K. The upper graph shows spectra parallel to the a-axis and the lower parallel to the c-axis. Spectra have been offset for clarity

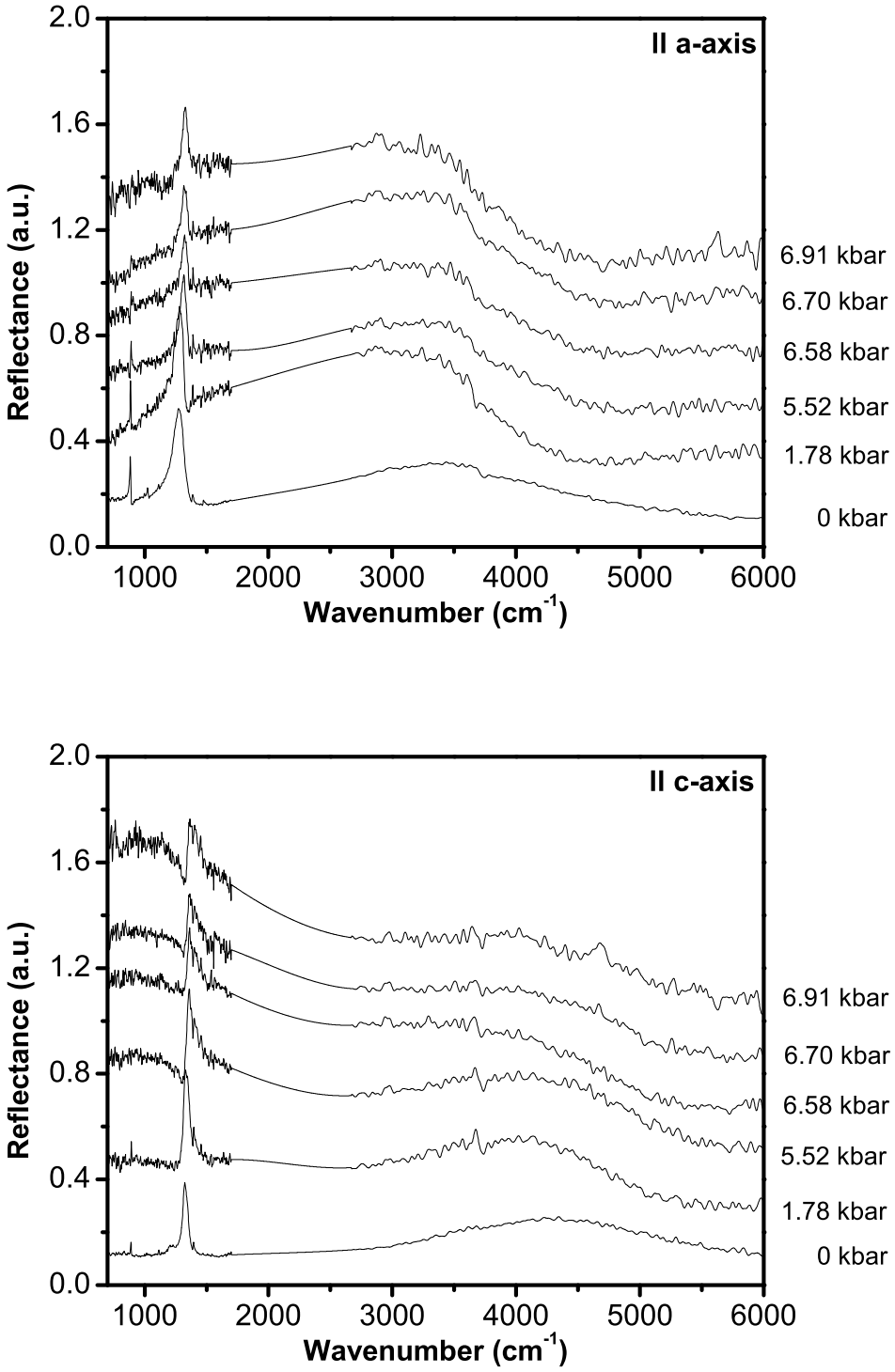

Figure 6.8: Polarized reflectance spectra for d_8-κ-BEDT-$TTF_2Cu[N(CN)_2]Br$ at at a range of pressures for 200 K. The upper graph shows spectra parallel to the a-axis and the lower parallel to the c-axis. Spectra have been offset for clarity

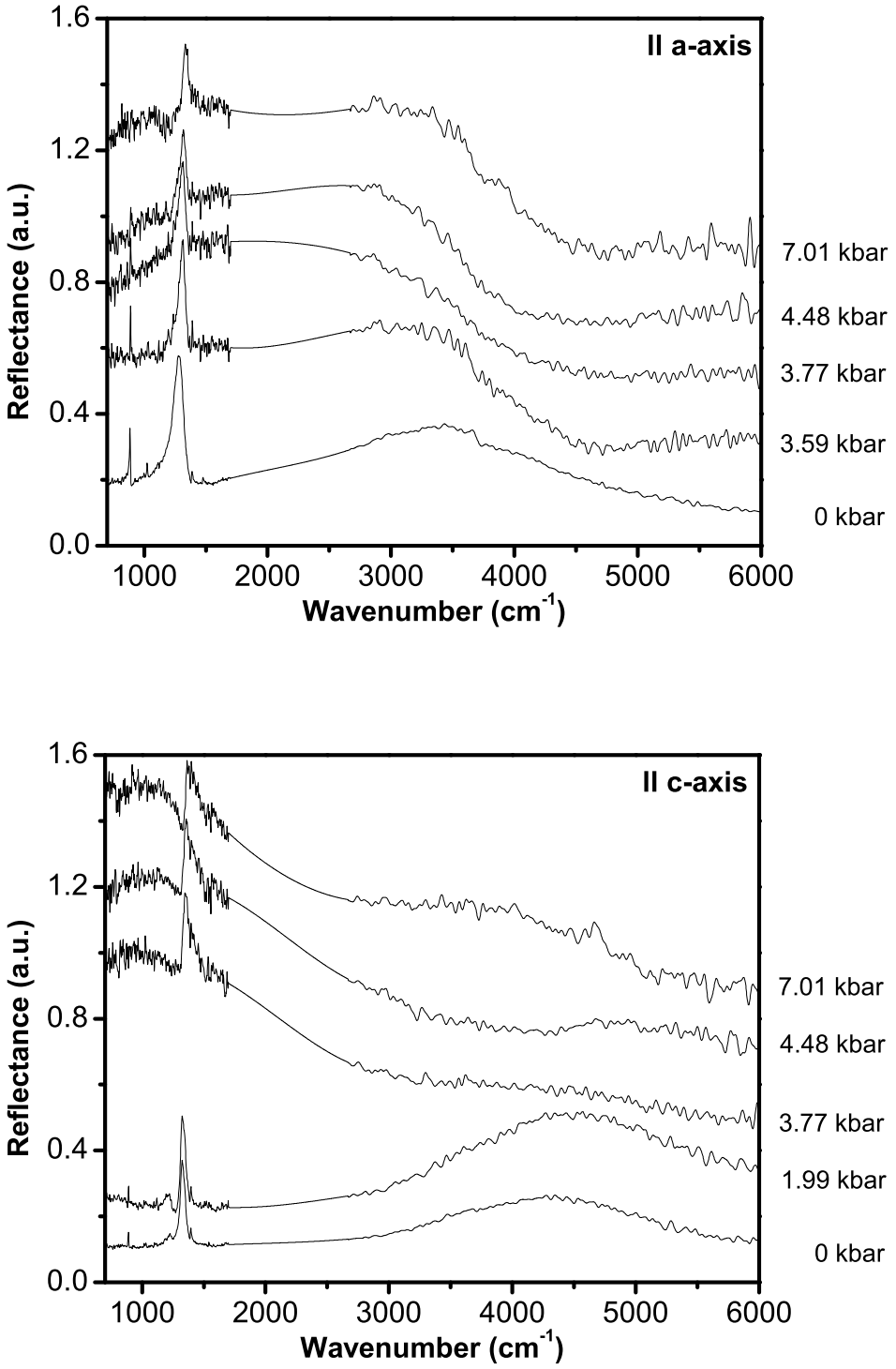

Figure 6.9: Polarized reflectance spectra for d_8-κ-BEDT-$TTF_2Cu[N(CN)_2]Br$ at at a range of pressures for 150 K. The upper graph shows spectra parallel to the a-axis and the lower parallel to the c-axis. Spectra have been offset for clarity

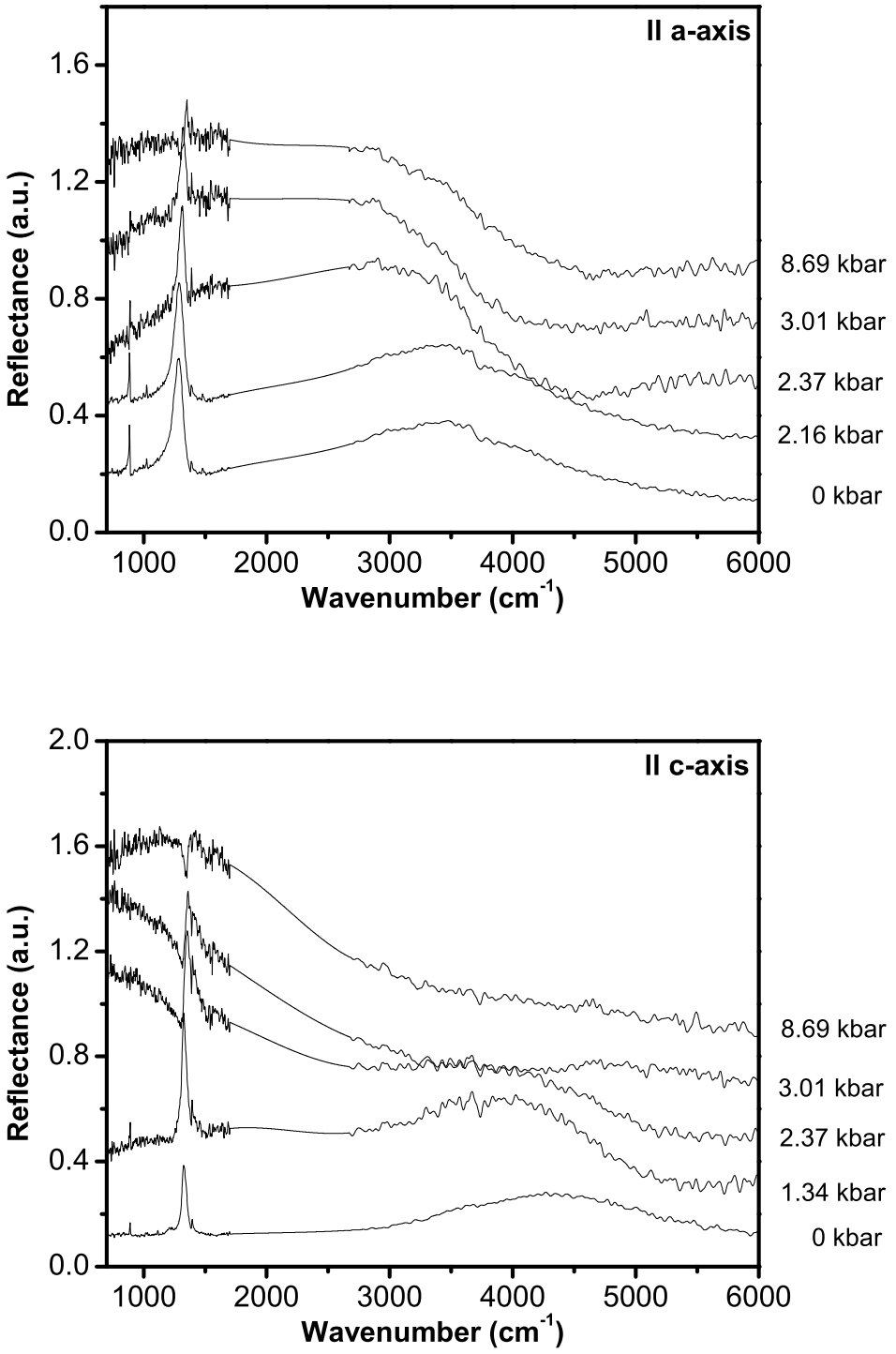

Figure 6.10: Polarized reflectance spectra for d_8-κ-BEDT-$TTF_2Cu[N(CN)_2]Br$ at at a range of pressures for 100 K. The upper graph shows spectra parallel to the a-axis and the lower parallel to the c-axis. Spectra have been offset for clarity

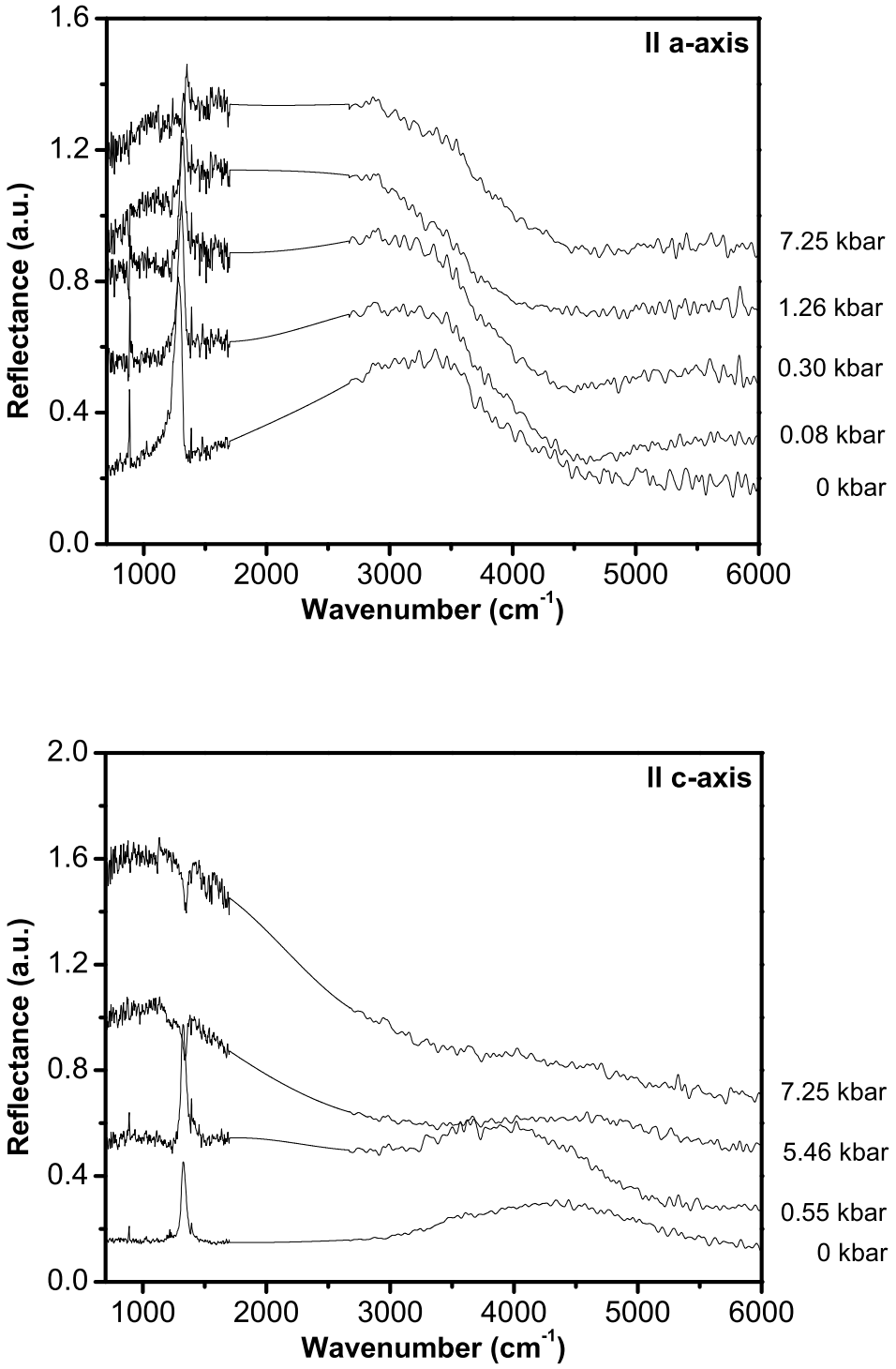

Figure 6.11: Polarized reflectance spectra for d_8-κ-BEDT-$TTF_2Cu[N(CN)_2]Br$ at at a range of pressures for 50 K. The upper graph shows spectra parallel to the a-axis and the lower parallel to the c-axis. Spectra have been offset for clarity

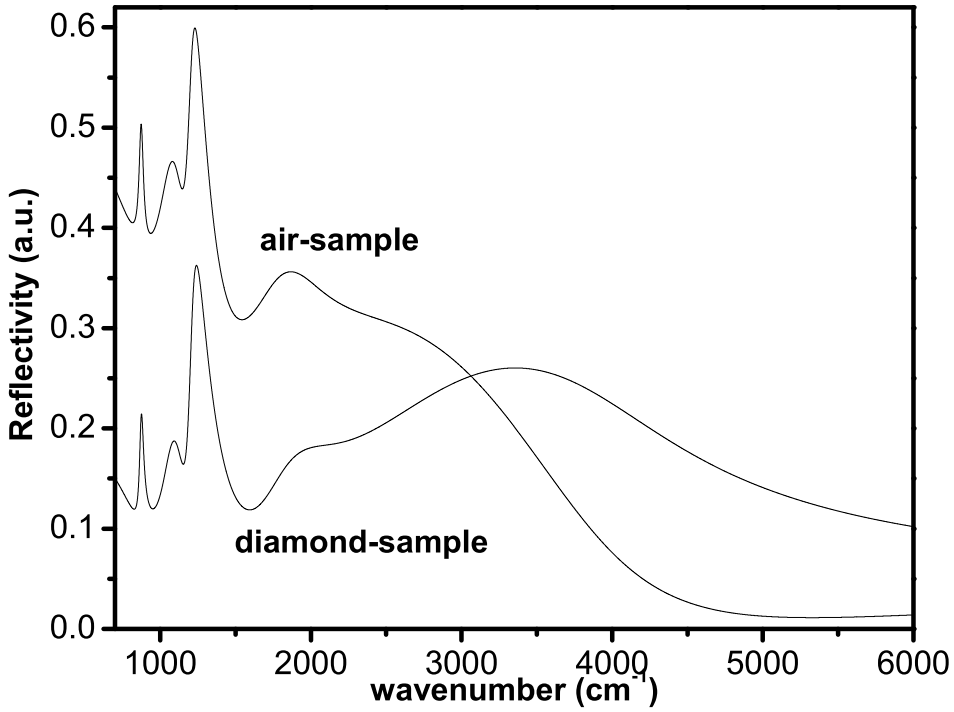

Figure 6.12: Diamond-sample and air-sample modelled reflectivities for d_8-κ-BEDT-$TTF_2Cu[N(CN)_2]Br$ at 294 K and ambient pressure

this is smaller than the uncertainties in the measurement; the damping of the phonon modes with increasing pressure meant that the pressure dependence could only be determined at comparatively low pressure for most temperatures. The C=C mode, on the other hand, displays a clear change in pressure dependence with temperature. The pressure and temperature dependencies of these modes are summarized in table 6.2. The C=C mode is a fully symmetric A_g mode [64] so it can only be observed in the infrared due to electron-phonon interactions whereas the C–S mode is anti-symmetric and can normally be seen in the IR. This suggests that the temperature dependence seen is due to temperature dependent changes in the electron-phonon interaction as we see no similar change in the C–S mode.

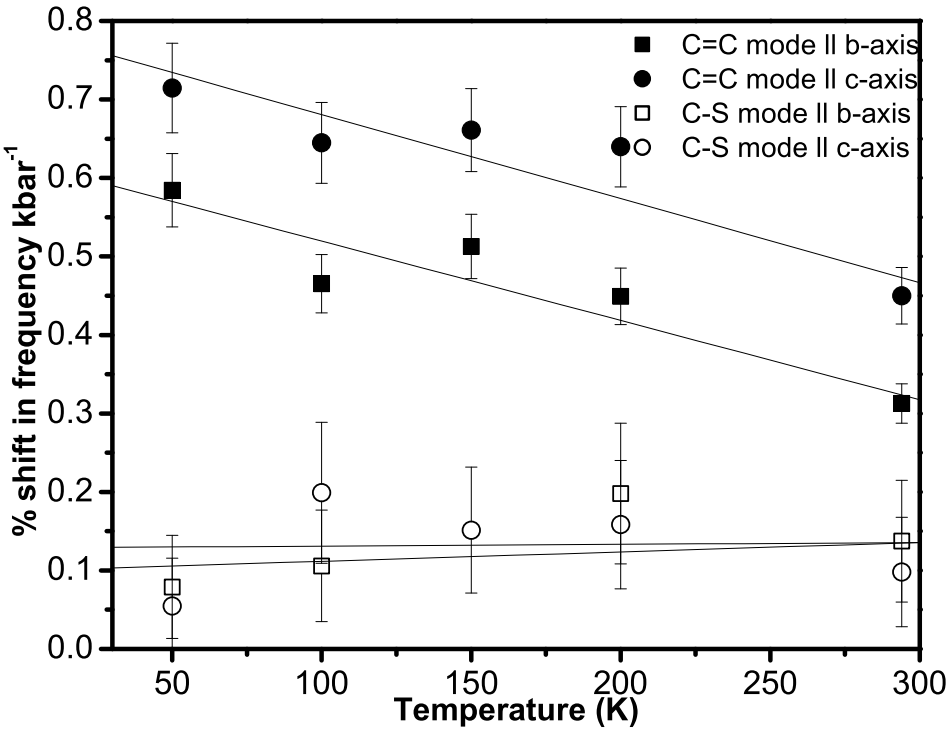

Figure 6.13: The shift in frequency with pressure for the central C=C and C–S vibration modes for d_8-κ-BEDT-$TTF_2Cu[N(CN)_2]Br$ as a function of temperature for both the b- and c-axes.

6.3.4 The extended Drude model

We shall now consider the extended Drude model, giving the frequency dependent scattering rate and effective mass. In the first instance this is obtained from the reflectance data by using a Kramers-Kronig transformation, giving access to the conductivity. From here a sum rule can be used to find the plasma frequency which is needed for the model. Unfortunately, to use a Kramers-Kronig transformation, knowledge of the reflectance over all frequency is needed. As the measurements were only performed over a finite range the function is extrapolated down to 0 cm^{-1} and up to 20,000 cm^{-1} for the purposes of the integration. The low frequency part was created using a Drude-Lorentz fit to the data in the measured range which was then extended

Phonon Mode	b-axis cm^{-1} + % $kbar^{-1}$ + $\%(100\ K)^{-1}$	c-axis cm^{-1} + % $kbar^{-1}$ + $\%(100\ K)^{-1}$
C=C	1326 + 0.3 - 0.1	1268 + 0.5 - 0.1
C–S	888 + 0.1 + (0)	883 + 0.1 + (0)

Table 6.2: Positions and pressure shifts of studied phonon modes in d_8-κ-BEDT-$TTF_2Cu[N(CN)_2]Br$

back to zero. The high frequency part was assumed to be flat from the end of the measured data until near the end of the extrapolated range, where it was allowed to decay to zero as ω^{-2}, as this helps convergence of the integral to a real value. This gave a reasonably consistent value of the conductivity which was relatively insensitive to small changes in the extrapolated function. However, this method was designed for simple conductors which obey the Drude model, which is not a good model for this sample. In addition to the errors from this inaccurate extrapolation, the similarity of the refractive index of the sample and that of diamond causes a further problem. For an air-sample interface, the refractive index of air, N_A, is always smaller than that of the sample, N_S. However for a diamond-sample interface at high frequency $|N_{\mathrm{S}}| < |N_{\mathrm{D}}|$ i.e. the reflected wave will be in phase with the incident wave. At low frequency, $|N_{\mathrm{S}}| > |N_{\mathrm{D}}|$ and the reflected wave will be out of phase by $-\pi$ with the incident wave. At some point in between the moduli of the refractive indices match, corresponding to a shift of $-\frac{\pi}{2}$ upon reflection. This frequency, ω_β, is needed to accurately determine the phase inversion term in the Kramers-Kronig integral and it is unknown and dependent on pressure and temperature. A detailed discussion and solution to this problem can be found in [60] so only an overview will be given here. As both the extrapolation and phase inversion term contribute a slowly varying background to the calculated phase, both terms can be compensated for using a single term, ω'_β, which replaces ω_β. We want a value of ω'_β such that we can calculate the correct phase over the measured reflectance range. Algorithms which guess a value of ω'_β, calculate n_s and then refine the value of ω'_β are not convergent so a different approach is needed. As the Drude-Lorentz model is a good fit over most of the mea-

sured range, including the frequency ω'_β, we can choose a value such that the value of the complex refractive index calculated using Kramers-Kronig matches that calculated from the model function. The further the shape of the spectrum deviates from the Drude-Lorentz model, the less appropriate this approximation becomes and any fits that return a value for ω'_β outside the measured range cannot be relied upon.

The conductivity of the room temperature spectra using this technique can be seen in Figure 6.14. These show good agreement with published ambient pressure spectra [71] and increasing pressure shows a similar effect to decreasing temperature for both polarizations, mainly an increase at low wavenumber due to intraband transitions. These spectra are also qualitatively similar to pressure work on h_8-κ-$(ET)_2Cu(SCN)_2$ [60].

However, we also have access to the conductivity at low temperature (see Figure 6.15). Once again we see an increase in conductivity at low wavenumber with increasing pressure and see larger conductivity for the measurement parallel to the c-axis. However now we see much greater enhancement with pressure for both axes. This is to be expected if we consider the phase diagram, as this material is an insulator at room temperature and pressure, but both decreasing the temperature and increasing the pressure bring it closer to a metallic state. A pressure increase at lower temperature has greater effect because there it is already much closer to the metal-insulator boundary. This process has been repeated for all temperature and pressure points as it enables an estimate of the plasma frequency to be made from a sum rule, this is needed to calculate the form of the extended Drude model.

The simple Drude model ignores electron correlations, which play a very significant part in the properties of these organic molecular materials. It does not work well when used on many conducting systems, including the high T_c superconductors [73] and ferromagnetic systems [23]. For these materials the extended Drude model, discussed in Chapter 2, has been used quite successfully.

For the extended Drude model to be used, we need to know both the reflectivity and phase. It is only possible to measure the reflectivity, but the phase can be calculated

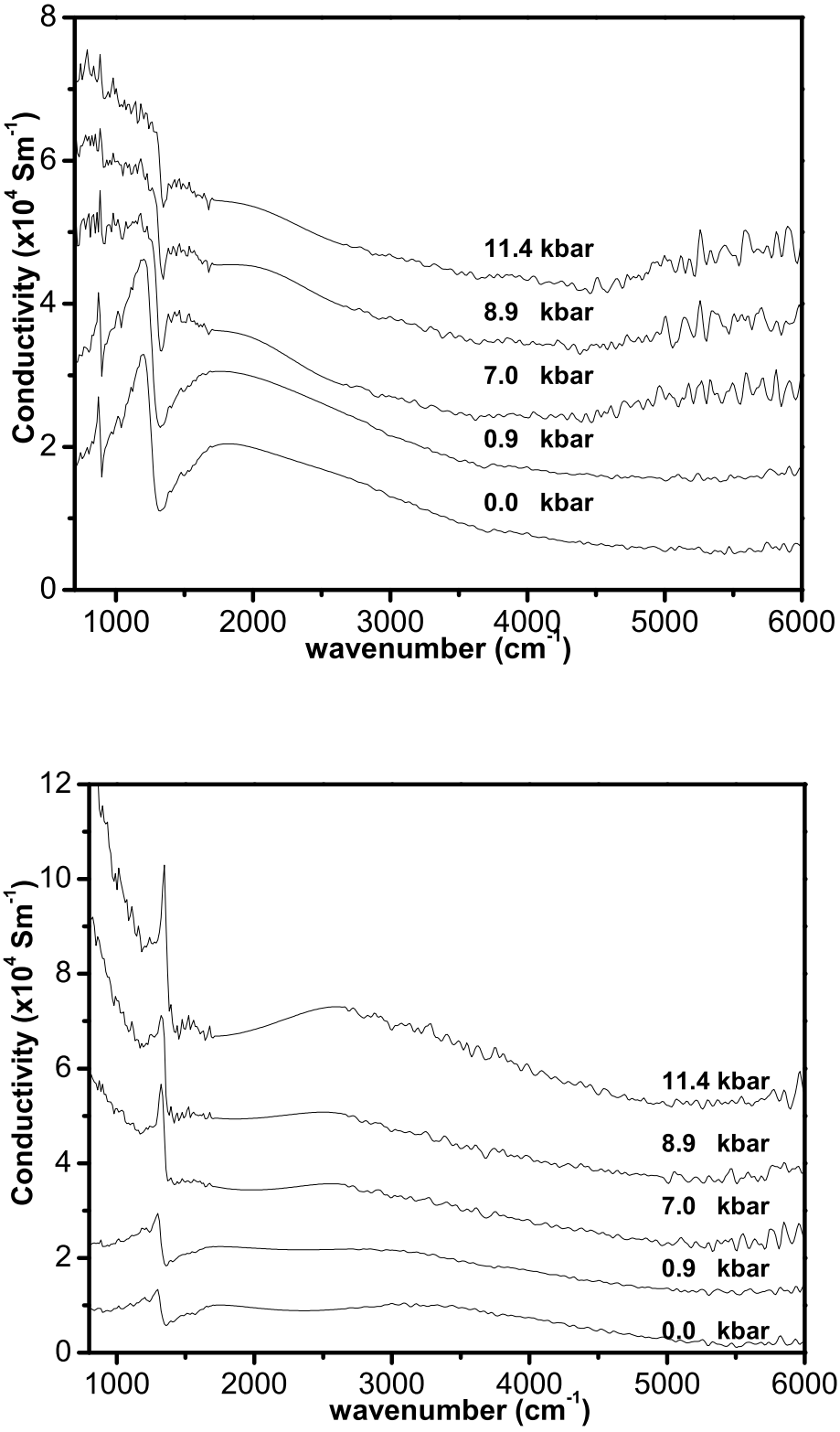

Figure 6.14: Optical conductivity of d_8-κ-BEDT-$TTF_2Cu[N(CN)_2]Br$ at 294 K, $\|$ to a-axis (top) and $\|$ to c-axis (bottom), from a Kramers-Kronig transformation. Spectra have been offset for clarity.

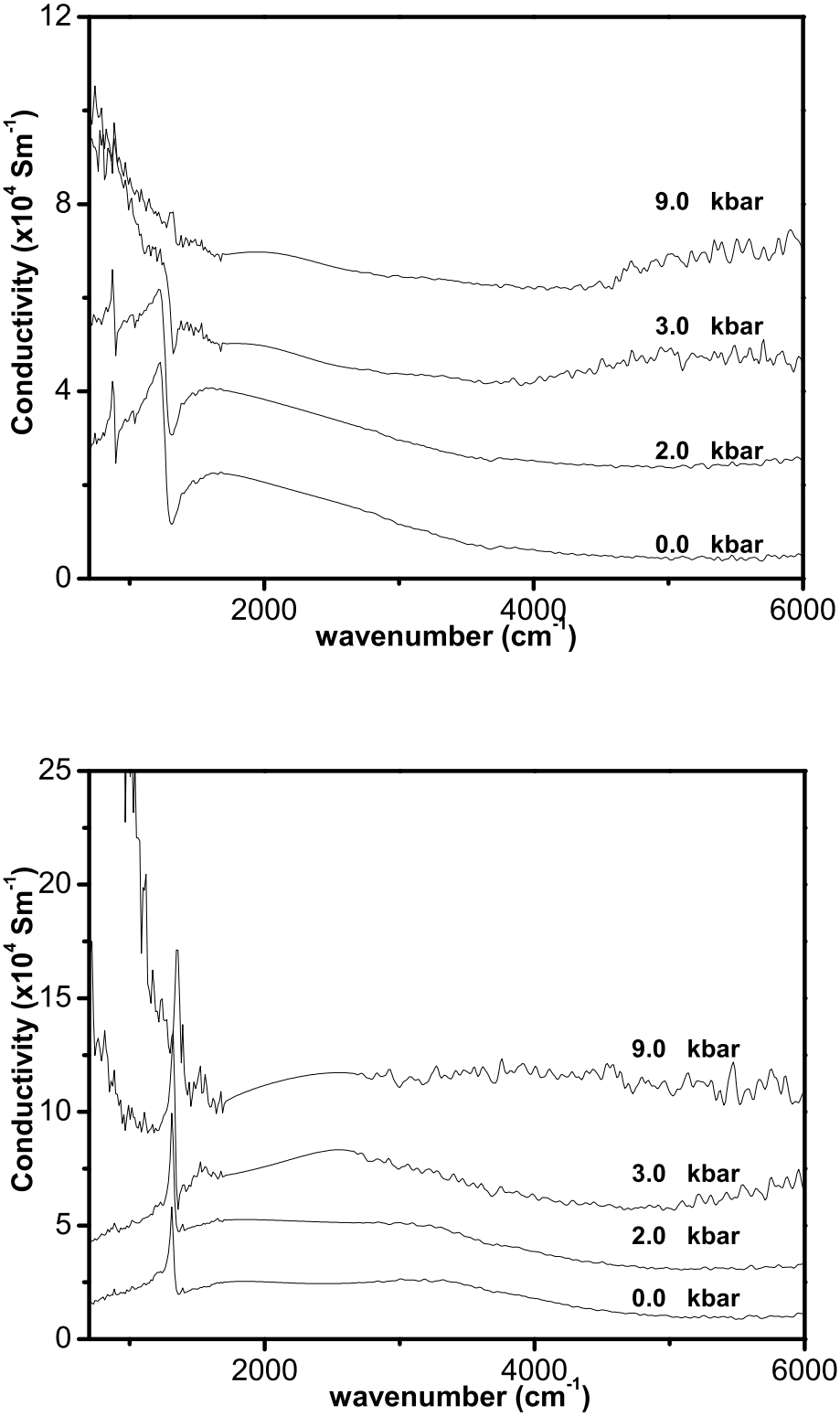

Figure 6.15: Optical conductivity of d_8-κ-BEDT-$TTF_2Cu[N(CN)_2]Br$ at 100 K, $\|$ to a-axis (top) and $\|$ to c-axis (bottom), from a Kramers-Kronig transformation. Spectra have been offset for clarity.

from this using the Kramers-Kronig relations (see Chapter 2), if the value of the reflectivity is known over all frequency. As these experiments were only performed over a relatively small frequency range, this could introduce reasonably large errors into the phase. In addition, the phonon modes at low wavenumber are difficult to remove exactly with a fitted oscillator. This technique was tried initially and, although the conductivity derived agreed broadly with the literature at ambient pressure [67], the removal of the phonon peaks was incomplete at best, and at worst introduced some significant errors. Figure 6.16 shows the conductivity (calculated from a Kramers-Kronig analysis), oscillator fit to the conductivity and the difference between the two. There are significant deviations between the two and this carries through into any subtraction of just the phonon modes. It is also much more difficult to write a fitting routine which will accurately fit oscillators to both real and complex parts. Such an approach is necessary due to the large number of spectra and to prevent any introduction of human bias.

As this method gave unsatisfactory results, a second approach was tried in which the reflectivity spectrum was fitted directly using a series of oscillators (see Figure 6.17). The imaginary parts of these oscillators gave the phase. This removed the problem of poor fitting to the phonon modes, which could result in large "spikes" in the spectrum after subtraction, as they were each now represented by a single oscillator, which could be easily turned off. This model consisted of two oscillators fitting the broad hump feature in the middle of the spectrum, one to give shape at low wavenumber and three to fit the phonon modes below 1500 cm^{-1}.

Data below 800 cm^{-1} have not been used in the results as the data cut off at 700 cm^{-1}. The low frequency oscillator was found to have an unpredictable effect on the modelled spectra in this range due to it extending outside the range of the data.

A high wavenumber cut-off of 3500 cm^{-1} is used for all the extended Drude modelling because the spectra are seen to vary in a non-predictable manner at higher wavenumber. This is caused by the presence (or absence) of a small gap, between the sample and the diamond surface, which is of the order of the wavelength used

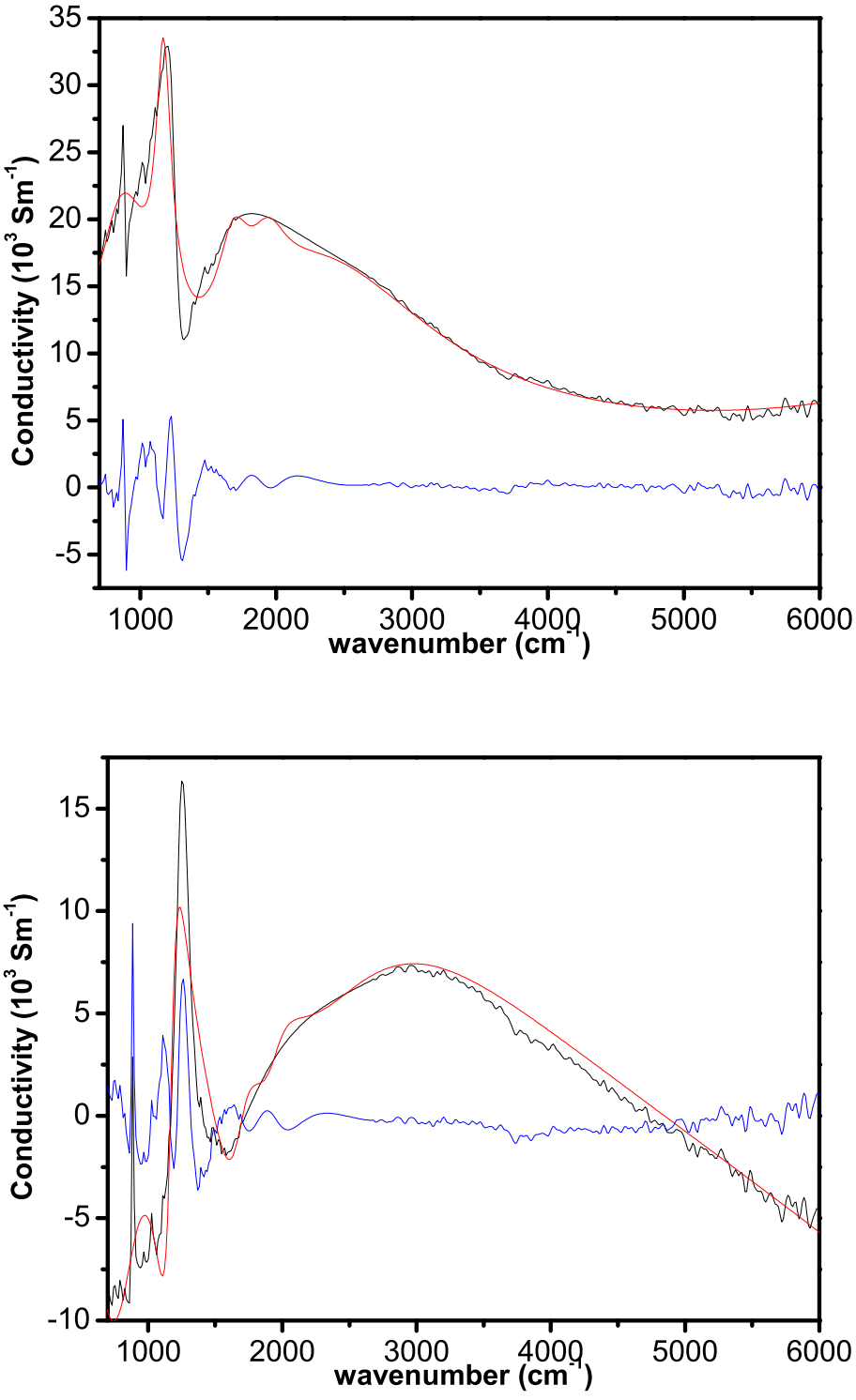

Figure 6.16: Optical conductivity of d_8-κ-BEDT-$TTF_2Cu[N(CN)_2]Br$ at 294 K and ambient pressure $\parallel$ to a-axis showing real (top) and imaginary (bottom) components derived using a Kramers-Kronig transformation. The spectrum (black), a multiple oscillator fit to the spectrum (red) and the difference between the two (blue) are shown

at the higher energy end of the measured spectral range. This, in effect, acts as a broad interference fringe which modifies the shape of the spectra at high wavenumber. In some cases, cooling, warming or changing the pressure caused the gap to appear, probably due to the sample, diamond and pressure medium contracting at different rates. As the exact size of the gap is unknown it is not possible to remove this term so it was decided to exclude the affected range. The effect can be seen in spectra in Figures 6.7 to 6.11. In addition, the "feature" in the middle of the spectra cannot easily be fitted and removed.

The small ripples present in some areas of a few of the modelled spectra are due to subtraction of the phonon modes. Every effort has been made to reduce such effects, but eliminating them entirely has not been possible. They are not present in the Kramers-Kronig transform method initially attempted so it is reasonable to believe that they are not "real".

This oscillator model of the spectrum was then used in the subsequent calculations. A concern about this technique was that it might not accurately represent both parts of the conductivity accurately, but this was not found to be the case. Figure 6.18 shows a comparison of the conductivity from a Kramers-Kronig analysis and from a fitting of the reflectivity spectrum. Both methods show good agreement over most of the range, and it appears to give at least as good a fit as the oscillator fit to the conductivity. In addition, fitting was much simpler with less ambiguity as there was only one spectrum to fit. This allowed the frequency-dependent mass enhancement ratio, m^*/m, and renormalized scattering rate, γ^* to be calculated for the full range of temperatures and pressures measured. Figures 6.20 to 6.22 show their temperature dependence at a range of pressures. As it is not possible to predetermine the exact pressure that will be reached upon cooling, the data on each graph are from similar, but not exactly the same, pressures and this may be responsible for some of the small anomalies seen in the data. In addition, the "hooks" seen in some of the data at low wavenumber may be due to inexact fitting of the model to the data and errors arising from the subsequent subtraction of the phonon modes. For the most part, these do

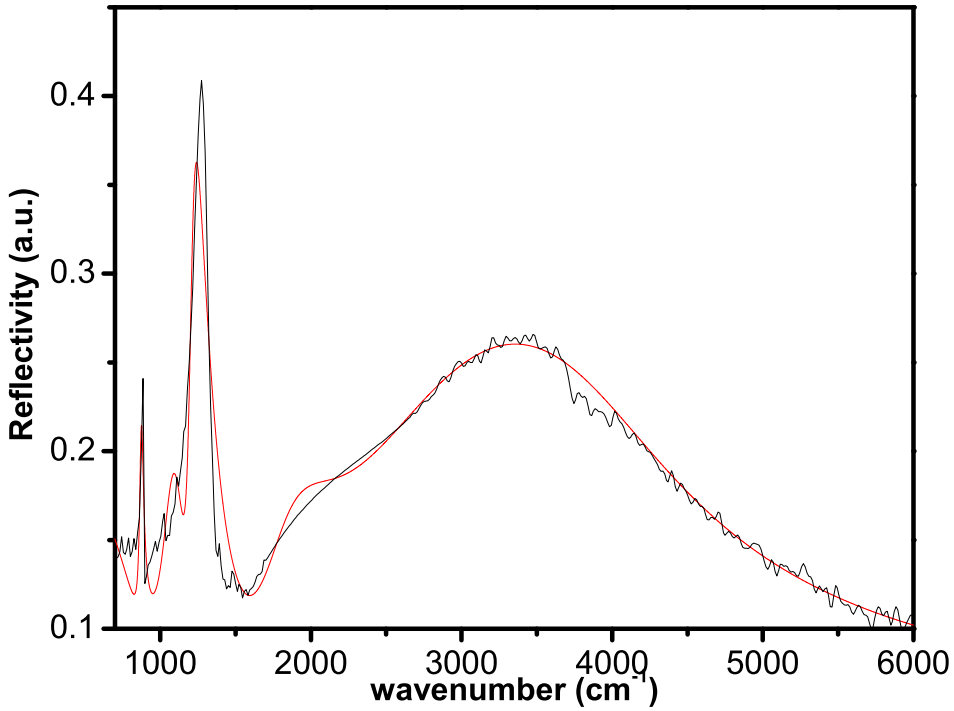

Figure 6.17: Reflectivity of d_8-κ-BEDT-$TTF_2Cu[N(CN)_2]Br$ at 294 K and ambient pressure || to a-axis (black) and an oscillator fit to the data (red)

not obscure the general form of the data.

We shall now consider the general trends of the data. At low temperatures and high pressures, γ^* increases monotonically with wavenumber and m^*/m increases at low wavenumber. This is typical of correlated metals such as the cuprates at above T_c [72] and it is in this region that we expect the metallic character of the sample. However, at high temperatures and low pressures we see the opposite behavior, with γ^* decreasing and m^*/m increasing with wavenumber. Changes like this are seen in both the superconductor $La_{2-x}Sr_xCuO_4$ [73] in its normal state, and the ferromagnet, $La_{1-x}Sr_xMnO_3$ [23], and in both cases indicate a crossover from coherent to incoherent transport. In these materials, it is caused by changes in temperature and doping rather than temperature and pressure. However we know that pressure has a similar effect on carrier concentration in the materials studied here as doping does in high-

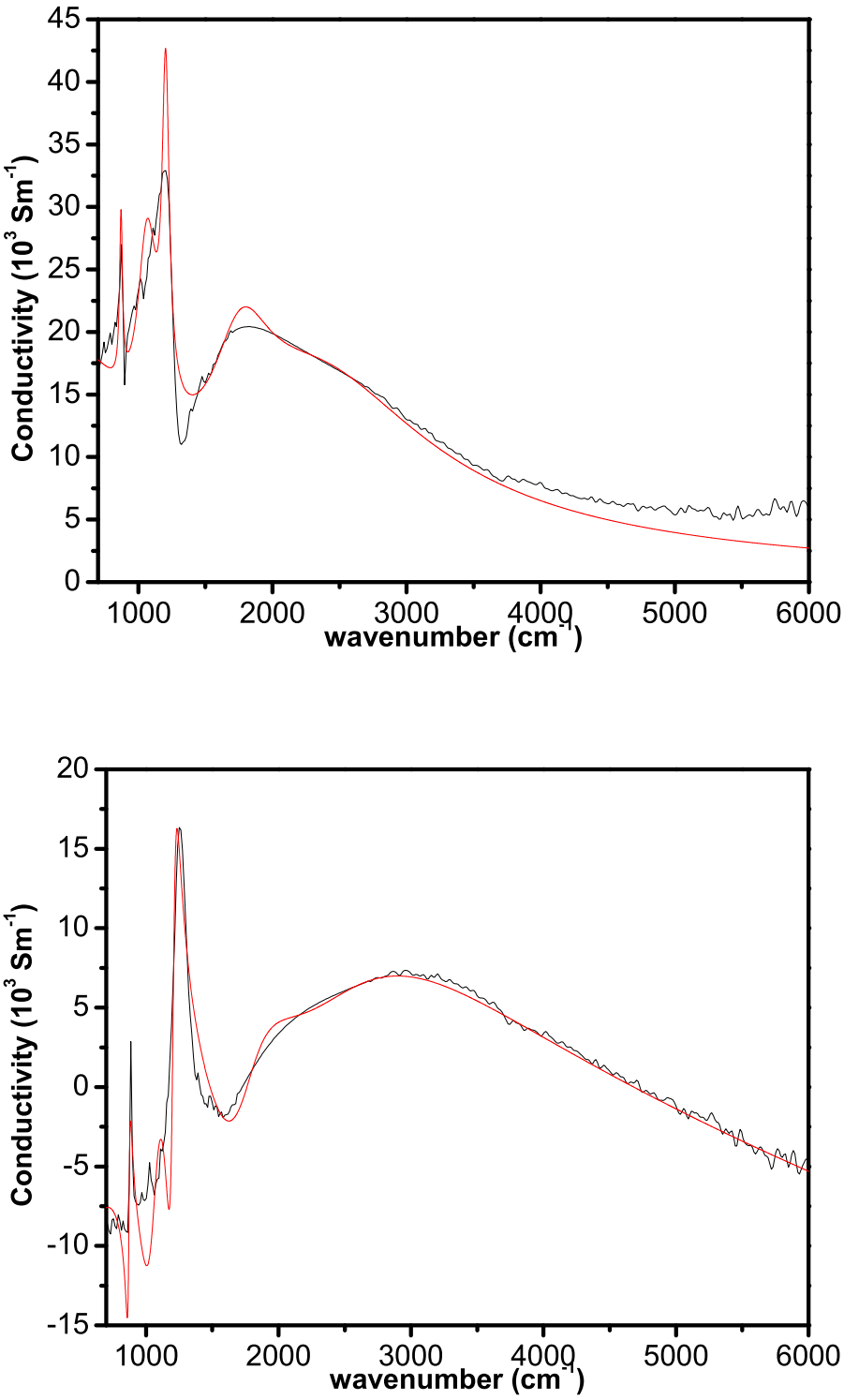

Figure 6.18: Optical conductivity of d_8-κ-BEDT-$TTF_2Cu[N(CN)_2]Br$ at 294 K and ambient pressure $\|$ to a-axis showing real (top) and imaginary (bottom) components derived using a Kramers-Kronig transformation (black). The conductivity from an oscillator fit to the reflectivity is also shown for comparison (red)

T_c superconductors (see Chapter 4). Figure 6.19 shows the properties of the latter compound to allow better comparison.

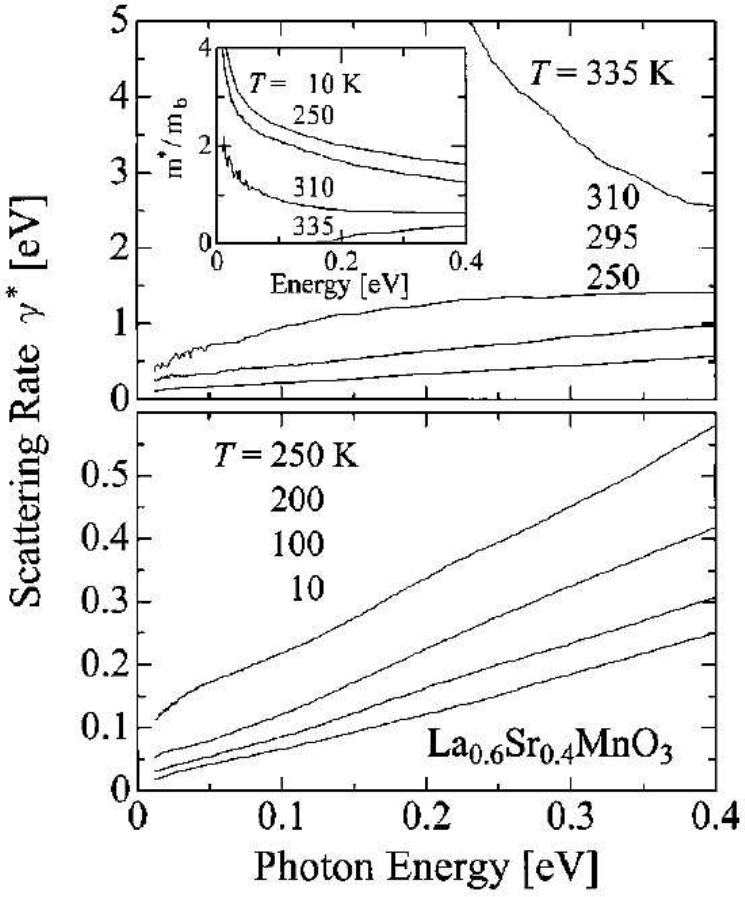

Figure 6.19: Frequency-dependent (renormalized) scattering rate γ^* and mass enhancement ratio m^*/m (inset) for $La_{0.6}Sr_{0.4}MnO_3$ calculated via an extended Drude analysis. Figure from [23]

These materials also exhibit the rather unusual phenomenon of a negative m^*/m at low wavenumber which we see in d_8-κ-BEDT-$TTF_2Cu[N(CN)_2]Br$. This is difficult to interpret under the Extended Drude model, but is generally associated with a low frequency conductivity which increases monotonically with frequency [18], something we see in this material. However, optical and transport properties should still be consistent. Theoretical models show that $\lambda(\omega)$ (nb: $m^*/m = 1 + \lambda(\omega)$) has the same sign as $\mathrm{d}\gamma^*/\mathrm{d}\omega$ and that $\mathrm{d}\gamma^*/\mathrm{d}\omega$ should have the same sign as $\mathrm{d}\rho/\mathrm{d}T$ where $\rho(T)$ is

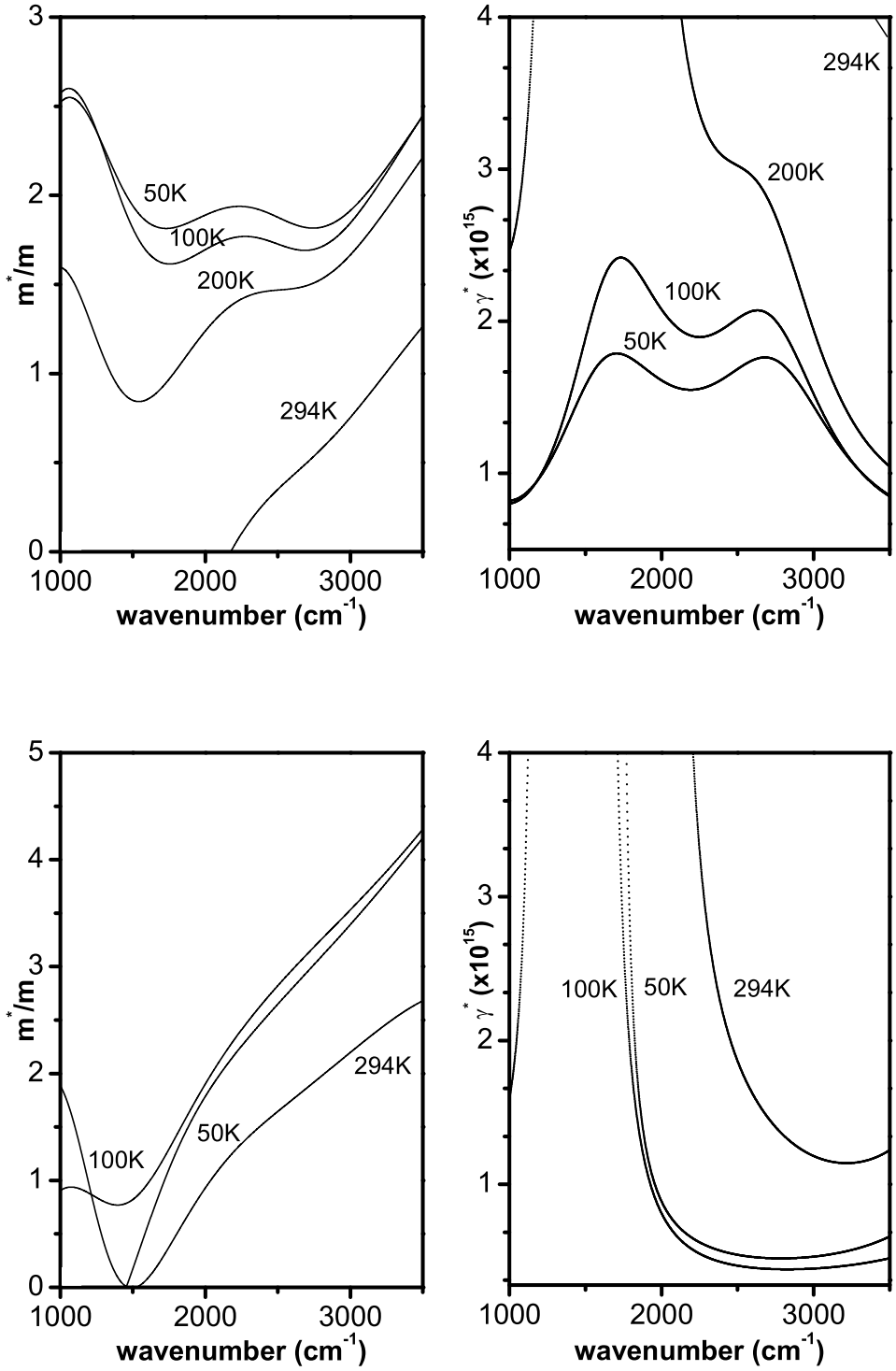

Figure 6.20: Frequency-dependent mass enhancement ratio m^*/m and (renormalized) scattering rate γ^* for d_8-κ-$(ET)_2Cu[N(CN)_2]Br$ at ambient pressure and $\|$ to the c-axis (top) and a-axis (bottom) of the crystal, calculated via an extended Drude analysis.

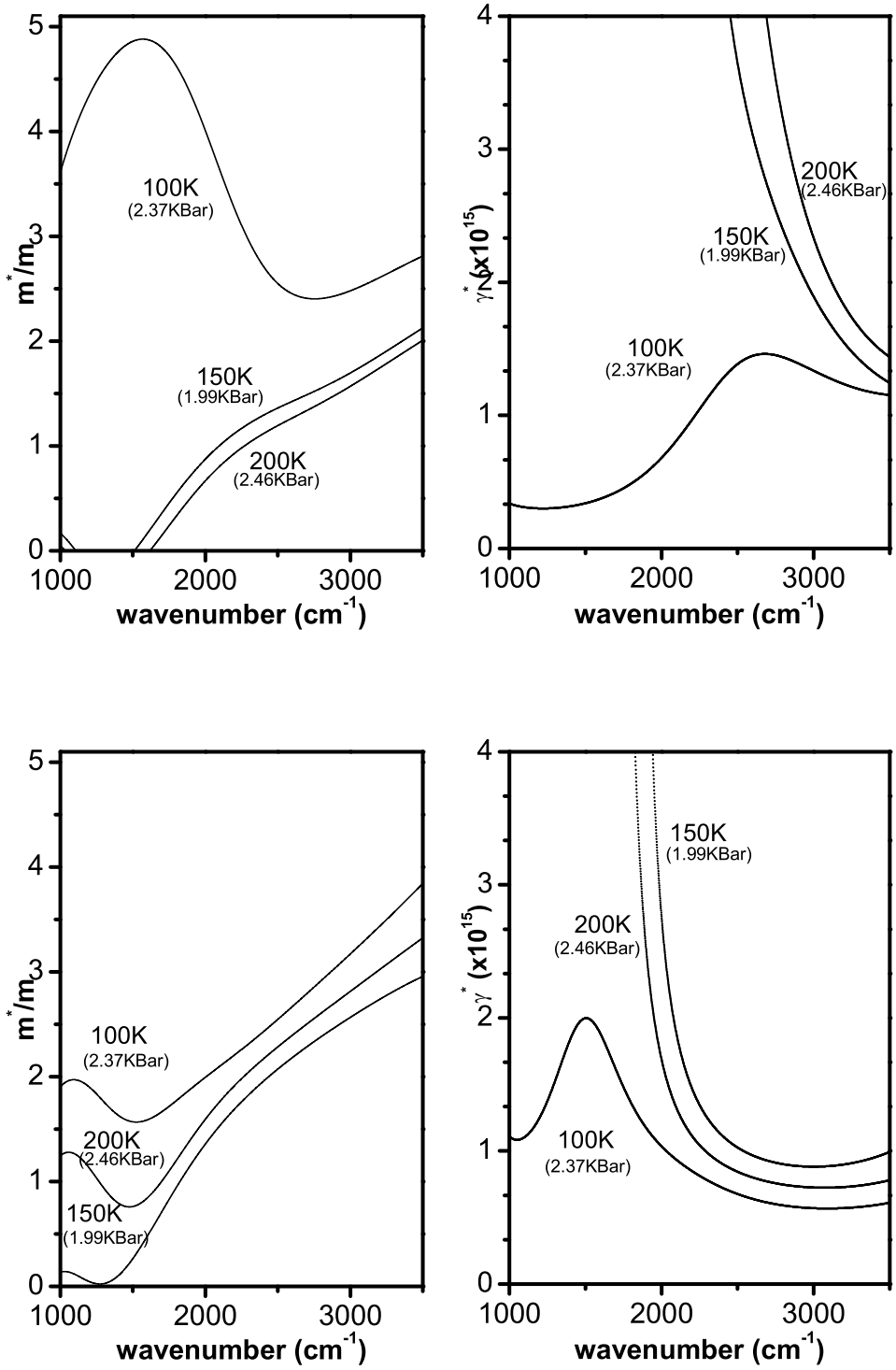

Figure 6.21: Frequency-dependent mass enhancement ratio m^*/m and (renormalized) scattering rate γ^* for d_8-κ-$(ET)_2Cu[N(CN)_2]Br$ at an average pressure of 2.3 ± 0.3 kbar and $\|$ to the c-axis (top) and a-axis (bottom) of the crystal

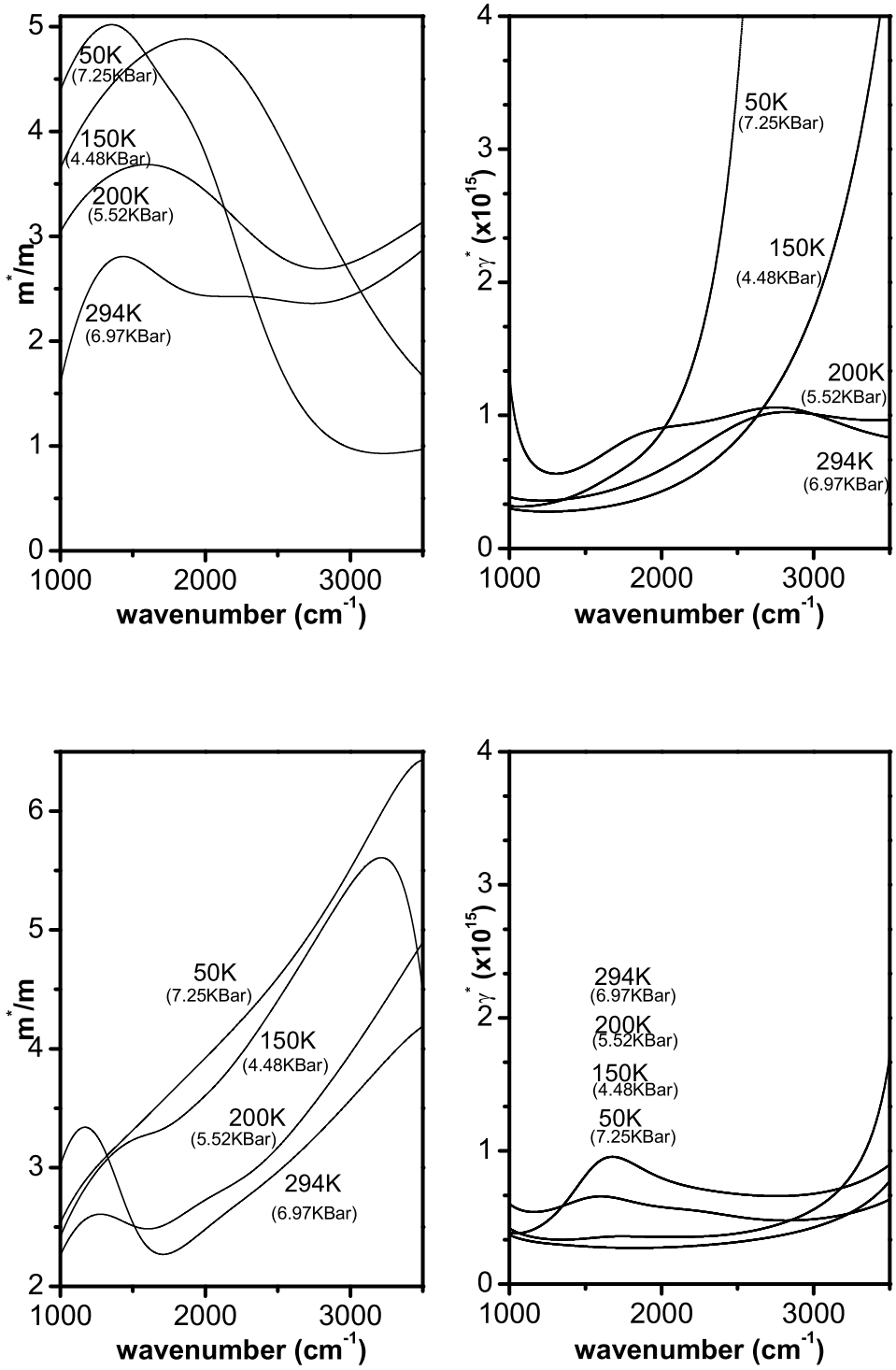

Figure 6.22: Frequency-dependent mass enhancement ratio m^*/m and (renormalized) scattering rate γ^* for d_8-κ-$(ET)_2Cu[N(CN)_2]Br$ an average pressure of 6.1 ± 1.6 kbar and $\|$ to the c-axis (top) and a-axis (bottom) of the crystal

the dc resisitivity [18]. h_8-κ-BEDT-TTF$_2$Cu[N(CN)$_2$]Br displays a maximum in $\rho(T)$ at $\sim$90 K [3], which tends to disappear under pressure. However deuteration shifts this to lower temperatures [70], the exact position being dependent on cooling rate. For high temperature and low pressure $\mathrm{d}\rho/\mathrm{d}T$ is negative and it is this region in which we see negative $\lambda(\omega)$ at low wavenumber. At high pressure and low temperature we see a positive value of $\mathrm{d}\rho/\mathrm{d}T$ and we have broad agreement as $\lambda(\omega)$ is positive for the spectra. This suggests that the Extended Drude model is still an acceptable fit, despite the behavior of m^*/m at low wavenumber.

No obvious discontinuity is seen in the scattering rate or mass enhancement ratio; the properties seem to slowly vary from non-metallic to metallic character. This would be expected if we are above the critical temperature for this material's Mott transition [74]. However it is possible that we do not have sufficient points in pressure-temperature space to detect any discontinuity.

Also of note is the difference in properties between the two polarizations. Measurements parallel to the c-axis show a greater degree of metallic character than those parallel to the a-axis. This is particularly noticeable in Figure 6.22 where we see metallic properties at lower temperatures parallel to the c-axis. However parallel to the a-axis it shows a mass enhancement ratio which is insulating in character. This is partially reflected in the conductivity (see Figure 6.15), but to a lesser extent.

6.4 Conclusion

The results from temperature and pressure dependent polarized infrared reflectivity measurements on the organic superconductor d_8-κ-(ET)$_2$Cu[N(CN)$_2$]Br have been presented. It is believed that these are the first such measurements on organic molecular materials and allow greater access to the whole of the pressure-temperature phase diagram than has previously been possible with optical measurements. These techniques are still in development and are not yet suitable for all materials (as seen in the difficulties with TMTSF$_2$PF$_6$). However it is an area which shows great promise and

is deserving of further research.

The effect of pressure and temperature on both symmetric and antisymmetric phonon modes has been investigated and it was found that the pressure dependence of C=C and C–S modes are virtually identical to that found in d_8-κ-$(ET)_2Cu(SCN)_2$. This is hardly surprising as d_8-κ-$(ET)_2Cu[N(CN)_2]Br$ displays many of the same properties as a sample of d_8-κ-$(ET)_2Cu(SCN)_2$ under pressure. However, a shift in position with temperature was only observed for the symmetric C=C mode, which can only be observed through electron-phonon interactions, and was independent of polarization. This suggests that the temperature shift gives a measure of the temperature dependence of electron-phonon interaction in this material.

The Extended Drude model has been used to analyze the data as it has been very effective for modelling the properties of high T_c superconducting compounds, and the simple Drude-Lorentz model is not a good fit– mainly due to the fact that these strongly correlated electron systems are not simple Drude metals. Results for this single sample agree with known properties of the system and suggest that this it would be worth investigating the applicability of the model to other organic molecular materials. In addition, m^*/m and γ^* show significant inplane anisotropy which would bear further investigation. The effects of temperature and doping on m^*/m and γ^* for high T_c materials is similar to that seen with temperature and pressure in d_8-κ-$(ET)_2Cu[N(CN)_2]Br$.

Appendix A

Preliminary investigations into $TMTSF_2PF_6$

A.1 Overview

$TMTSF_2PF_6$ was the first organic molecular material that was found to be a superconductor (It has a T_c of 1.1 K at 6.5 kbar) [3]. This salt is one of the Bechgaard salts, which were first synthesized by Bechgaard et al [75] and are of the form $TMTSF_2X$, where X^- is a monovalent anion. The TMTSF molecule can be seen in Figure A.1. $TMTSF_2PF_6$ is a charge transfer salt where each TMTSF molecule donates half an electron to the anion.

$TMTSF_2PF_6$ is a quasi-one-dimensional material, the overlap of π-orbitals is strongest along the a-direction. While there is some movement along the b-axis as well, the transfer integral is an order of magnitude smaller [3] (see Figure A.2). This is reflected in a variety of properties of the system, including the infrared reflectivity (see Figure A.3)

This material displays a range of interesting ground states, including one-dimensional Luttinger liquid, two-dimensional Fermi liquid and charge localized states, which are accessible through manipulation of temperature and pressure. It was hoped that these could be studied using the techniques in Chapter 6. However, the me-

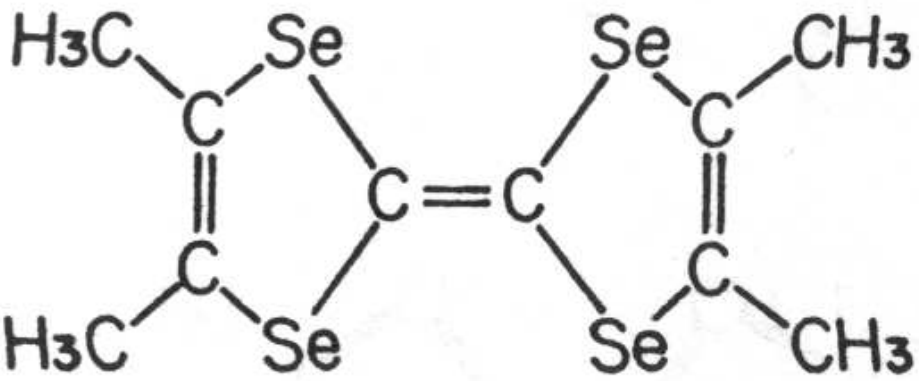

Figure A.1: Structure of the TMTSF molecule [3]

chanical twinning observed prevented high pressure measurements and so the ambient pressure results obtained are included in this appendix to aid anyone who is interested in continuing this work. An extended Drude analysis was also been applied to the resulting spectra.

A.2 Infrared reflectivity measurements

Figure A.3 shows the highly one-dimensional character of the sample measured at room temperature under air with nitrogen gas purging. Figure A.4 shows the temperature depedence of the spectra. Much lower noise is seen in the spectra than for d_8-κ-$(ET)_2Cu[N(CN)_2]Br$ studied in Chapter 6, for two reasons: firstly, the much stronger reflectance observed in this part of the spectrum gives a better signal to noise ratio and the samples of $TMTSF_2PF_6$ were much larger and with a better surface quality and measured under air. Similar filtering techniques to those used on d_8-κ-$(ET)_2Cu[N(CN)_2]Br$ have been used. These measurements were performed using the cryostat with a small cold finger described in Chapter 3 and were performed in air to give reference spectra to compare to the subsequent measurements in the pressure cell. They show that cooling has comparatively little effect on the b-axis

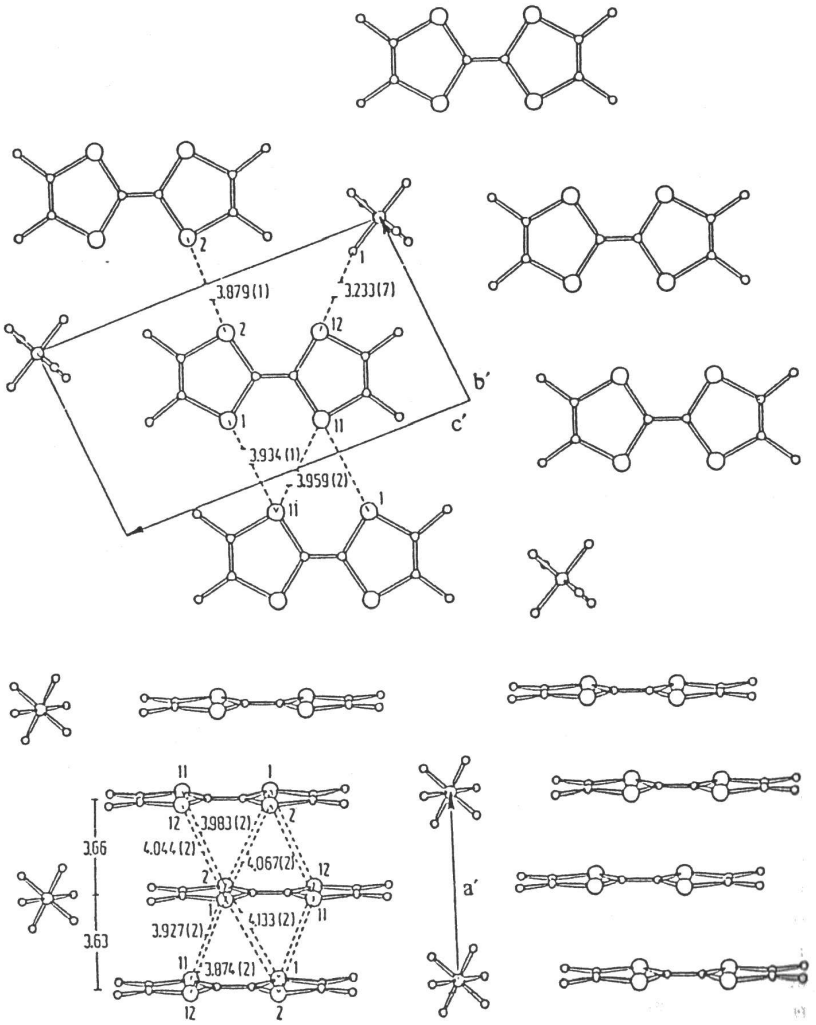

Figure A.2: Crystal structure of $TMTSF_2PF_6$. View along the a-direction (top) and side view of the stacks (tilted at 10°) (bottom) [3]

spectra over the range measured (it has a much larger effect in the far infrared) and that the reflectance is flat and near to zero. For this reason, initial Extended Drude calculations were only performed on the much more reflective a-axis. The ambient pressure polarized reflectance measurements carried out inside the pressure cell are shown in Figure A.5. These are much nosier, but the same trends are still seen. The difference in shapes is again due to the diamond-sample interface. Both polarizations show an increase in intensity at low wavenumber with decreasing temperature. This is particularly noticeable for the b-axis where a change from very little relfection to a

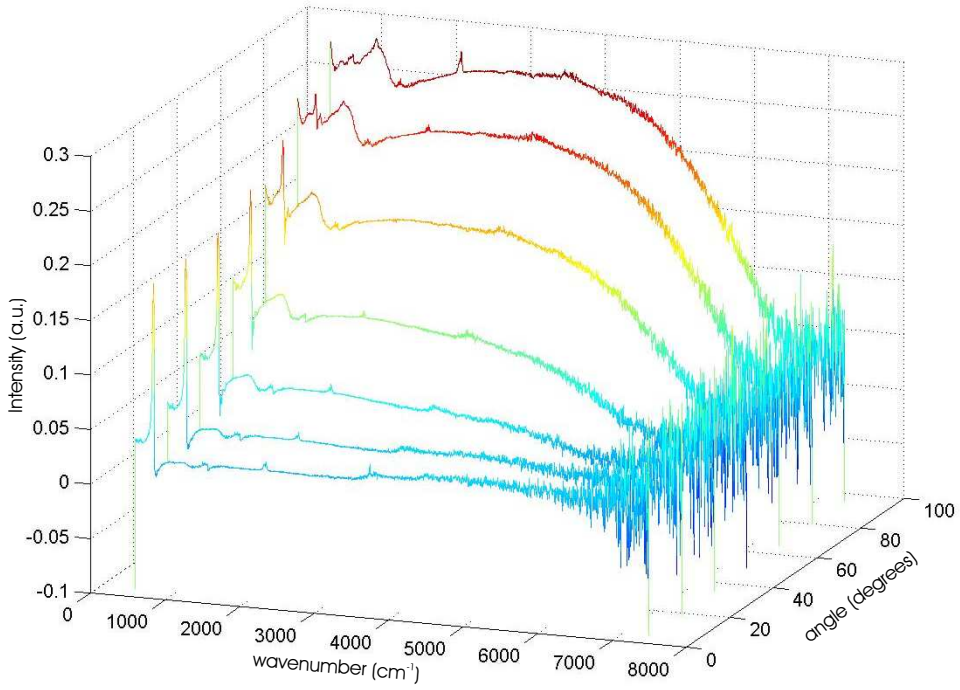

Figure A.3: Angle dependant infrared reflectance spectra of $TMTSF_2PF_6$ at room temperature. 0° corresponds to || b-axis and 90° corresponds to || a-axis

more Drude like spectrum is seen. The spectra are also seen to change shape between 150 K and 100 K. This corresponds to the temperature range in which $TMTSF_2PF_6$ changes from a one-dimensional Luttinger Liquid to a charge localized state [76].

A.3 Extended Drude Analysis

The techniques for fitting the Extended Drude model to this type of organic molecule were initially developed using the ambient pressure spectra under air of $TMTSF_2PF_6$. The model was also only used on the stronger a-axis. In this case, removal of the phonon modes was possible by fitting them and then subtracting, as can be seen in Figure A.7. This means that a Kramers-Kronig analysis was performed to get the phase rather than an oscillator fit to the reflectance. Overall, an increase in conductivity is

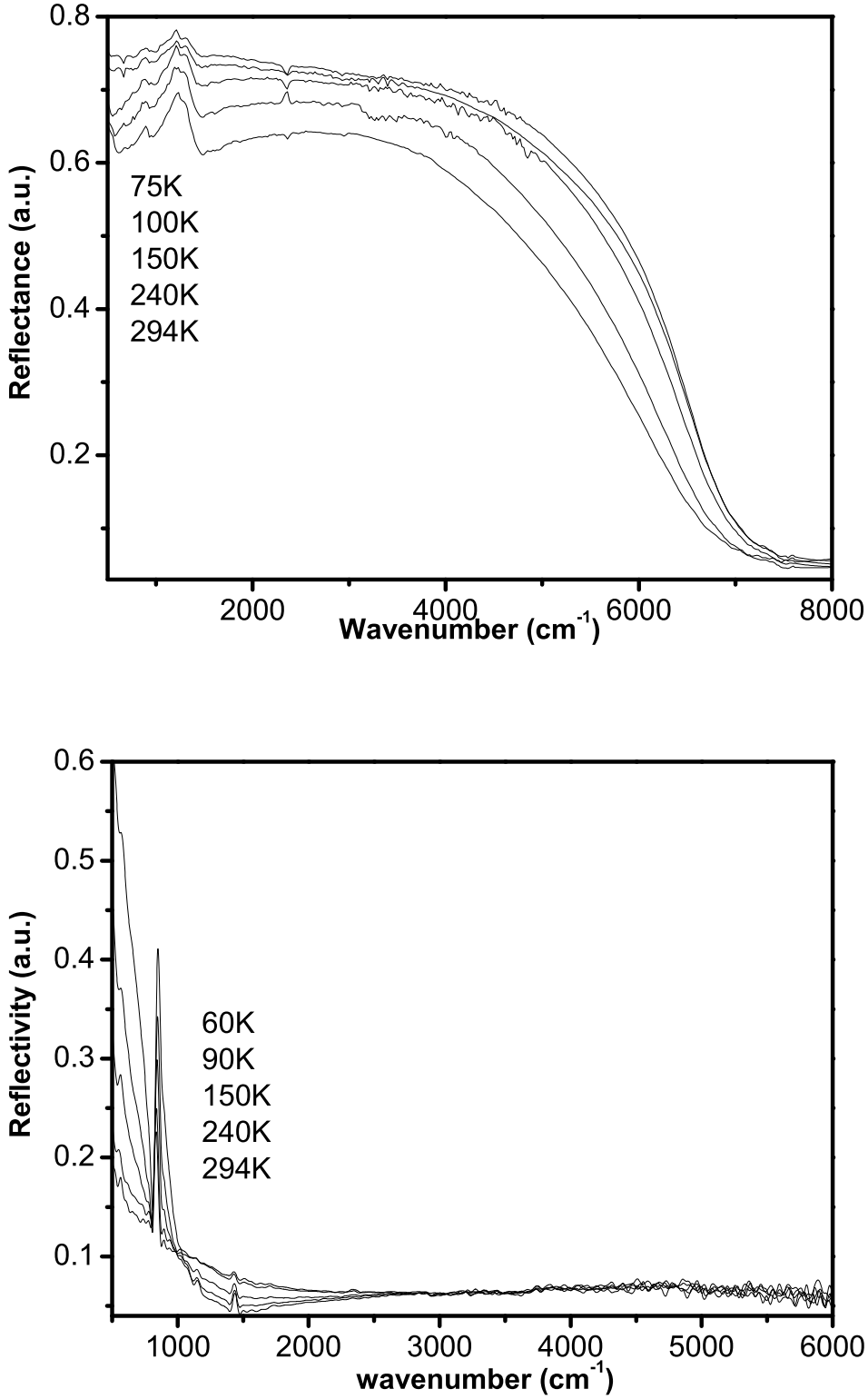

Figure A.4: Temperature dependent reflectance spectra of $TMTSF_2PF_6$ parallel to both a- (top) and b-axes (bottom) at ambient pressure measured under air

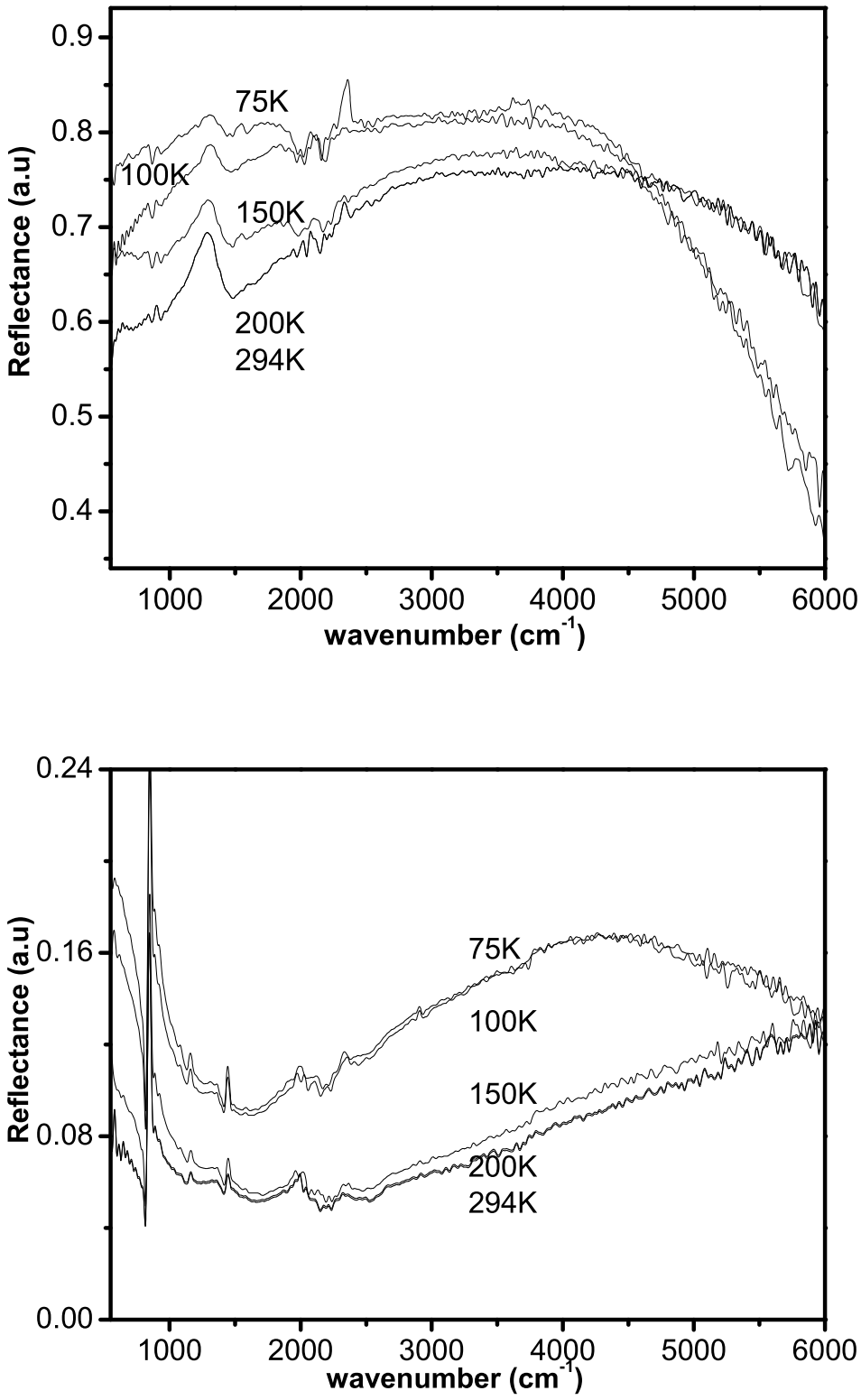

Figure A.5: Temperature dependent reflectance spectra of $TMTSF_2PF_6$ parallel to both a- (top) and b-axes (bottom) at ambient pressure measured under diamond

seem as temperature decreases, with a noticeable change between 125 K and 100 K, as seen in the reflectance spectra.

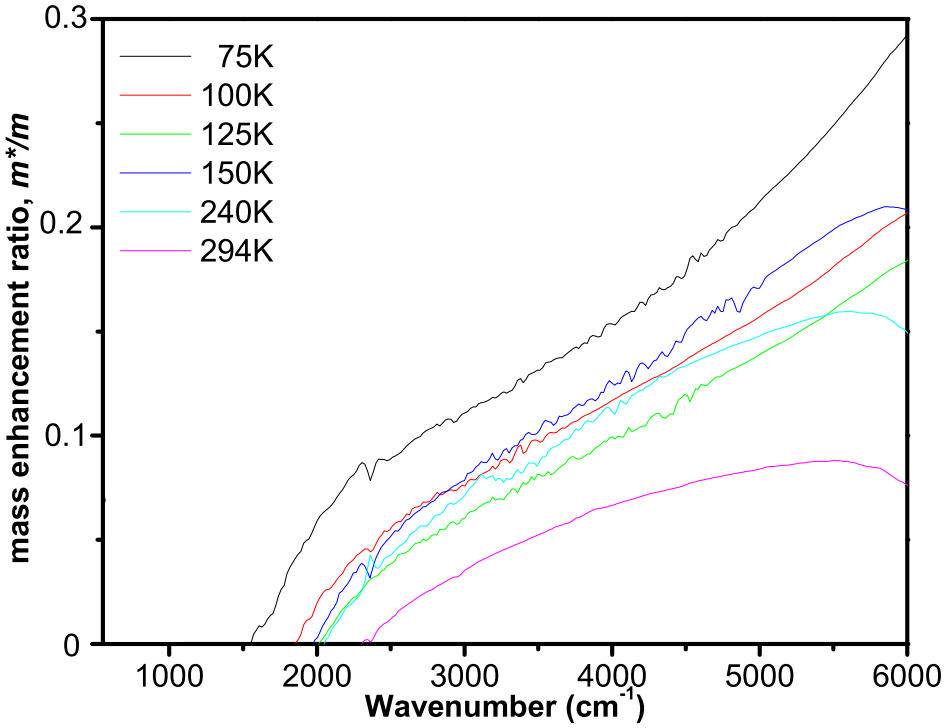

Figure A.6: Mass enhancement ratio for the a-axis of $TMTSF_2PF_6$ at ambient pressure

From here, the Extended Drude model was used to extract the frequency dependent mass enhancement ratio (Figure A.6) and scattering rate (Figure A.8).

m^*/m increases across the whole range but by the largest amount at high wavenumber as the temperature decreases. There is very little change in scattering rate.

A.4 Conclusion

The large number of accessible states make $TMTSF_2PF_6$ worth studying with this pressure cell technique, if the problems in getting good contact with the diamond

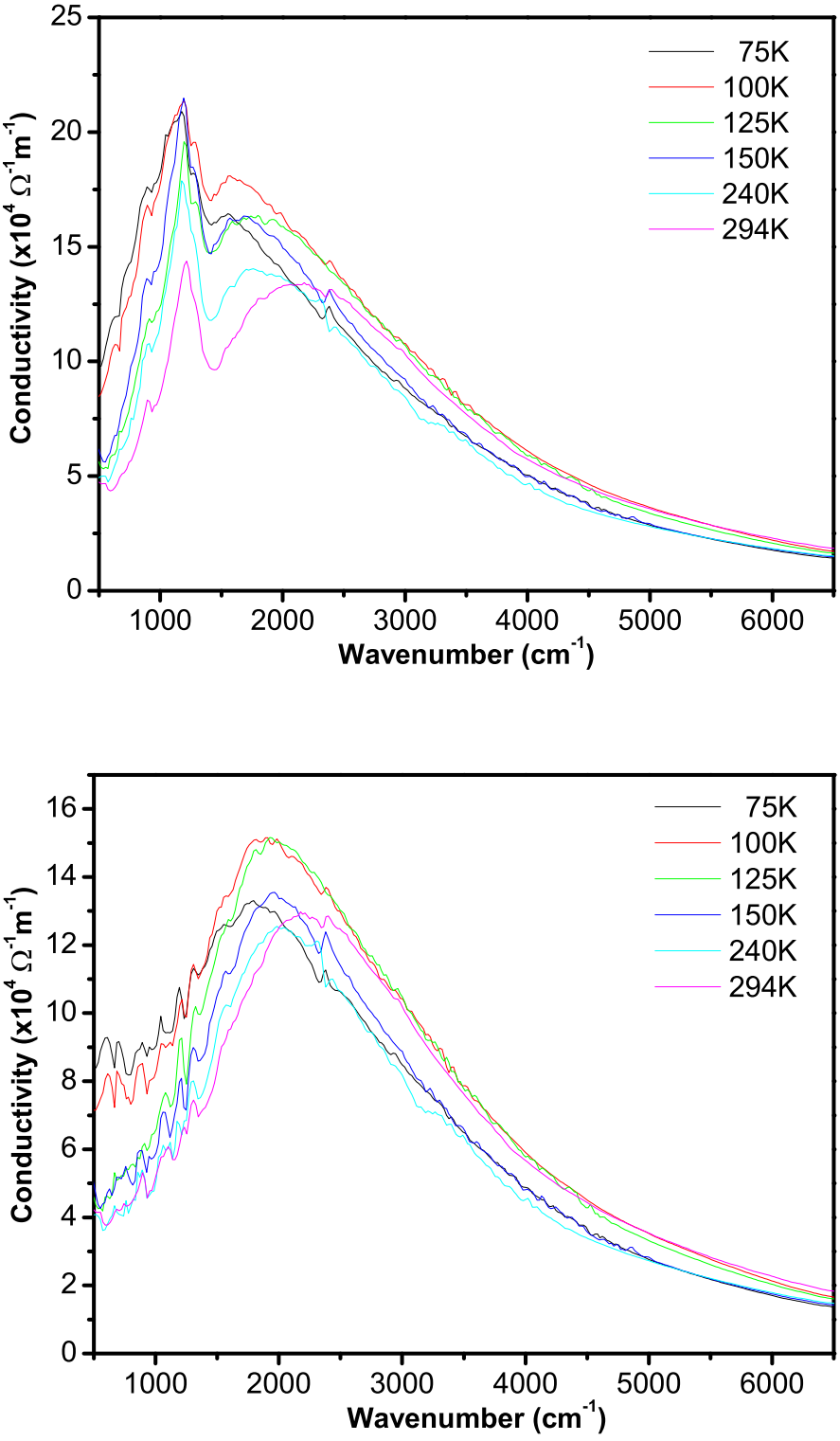

Figure A.7: Optical conductivity of $TMTSF_2PF_6$ parallel to a-axis extracted from the reflectance data using a Kramers-Kronig transformation. Sample under air before (top) and after (bottom) phonon removal

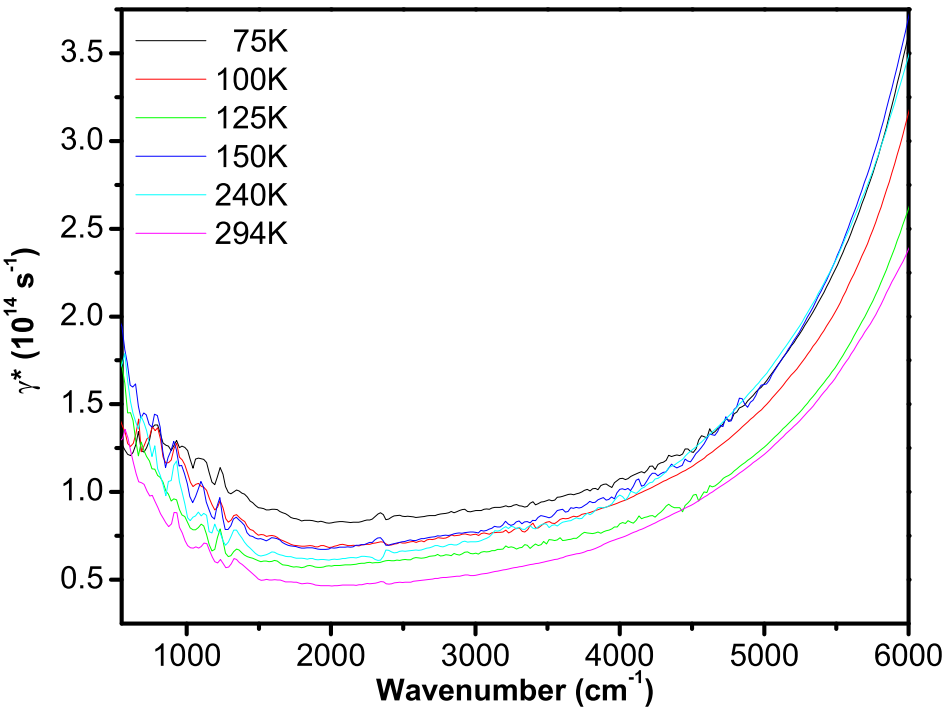

Figure A.8: Renormalised scattering rate for the a-axis of $TMTSF_2PF_6$ at ambient pressure

surface could be overcome. The ease of removing the phonon modes and the relative ease of fitting to the Extended Drude model suggest that this is also a good approach.

Appendix B

Use of the Optical Anvil Pressure Cell

B.1 Overview

In this appendix, I describe the operation of the optical anvil pressure cell. This can serve as an instruction and safety manual for future users. The pressure cell was originally designed to run with two sapphire anvils. This was changed to one sapphire and one diamond to gain increased signal in the IR. A copper gasket separates the anvils and the pressure medium is argon gas. The fluorescence line (excited by an argon laser) of small ruby chips in the cell is used to determine the pressure. It is loaded by cooling the cell with liquid nitrogen and then pumping argon through it. Pressure is changed using a press while the cell is at room temperature. The working pressure range is 20 kbar. Users should try to use the cell at pressures lower than this or its working life may be shortened.

B.2 Parts of the Cell

The cell consists of the parts shown in Figure B.1. The top and bottom anvil mounts only fit together one way; make sure the marks are aligned and it should slide together

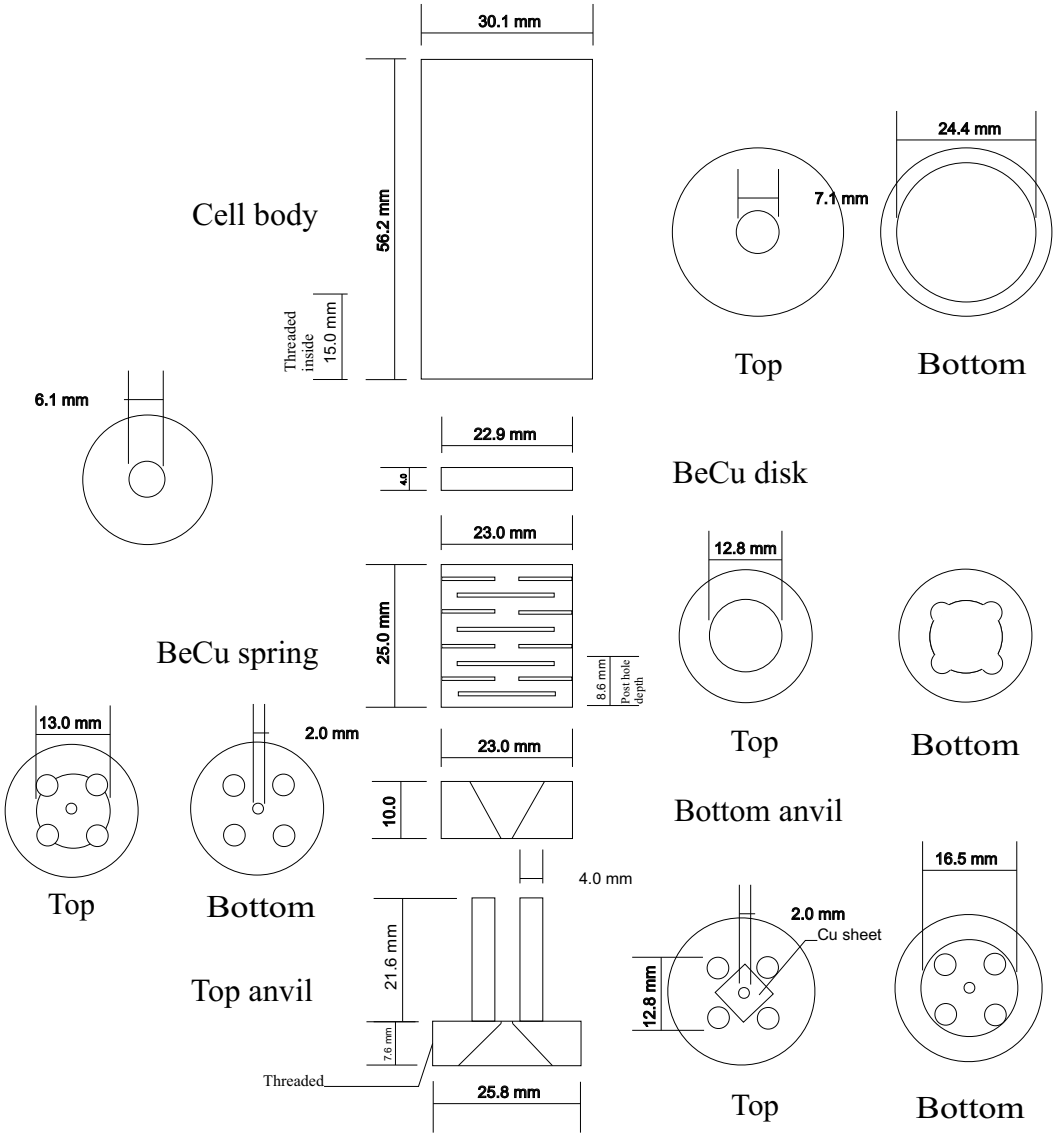

Figure B.1: Exploded diagram of the anvil cell

with slight resistance. Do not push the halves together without a gasket as this can damage the sapphire, or even the diamond.

B.3 Handling the pressure cell

When loaded, the pressure cell is potentially very dangerous. Accidents are rare, but simple precautions can drastically reduce the risk of injury.

1. Do not point the ends of the cell at anyone. This is where failure is most likely to occur.

2. Never look into the top or bottom of a loaded cell. Only use a microscope or large full reflection prism. Do not use a mirror, fragments could bounce off and into the observer.

3. Never shake or knock the cell.

4. Keep the cell shielded whenever possible. The walls of the cryostat or the shields of the press are ideal.

5. When handling an unshielded cell, wear safety spectacles. Keep handling time to a minimum.

6. Put a note to alert others to a loaded, shielded pressure cell if you have to leave it unattended.

B.4 Use of the press

Warning: This is an hydraulic press capable of delivering more that enough pressure to destroy the cell, sending sharp parts flying. Even with careful operation, failure of the anvils can occur. The shields on the press must be closed at all times when the press is in use. Listen for strange noises during use, this may indicate problems with the cell.

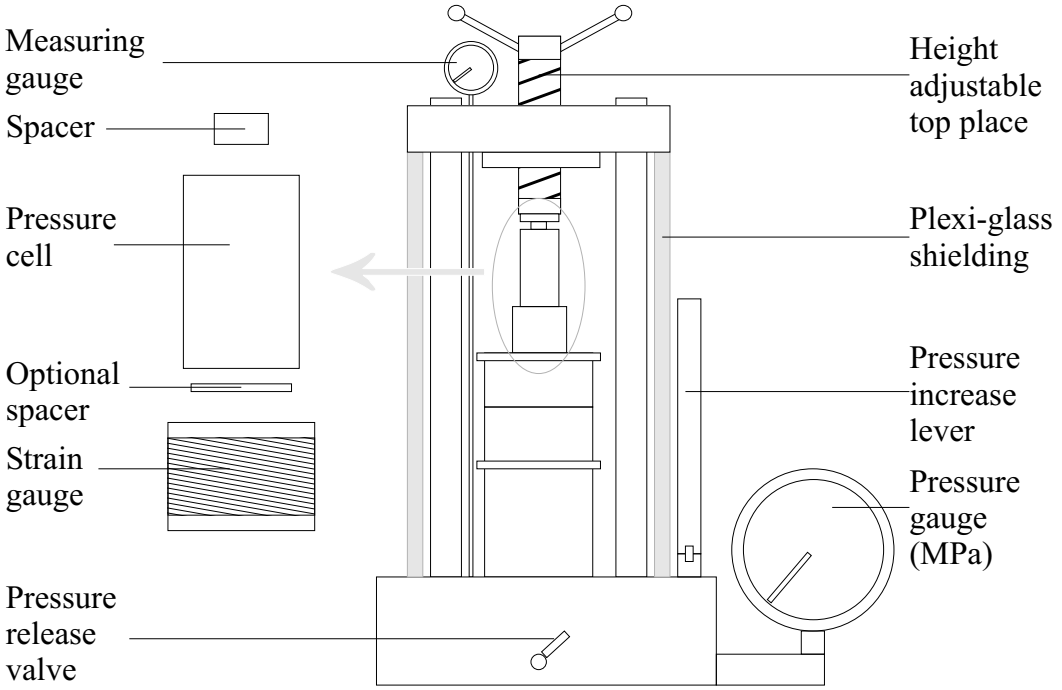

Figure B.2: Schematic of hydraulic press. The press is triangular from the top

1. Slide open the shields and put the cell in the press. Put the strain gauge under the cell and the small spacer that fills the hollow in the cell on top. At higher pressures, an extra, thin circular spacer may be needed to prevent the body touching the press plates. **It is critical that these are placed centrally in the press. Otherwise cell failure may occur.** Close the shields.

2. There is a small tap under the cell lever. This is used for allowing the oil in the press back into the reservoir. Close this now.

3. Screw down the top plate in the press until it is close to, *but not touching* the top of the cell.

4. Insert the measuring gauge and set it close to zero.

5. The strain gauge needs 6 V through it to work. It is a good idea to allow it to run for a while before use as it works by measuring a change in voltage across it and the current causes slight warming. Connect a nanovoltmeter to the gauge. It should read $\sim$13.6 mV. Take 15 samples and average the result, as the reading

fluctuates a great deal. This can be done automatically using the meter.

6. Record the measuring gauge, the strain gauge and the hydraulic pressure gauge as the pressure is increased.

7. Pump the lever until the top plate just touches the cell. You can tell this has happened when the strain gauge voltage just starts to change. This is your starting point.

8. **Slowly** increase the pressure. Stop and take readings at intervals. The intervals depend on whether you are indenting the gasket, increasing the pressure, decreasing the pressure etc. See the individual sections of these instructions.

9. When you have reached your final pressure, wait for a few minutes to allow the gasket to flow.

10. **Wear safety glasses for this step.** Do not do this step if you are only pre-indenting the gasket. Open one of the shields and carefully tighten the cell by rotating the outer body by hand. Do not over tighten; only rotate the body until it does not easily move any further.

11. **Very slowly** release the pressure by opening the tap.

12. Open the shields and remove the cell.

B.5 Strain gauge

This gauge is an elastic cylinder of Ti-alloy with 4 manganin strain gauges attached to its surface to measure deformation. The gauges are connected in a 4 arm bridge arrangement (Figure B.3) to eliminate temperature dependent errors. Two wires are for biasing the bridge with 6 V and the other two are for measuring the voltage. The force applied is governed by the equation:

$$F = -0.48(V - V_0)\mathbf{tonne/mV} \tag{B.1}$$

Here V_0 is the output of the bridge at zero applied force and V is the voltage measured under pressure. V_0 should be measured every time the gauge is used. In addition, the coefficient may change with time and so the gauge should be calibrated with respect to a primary force gauge every year.

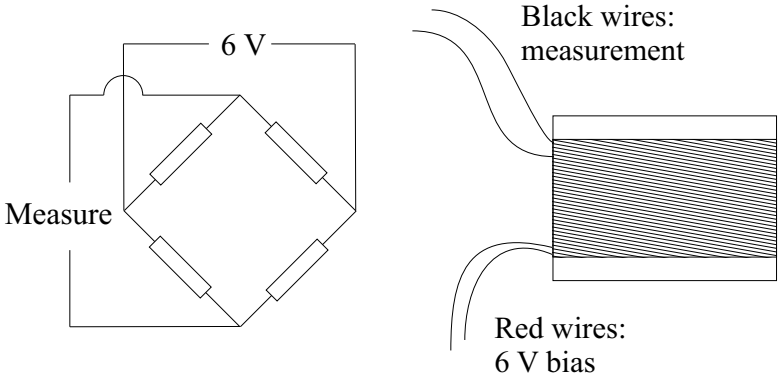

Figure B.3: Strain gauge

B.6 Gasket fabrication

Tip: Making these is quite fiddly and time consuming and you *will* use more than one, so make a batch. I usually make five at a time.

1. Use copper sheet 0.4 mm thick (exact thickness is not critical). Magnet baffle works well.

2. Scribe the outline and then cut out blanks using metal snips (or scissors that you don't mind blunting). Size: 7 mm x 21 mm.

3. Roll flat.

4. Clamp to steel post hole template using tool-maker's clamp. It has holes of 3 mm diameter with centres 12.5 mm apart.

5. Centre punch holes. Do this on a hard surface to minimise distortion of the gasket.

6. Make post holes. They need to be 4 mm diameter. Either drill or punch with a lever punch (better). When punching put the aluminium triangular shield (This is just a 2 mm thick piece of aluminium, about 5 cm on the two short sides, with a hole fractionally larger than 4 mm near one corner) onto the punch first, or it is very difficult to get the gasket off the punch.

7. Test the fit. Ream or file holes to increase size if it does not fit. It should slide on easily, but not rattle too much.

8. Roll flat again.

9. Scribe edge for alignment with marks on cell body.

10. Pre-indent the gasket. Assemble cell and put in press. Slowly ncrease the pressure by $\sim$0.1 mV in steps of $\sim$0.02 mV. Release the pressure and inspect the gasket. If there is no change, increase by a further $\sim$0.1 mV. Measure the thickness of the gasket when indented. Repeat until the gasket is 0.13 mm thick. Measure this using a mircometer, but be very careful to avoid dimpling the surface the gasket further. The entire increase should not be above $\sim$0.3-0.35 mV. Once a given pressure has been obtained, it can be returned to using larger steps.

11. The next few steps are best done using a binocular microscope.

12. Carefully mark the centre of the depression on the diamond side using a scalpel. It should be deep enough to centre a centre drill bit. The easiest way to do this is to make an initial mark and then slowly rotate the gasket under the scalpel.

13. Use a very small centre drill bit to enlarge the indent so a drill bit will not drift. This can be done by twisting it between the fingers or by holding the drill still and rotating the gasket.

14. Drill a 0.5 mm hole using a small drill press. You can still use a binocular microscope if you can angle the head.

15. Clean both sides of the hole using the scalpel to remove any stray metal.

16. Put in the press again and press to the final depth (not final pressure, as this will now be much lower for a given thickness as material has been removed). If this is not possible, then try a range of pressures until the surface is smooth. This will remove any bumps left by drilling the hole. If scratches are still visible, increase pressure slightly.

17. NB the forces required will vary from gasket to gasket and these should be taken as guides.

18. Plate the diamond side of the gasket with gold so it will act as a mirror.

B.7 Assembly of the Cell

Inspect all parts for cracks, strange discolourations, chips or scratches on the diamond or sapphire and wear on threads. If any are found, do not use the cell without further consultation. If the cell already has the sapphire and diamond mounted and properly aligned, you can ignore the rest of this section.

1. Fully disassemble and clean the cell. Acetone is ideal for this and will dissolve the glue. Clean the top and bottom anvil, sapphire, diamond and copper diamond base plate (if missing/broken, making this will be covered in point 3 of this section).

2. Centre the sapphire. Use the top and bottom anvils and the sapphire.

    - Align scratches on cell top and bottom. It should only fit together this way.
    - Gently slide the halves together with the sapphire in between. Centre the sapphire to the hole in the top using a wooden stick (Figure B.4).

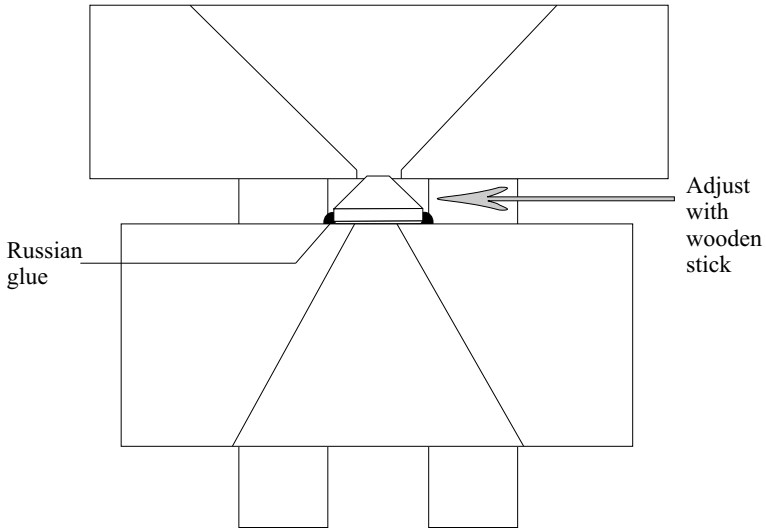

Figure B.4: Gluing and positioning sapphire

- Glue in place with Russian glue. This is better at thermal cycling that GE varnish. Dilute the glue in a watch glass with ethanol to make it flow well and apply with a sharpened wooden stick. Cover as much of the edge as possible then allow to dry. This can take several hours.
- Slide top and bottom apart. Apply glue round the base to fill any gaps.
- NB Care must now be taken cleaning the sapphire as solvents will soften the glue and allow it to shift.

3. Copper diamond base plate.

   - 0.1 mm copper sheet. Cut out and flatten an 8 mm x 8 mm square (slightly thicker will work as well).
   - Drill 2 mm diameter hole in middle and roll flat.
   - Centre the copper visually on the hole in the top anvil and glue with Russian glue at the 4 corners. Adjust copper with wooden stick (NOT metal). There must be no glue anywhere apart from the edges. Allow to dry.

4. Mount diamond.

- Place the diamond on the top anvil, on top of the copper sheet
- Slowly slide the two anvils together until the diamond and sapphire are just touching
- Centre by looking through the sapphire using a wooden stick. Make sure each part of the vertices visible between the edges of the tops of the diamond and sapphire are the same length (Figure B.5). Use a binocular microscope with a scale to measure them.

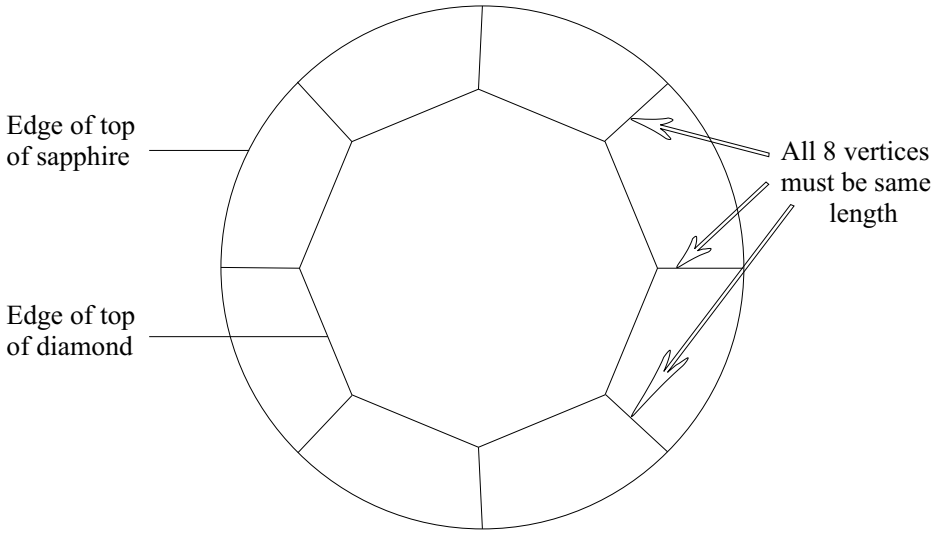

Figure B.5: Aligning the diamond. Viewed down through the sapphire

- Check that the interference fringes are circular (best, but not always possible) or that there is only 1 fringe across the top surface. If there are many fringes, try rotating the diamond and check the surface beneath it. If still no success, the copper sheet and/or the sapphire may need re-mounting.
- Glue round the edge with Russian glue (or other low temperature glue). GE varnish is not suitable as it is too brittle at low temperature for the stresses experienced. Epoxy resin is suitable, however great care should be taken as this is extremely hard to remove (for readjustment etc) once dried.
- Re-check the fringes.
- Allow the glue to dry.

B.8 Mounting the sample

1. Clean the diamond, sapphire and gasket. Ethanol or methanol seem to work best. This is critical and could take over 1 hour to do well.

2. Take the top anvil and place the gasket over the diamond.

3. Place the sample in the middle of the hole in the gasket. It is very important that it is central to the hole, or the gasket may touch it as pressure is applied, and that there is good contact between it and the diamond surface or there will be interference in the spectra.

4. Slide the bottom anvil carefully onto the top until the sapphire touches the gasket. Care must be taken not to move the gasket or the sample may be dislodged.

5. Carefully invert the anvils and look through the diamond at the sample and check for fringes. Ideally there should be none, but one may be permissible. If you have none, make sure that it is not that the sample has fallen off the diamond.

6. Introduce a ruby chip into the hole in the gasket using a needle.

7. Reassemble the cell but do not tighten.

B.9 Loading the cell with pressure medium

This is potentially dangerous as it involves the use of cryogenic liquids (liquid nitrogen) which can cause severe burns, gases at high pressure and a risk of sudden explosion of the cell, ejecting high velocity parts out of the top and bottom. Safety glasses must be worn and it must not be done in an enclosed space.

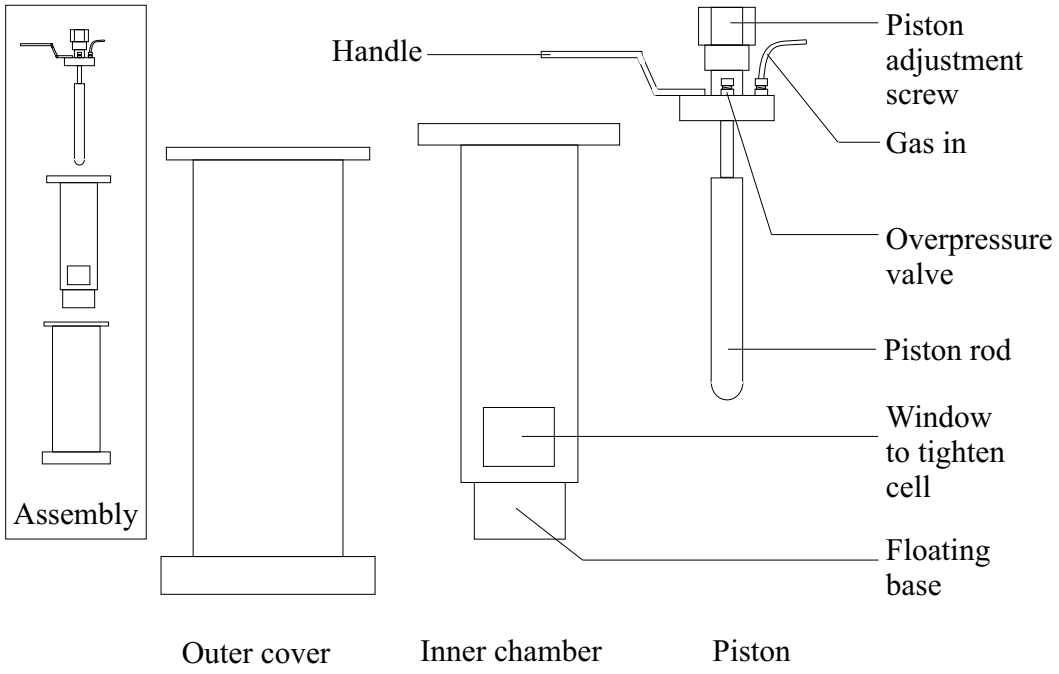

Figure B.6: Schematic of pressure loading vessel

1. Disassemble the pressure loading vessel by removing the two circles of bolts in the top. This allows the outer cover and inner piston to be removed (Figure B.6).

2. Check for and remove any stray dirt.

3. Gently slide the cell into the inner chamber with the spring at the top.

4. Replace the piston but do not put the bolts back. Adjust the length of the piston so that it just touches the BeCu disk over the spring when its top is flush with top of the inner chamber. Wind it up a further half turn. Make a note of exactly how far it has been turned as this is important.

5. Check that the cell is not tightened and that the outer is free to move and then replace the bolts in the top of the piston.

6. Replace and rebolt the outer cover.

7. Connect the vessel, pump and Argon gas cylinder to the valve board, see Figure B.7. All valves should be shut at this point. The gas cylinder should only be open a small amount.

8. Open the valves so that gas flows into the vessel. The flow rate should be somewhere in the middle of the gauge. The vessel has under- and over-pressure valves. Allow the gas to flow for about 1 minute, then pump it out. Carefully cover the under pressure valve and only pump briefly. Repeat several times. The aim is to flush out all gases apart from argon.

9. Keep gas flowing into the vessel and slowly lower it into a bucket of liquid nitrogen. When the boil off slows, top the bucket up again.

10. Throughout the cooling process, make sure that a small amount of gas flows out of the over-pressure valve. If it slows, increase the flow rate.

11. Keep topping up the liquid nitrogen.

12. It may take a couple of hours for the vessel to fill with liquid argon. When this happens, there will be an increase in gas flow through the over-pressure valve.

13. Lower the piston by 1 turn (i.e. half a turn more that just closed).

14. Shut off the gas flow, remove from the liquid nitrogen, open the external vent and allow the system to warm up. This will take several hours.

15. When warm, remove ONLY the outer jacket.

16. Tighten the cell by hand through the window in the bottom of the inner vessel.

17. Wear safety glasses. Remove the top piston and take the cell out. Examine under a binocular microscope to check sample position.

18. Measure pressure to check gas is trapped.

B.10 Loading the cryostat

NB Care must be taken as this procedure involves placing the loaded cell horizontally at chest height. Safety glasses MUST be worn

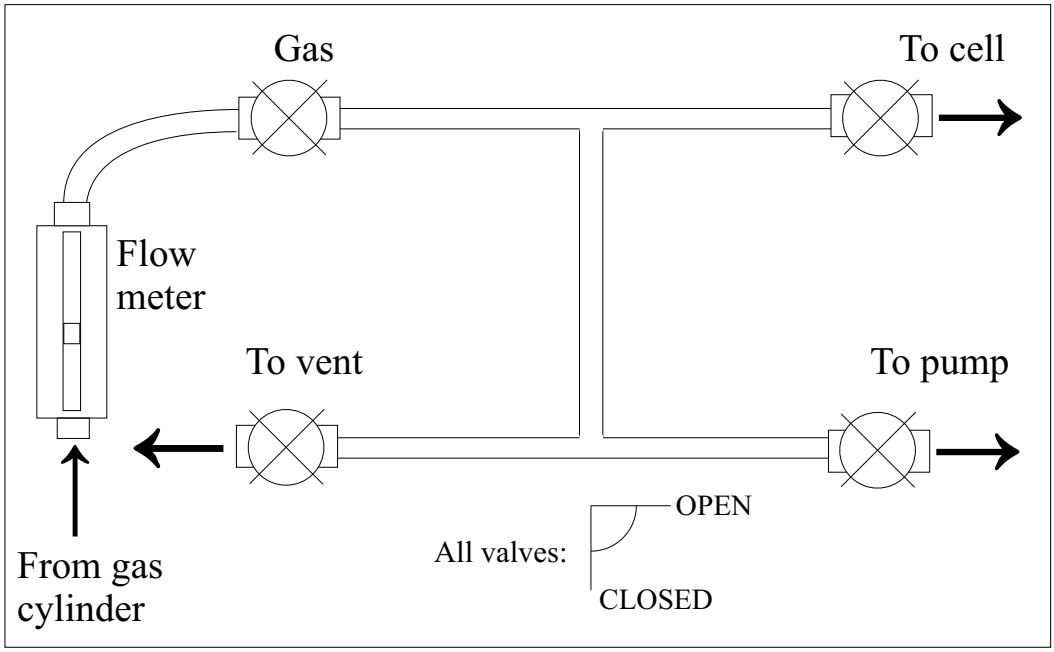

Figure B.7: Argon gas flow control board

1. Remove outer cover and inner baffle of the cryostat.
2. Loosen the top retaining ring. Loosening one of the three screws is enough.
3. Slide the cell into the cryostat and align the mark on the front face of the top anvil with the gap in the top retaining ring.
4. Tighten the top retaining ring, replace the inner baffle and outer cover.
5. Turn the cryostat so that its window faces the microscope so that any explosion would not fire shrapnel at people.

NB if there are problems measuring the pressure, it may be necessary to rotate the cell slightly and make an additional mark on the top retaining ring using a marker. The alignment must stay constant throughout any experimental run.

B.11 Safe use of the optical fibres

The fibres carry potentially dangerous levels of laser light. Treat the fibres with the same respect you would the laser.

1. Fibres may only be connected or disconnected when the laser is off.

2. All fibres must be either connected to ports or have caps on their ends before the laser is turned on.

3. If it is necessary to disconnect a fibre while the laser is on (for alignment purposes), laser safety goggles must be worn.

B.12 Measurement of Pressure

NB Pressure measurement requires the use of an argon ion laser (or equivalent laser of the same wavelength, 532 nm). Laser safety goggles MUST be worn. Direct or reflected light from a laser will cause severe eye damage.

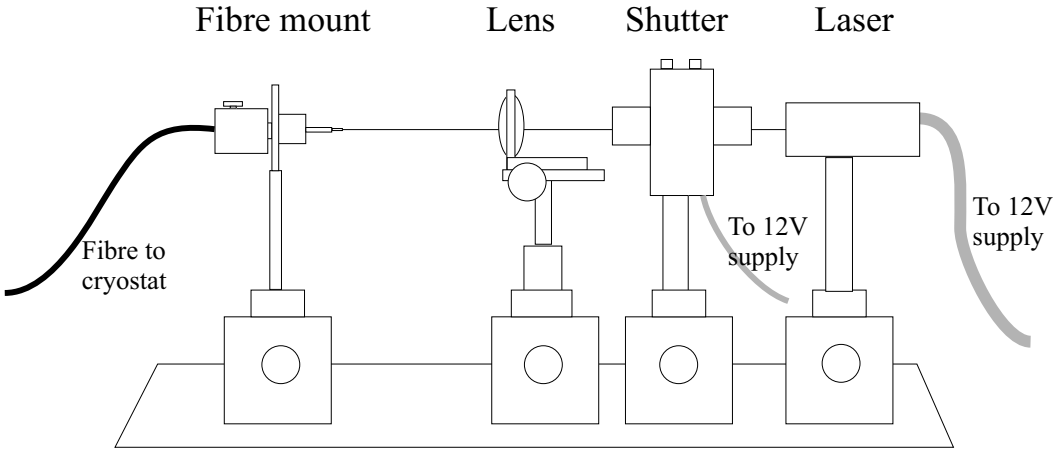

Figure B.8: Schematic of laser bench

1. Connect the fibres to the cryostat. The fibre port 5 on the cryostat is the central fibre and the fibre from the laser should be connected to this.

2. The fibres entering the Raman spectrometer should be just through the aperture, so no radiation escapes.

3. Turn on the spectrometer, control box and its computer. Type "mogina" at the prompt. Go to system→ monos→ spectrograph (or filter). Set 'dial current'

to 1045 and grating to 1800. Set filter→ dial current to 335. Make sure the grating and the two dials on the spectrometer agree with these numbers.

4. Turn on the CCD, its power supply and its computer. Type "ccd" at the prompt. Set the CCD temperature to $5\,^{\circ}\mathrm{C}$ and allow to stabilise. Load a file (eg the "leaves.st6" file. You will see this is the outline off some trees taken using the CCD as a pinhole camera) and then go to "spectrometer". Place a 4 pixel wide zone in the middle of the display.

5. To take a neon calibration spectra, place the neon lamp just in front of the laser fibre. Alignment is important, it may be neccessary to adjust the lamp position to get a good signal.

6. To use the laser:

   - Use the laser sign on the laser room.
   - Wear laser googles.
   - Connect the solid state laser and shutter to a 12 V power supply.
   - Slide the Microscope to "IR" (the shutter safety switch on the microscope will not allow it to open on "view").
   - Close the flaps in the Bruker (prevents possible detector damage).
   - Open the laser shutter (press red button).

7. Use CCD program to take spectra. Time required will vary but typical times are 10-20 seconds for neon and 30-180 seconds for the ruby fluorescence line. Alignment is very critcal. Data can only be removed from this PC using a floppy disk.

Take neon spectra before and after ruby spectra, to check for drift.

B.13 Fitting the Ruby Lines

NB: Most of the following operations can be performed by my matlab program *ruby2.m*.

The output of the CCD is a plot of number of counts against pixel bin. Due to the length of exposure time, the CCD picks up dark noise and these bad pixels need removing by hand. It will be very obvious which and the noisy pixels. There are 375 pixels across the detector and this pixel position needs translating into a wavelength. The detector has a spectral spread of 8 nm, giving $8/375 = 0.0213$ nm/pixel.

1. Fit the before and after neon lines using a Gaussian fit. Average the result.
2. Use a 2 peak Gaussian fit on the ruby data. The bigger peak is the important one.
3. The wavelength of the neon line should be $\lambda_n = 692.94673$ nm
4. Use equation B.2 to obtain the ruby wavelength.

$$\lambda_r = \lambda_n + 0.0213(p_r - p_n) \tag{B.2}$$

Where λ_r is the ruby wavelength and p_r and p_n are the pixel bin numbers of the ruby and neon lines respectively.

Now the wavelengths need converting into pressure. NB the ruby lines shift with both temperature and pressure and this is particularly important above 100 K, where a 6 K change has the same effect as 1 kbar. There are two ways to allow for this:

1. Use an equation to fit this (most are only well tested for above 150 K)
2. Obtain a calibration curve by running the system at a range of temperatures at zero pressure (better but time consuming to set up initially)

We will use the second method as it is more accurate at our temperature and pressure range. The values for $\lambda_{r_0,P=0,T=x}$, the ambient pressure wavelength at $T = x$ K, are

used in place of λ_{r_0} in equation B.3.

$$P = \frac{A}{B}\left(\left(1 + \frac{\lambda_r - \lambda_{r_0}}{\lambda_{r_0}}\right)^B - 1\right) \tag{B.3}$$

Where $A = 19040$ kbar and $B = 7.665$. This give a P in kbar.

B.14 Cooling the Cell

The combined cell and cryostat respond to temperature changes very slowly. In any case, a slow cooling rate of not greater than 1 K min^{-1} should be used to reduce the chance of introducing shear forces on the sample. It is important that the cell should be observed through the microscope frequently to check that the gasket has not collapsed on cooling or that the sample has lifted off the diamond surface. If this occurs, coloured fringes will be seen. If this happens, warm the cryostat up to the last temperature where no fringes were present and wait for 20 minutes, as the sample will often reattach to the surface. If this does not happen, then the cell will need to be reloaded. If the gasket starts to collapse, warm the cell back up to room temperature and disassemble as soon as possible.

The temperature in the cell may lag behind that measured by the temperature controller. This is because it is not possible to mount the thermometer next to the sample– the closest it can be is on the outside of the cell. It is possible to determine when steady state has been reached by measuring the ruby line, as this changes with temperature. Experiment has shown that a period of 30 minutes is sufficient for the system to stabilize.

Appendix C

List of Publications

1. *New superconducting charge-transfer salts (BEDT-TTF)$_4$[A·M(C$_2$O$_4$)$_3$]·C$_6$H$_5$NO$_2$ (A = H$_3$O or NH$_4$, M = Cr or Fe, BEDT-TTF = bis(ethylenedithio)tetrathiafulvalene);*

   S Rashid, S S Turner, P Day, J A K Howard, P Guionneau, E J L McInnes, F E Mabbs, R J H Clark, S Firth, T Biggs, *Journal of Materials Chemistry 11*, **9**, 2095 (2001)

2. *Comparison of the normal-state properties of κ-(BEDT-TTF)$_2$Cu(SCN)$_2$ and its deuterated analogue in high magnetic fields and under high hydrostatic pressures;*

   T Biggs, A-K Klehe, J Singleton, D Bakker, J Symington, P Goddard, A Ardavan, W Hayes, J A Schlueter, T Sasaki, M Kurmoo, *Journal of Physics: Condensed Matter*, **14**, L495 (2002)

3. *Study of magnetoresistance under hydrostatic pressure in the deuterated organic superconductor d$_8$-κ-(BEDT-TTF)$_2$Cu(SCN)$_2$;*

   T Biggs, D Bakker, A-K Klehe, J Symington, J Singleton, T Sasaki, M Kurmoo, *Synthetic Metals*, **133**, 239 (MAR 13 2003)

4. *Comparative magnetotransport and T_c measurements on κ-(BEDT-TTF)$_2$Cu(SCN)$_2$ under pressure;*

   A-K Klehe, T Biggs, C A Kuntscher, A M Kini, J A Schlueter, *Journal of Physics: Condensed Matter*, **16**, 6109 (2004)

5. *Comparative magnetotransport and T_c measurements under pressure on κ-(BEDT-TTF)$_2$Cu(SCN)$_2$;*

   A-K Klehe, T Biggs, T Tomita , J S Schilling, A M Kini, J A Schlueter, *Journal de Physique IV*, **114**, 217 (APR 2004)

Bibliography

[1] J Singleton, *Rep. Prog. Phys.* **63**, 1111-1207 (2000)

[2] J Wosnitza, Fermi Surfaces of Low-Dimensional Organic Metals and Superconductors, Berlin: Springer, (1996)

[3] T Ishiguro and K Yamaji, Organic Superconductors 2^{nd} ed., Springer-Verlag (1998).

[4] W Little, *Phys. Rev.* **134**, 1416, (1964)

[5] J Singleton, Band Theory and Electronic Properties of Materials, Oxford: Oxford University Press, (2000)

[6] J Caulfield, W Lubcynski, F Pratt, J Singleton, D Ko, W Hayes, M Kurmoo and P Day, *J. Phys.:Condens. Matter*, **6**, 2911 (1994)

[7] R Mckenzie, *Comments Cond. Matt. Phys.* **18**, 309 (1998)

[8] J Schmalian, *Phys. Rev. Lett.* **81**, 4232, (1998)

[9] B Bleaney & B I Bleaney, Electricity & Magnetism: volume I (1993)

[10] M Dressel and G Gruner, Electrodynamics of Solids, Cambridge University Press (2002)

[11] L D Landau & E M Lifshitz, Statistical Physics Pergamon Press (1958)

[12] J R Hook & H E Hall, Solid State Physics, Wiley, (1991) chapter 13

[13] A S Barker $Phys.\ Rev.\ B$,**vol 12**, No 10, 4071 (1975)

[14] C Kittel, Introduction to Solid State Physics, Wiley, (1996)

[15] R F Wallis & M Balkanski, Many-body Aspects of Solid State Spectroscopy, NHPC (1986)

[16] J Reitz, F Milford, and R Christy, Foundations of Electromagnetic theory, 4^{th} edition, Addison Wesley (1993)

[17] T Timusk and D Tanner, Physical properties of high temperature superconductors, World Scientific Vol.1 (1989)

[18] D A Crandles, T Timusk, J D Garrett, J E Greedan *Phys. Rev. B*, **49**, 16207 (1994)

[19] N W Ashcroft, N D Mermin, Solid State Physics, New York: Holt, Rinehart and Winston (1976)

[20] D Shoenberg, Magnetic Oscillations in Metals, Cambridge: Cambridge University Press, (1984)

[21] N Harrison, A House, I Deckers, J Caulfield, J Singleton, F Herlach, W Hayes, M Kurmoo and P Day, *Phys. Rev. B* **52**, 5584 (1995)

[22] N Harrison, R Bogaerts, P Reinders, J Singleton, S J Blundell and F Herlach, *Phys. Rev. B* **54**, 9977, (1996)

[23] K Takenaka, R Shiozaki and S Sugai, *Phys. Rev. B*, **65**, 184436, (2002)

[24] J Singleton, F L Pratt, M Doporto, W Hayes, T J B M Janssen, J A A J Perenboom, M Kurmoo and P Day, *Phys. Rev. Lett.*, **68**, 2500 (1992)

[25] R J Bell, An Introduction to Fourier Transform Spectroscopy, Academic Press (1972)

[26] M L Boas, Mathematical Methods in the Physical Sciences, Wiley (1961)

[27] E Hecht, Optics 3rd Edition, Addison Wesley Longman (1998)

[28] M Eremets, High Pressure Experimental Methods, Oxford University Press (1996)

[29] H K Mao, J Xu and P M Bell, *J. Geophys.Res*, **91**, 4673 (1986)

[30] 3M chemical company, *Application Information: Fluorinert Liquids For Electronic Reliability Testing* (2003)

[31] J E Schirber, *Cryogenics* **10**, 418 (1970)

[32] J Wilks and E. Wilks, Properties and Applications of Diamond, Butterworth-Heinemann Ltd., Oxford, (1991)

[33] A-K Klehe, Dissertation for PhD, Washington University, Missouri (1995)

[34] I L Spain and S Segall, *Cryogenics*, **11**, 26 (1971)

[35] S Lefebvre, P Wzietek, D Jerome, C Meziere, M Fourmigue and P Batail, *Phys. Rev. Lett.*, **85**, 5420 (2000)

[36] M R Presland, J L Tallon, R G Buckley, R S Liu and N D Flower, *Physica C*, **176**, 95 (1991)

[37] R McKenzie, *Science* **278**, 820 (1997)

[38] D Pedron, G Visentini, R Bozio, J M Willians and J A Schlueter *Physica C* **276**, 1 (1997)

[39] J Singleton, P A Goddard, A Ardavan, N Harrison, S J Blundell, J A Schlueter and A M Kini *Phys. Rev. Lett.*, **88**, 037001 (2002)

[40] A M Kini, K D Carlson, H H Wang, J A Schlueter, J D Dudek, S A Sirchio, U Geiser, K R Lykke and J M Williams *Physica C* **264**, 81 (1996)

[41] J A Schlueter, A M Kini, B H Ward, U Geiser, H H Wang, J Montasham, R W Winter and G L Gard *Physica C* **351**, 261 (2001)

[42] T Biggs, A-K Klehe, J Singleton, D Bakker, J Symington, P Goddard, A Ardavan, W Hayes, J A Schlueter, T Sasaki, M Kurmoo *J. Phys.: Condens. Matter* **14**, L495 (2002)

[43] A-K Klehe, T Tomita, J S Schilling, A M Kini and J A Schlueter, *Physica C*, **402**, 17 (2004)

[44] T Sasaki, H Sato, N Toyota, *Physica C* **185-189**, 2687 (1991); *Solid State Commun.* **76**, 507 (1990)

[45] J M Caulfield, DPhil. Thesis, Oxford University (1994)

[46] N Harrison, J Caulfield, J Singleton, P H P Reinders, F Herlach, W Hayes, M Kurmoo, P Day *J. Phys. Condens. Matter* **8**, 5415 (1996)

[47] C Martin, C C Agosta, S W Tozer, H A Radovan, T Kinoshota and M Tokumoto, *Journal of low temperature physics*, **138**, 1025 (2005)

[48] M Rahal, D Chasseau, J Gaultier, L Ducasse, M Kurmoo and P Day, *Acta Crystallogr.*, **B53**, 159 (1997)

[49] J Muller et al, *Phys. Rev. B*, **61**, 11739 (2000)

[50] K Takemura, *Phys. Rev. B*, **60**, 6171 (1999)

[51] M Maesato, Y Shimizu, T Ishikawa and G Saito, *Synth. Metals*, **137**, 1243 (2003)

[52] T Ishikawa, M Maesato, G Saito,*Synth. Metals*, **133**, 227 (2003)

[53] H Weiss, M V Kartsovnik, W Biberacher, E Steep, A G M Janson and N D Kushch, *JETP Lett.*, **66**, 202 (1997); H Weiss, M V Kartsovnik, W Biberacher, E Steep, E Balthes, A G M Janson , K Andres and N D Kushch, *Phys. Rev. B*, **59**, 12370 (1999)

[54] W-M Lee, *Solid State Commun.*, **106**, 601 (1998)

[55] V A Sidorov and R A Sadykov, *J. Phys.: Condens. Matter*, **17**, S3005 (2005)

[56] A-K Klehe, T Biggs, C A Kuntscher, A M Kini, J A Schlueter, *J. Phys.: Condens. Matter*, **16**, 6109 (2004)

[57] J J Neumeier, H A Zimmermann, *Phys. Rev. B*, **47**, 8385 (1993)

[58] P Goddard, DPhil thesis, Oxford University (2003)

[59] R Louati, S Charfi-Kaddour, A Ben Ali, R Bennaceur and M Heritier, *Phys. Rev. B*, **62**, 5957 (1999)

[60] R D McDonald, DPhil Thesis, Oxford University (2001)

[61] J E Eldridge, Y Xie, H H Wang, J M Williams, A M Kini and J A schlueter, *Spectrochim. Acta A* **52**, 45 (1996)

[62] N B Colthup, L H Daly, S E Wiberley, Introduction to Infrared and Raman Spectroscopy 3^{rd} Edition, Academic Press (1990)

[63] T Sugano, M K H Hayashi and K Nishikida, *Phys. Rev. B* **39**, 11387 (1989)

[64] J E Eldridge, C C Homes, J M Williams, A M Kini and H H Wang, *Spectrochim. Acta.*, **51A**, 947 (1995)

[65] A-K Klehe, R D McDonald, A Goncharov, V Struzhkin, H Mao, R Hemley, T Sasaki, W Hayes and J Singleton, *J. Phys.: Condens. Matter*, **12**, L247 (2000)

[66] A-K Klehe, R D McDonald, J Singleton, A Kleppe, H Olijnyk, A P Jephcoat, A F Goncharov, V V Struzhkin, H Mao, R J Hemley, T Sasaki, *Synth. Met.*, **120**, 857 (2001)

[67] T Sasaki, I Ito, N Yoneyama, N Kobayashi *Phys. Rev. B* **69**, 064508 (2004)

[68] K Kornelsen et. al., *Phys. Rev. B* **44**, 5235 (1991)

[69] N L Wang, B P Clayman, H Mori, S Tanaka, *Physica B* **284-288**, 513 (2000)

[70] E Griesshaber, M Schiller, D Schweitzer, I Heinen, W Strunz *Physica C* **317-318**, 421 (1999)

[71] J E Eldridge, K Kornelsen, *Solid State Comm.*, **79**, 583 (1991)

[72] D B Tanner and T Timusk, in Physical Properties of High Temperature Superconductors III, edited by D M Ginsberg, World Scientific, p363 (1992)

[73] K Takenaka, R Shiozaki, S Okuyama, J Nohara, A Osuka, Y Takayanagi and S Sugai, *Phys. Rev. B*, **65**, 092405 (2002)

[74] F Kagawa, T Itou, K Miyagawa and K Kanoda, *Phys. Rev. B*, **69**, 064511 (2004)

[75] K Bechgaard, C S Jaconsen, K Mortensen, J H Pederson, N Thorup, *Solid state Commun.*, **33**, 1119 (1980)

[76] M Dressel, *Nature*, **90**, 337 (2003)